Global and Local Structural Health Monitoring Methods Based on Wireless Telemetry and Boundary-based Thermography

by

Nephi Ross Johnson

A dissertation submitted in partial fulfillment
of the requirements for the degree of
Doctor of Philosophy
(Civil Engineering)
in the University of Michigan
2017

Doctoral Committee:

Professor Jerome P. Lynch, Chair
Associate Professor Matthew D. Collette
Associate Professor Ann E. Jeffers
Assistant Professor Branko Kerkez

Nephi R. Johnson
nephi@umich.edu
ORCID iD: 0000-0002-2100-3767

DEDICATION

To *Meu Amor*, the most loving, supportive, understanding, fun and beautiful woman in the world; and to my children, who have sacrificed more and provided more joy and encouragement than anyone could imagine.

ACKNOWLEDGEMENTS

My utmost appreciation and gratitude go to my wife, Ashley, whose unwavering love, support and confidence in me provided a source of strength and never ending encouragement. She delayed pursuing her own goals and ambitions to make sure our children and I were taken care of and always happy. My children too, offered motivation to me to accomplish my goals and demonstrated understanding beyond their years with respect to sacrifices that were necessary for me to complete my education. Not to mention the joy I had in getting to play with them after studying and research. I can never repay my wife and children for the role they played in my, or more accurately, our accomplishments.

My parents were the best examples of work ethic and taught me the importance of high educational aspirations. I owe a lot to them for the firm foundation they created for me in my life. My father's advice that, "you will never regret taking an opportunity to obtain further education," still motivates me today. My wife's parents have always displayed the highest level of confidence in me and have always been willing to help my family in any way possible at the drop of a hat. Their love and support helped me overcome many of the obstacles associated with pursuing my education.

My lab-mates in the basement deserve a great deal of appreciation. I was able to learn so much studying and working alongside them as well as have fun. Most importantly I was able to build lasting friendships with them that I value greatly.

My advisor and mentor Professor Lynch offered the best guidance I could have expected and enabled me to succeed academically and professionally. His leadership challenged me to grow and develop while providing valuable insight along the way. He continually kept me focused on the end goal of research projects and education while encouraging me to find and pursue my interests. Professor Jeffers provided a great example of research habits and was very welcoming of me as an adopted member of her research group. The advice she provided along the way was always very well thought out and applicable. Professor Kerkez provided constant motivation whether by just seeing him in the halls or when we would have discussions in his office. He was always excited to hear about what was going on and help in any way possible. Professor Collette provided a priceless amount of valuable knowledge in the domain of naval architecture that I never would have been able to grasp without his guidance. I really appreciate how willing he was to meet up with me and discuss our project.

The bridge monitoring portion of this research effort has been supported in part by Union Pacific Railroad; however, all findings and claims are the opinions of the authors and do not represent claims by Union Pacific Railroad. The generous support and assistance of Union Pacific employees during work on the Harahan Bridge is greatly appreciated. This research project was sponsored by US Department of Transportation (USDOT), Office of the Assistant Secretary for Research and Technology (OST-R) – Award # OASRTRS-14-H-MICH. The views, opinions, findings and conclusions reflected in this dissertation are solely those of the authors and do not represent the official policy or position of the USDOT/OST-R, or any State or other entity. USDOT/OST-R does not

endorse any third party products or services that may be included in this dissertation or associated materials.

I would also like to acknowledge the generous support provided by the officers of the United States Coast Guard, most especially the crew of the RB-M vessel tested at Cape Disappointment, WA. This portion of the research was funded by the Naval Engineering Education Consortium (NEEC) headquartered at the University of Michigan.

The development of the wireless impedance analyzer was funded under FAA Cooperative Agreement Number 13-G-017. I would also like to express my appreciation to my collaborators in this project who are led by Dr. Ken Loh formerly at the University of California-Davis and now at the University of California-San Diego.

I would like to gratefully acknowledge the generous support offered by the National Science Foundation through Grant Number 0846256, which funded the heat-transfer damage detection efforts.

Finally, I would like to express my gratitude for the funding that I received through the Rackham Merit Fellowship (RMF) and the Rackham Engineering Award (REA).

TABLE OF CONTENTS

LIST OF FIGURES

LIST OF TABLES

ABSTRACT

Our nation's economy is dependent upon its transportation system for the movement of people, goods and services. Infrastructure plays a vital role in supporting transportation services. Given their importance, structures must be maintained to offer safe and reliable operations over extended life-cycles. Structural health monitoring (SHM) has emerged to offer owners a quantitative approach to monitoring structures, assessing system performance and estimating structural conditions. While SHM systems have been successfully deployed to structures, their full potential has not been reaped due to the gap that exists between SHM data and the decision-making needs of owners. This thesis contributes to the field by bridging this gap through two approaches. First, the thesis explores the advancement of wireless monitoring systems whose instrumentation strategy is defined by the needs of the decision-making process of the owner. This is illustrated in the thesis by exploring wireless monitoring systems and associated data-to-decision (D2D) frameworks in the United States Coast Guard (USCG) high-speed aluminum Response Boat-Medium (RB-M) and in the Harahan Bridge. In the former, the wireless hull monitoring system is tailored to derive RB-M hull response data over a short-period to create relationships between the environmental and operational conditions (EOC) of the vessel and the accumulation of fatigue in a critical hull component. In doing so, the vessel owner can make life-cycle decisions centered on managing fatigue accumulation by considering the future operational profile of the vessel. In the latter application, a wireless monitoring system is installed on the Harahan Bridge (which is a steel truss railroad bridge)

to monitor bridge responses to triggered load events including trains, collisions, and earthquakes. Again, a fatigue critical eyebar element is considered with an alerting framework created to alert the bridge owner of overloading conditions that can accelerate fatigue accumulation. While the two case studies showcase clear benefits to designing wireless monitoring systems around the decision-making of the asset owner, they also highlight the value of local structural measurements for component health assessment. To extend the benefits offered by local sensing further, the thesis explores the creation of a cost-effective approach to damage detection through thermal conduction. Using point heaters and temperature sensors, a thermal-based computed tomography (CT) image reconstruction method is developed for two-dimensional (2D) mapping of structural conditions. This powerful local damage imaging method is implemented using a wireless impedance analyzer developed for use in structural wireless monitoring systems. In summary, a new approach to designing SHM systems is developed that looks first at the desired outcome, or decision that the data should inform. This is showcased in two unique wireless monitoring system and D2D framework studies. Next, a novel thermal imaging technique is proposed and validated. Lastly, a first-of-its-kind multi-functional wireless impedance analyzer is developed that is capable of enabling the wireless and permanent installation of multiple spatial sensing techniques.

CHAPTER 1

INTRODUCTION

A nation's security, economic well-being and citizen's standard of living are heavily reliant on the functionality of its infrastructure. As such, this chapter highlights the importance of maintaining this infrastructure and the role structural health monitoring (SHM) can play in doing so. This chapter begins with a description of the current state of practice in SHM with an illustrative review of pertinent research. While SHM continues to mature, there remains a gap between SHM data acquisitions and direct decision-making by infrastructure owners using data and information derived from an SHM system. A case is specifically made for unifying global and local sensing strategies to inform analytical frameworks that asset managers can use to infer structural performance, assess structural health, and make decisions. The chapter delineates the research objectives of the dissertation followed by a chapter-by-chapter overview of the dissertation.

1.1 Motivation for Structural Health Monitoring

Whether via land, air or sea, the ability to efficiently transport goods, services and people is crucial to a country's economic prosperity. In fact, a key indicator in global competitiveness is infrastructure investment and quality (Schwab 2013). Examples of critical assets that constitute a working infrastructure are bridges, roads, railroads, dams, pipelines, airplanes and ships. There are many stakeholders effected by infrastructure

performance; namely, its users (which include people, government and enterprise) and its owners (both government and private owners). Notwithstanding its prime importance, much of America's and other developed countries' infrastructures require significant investment to maintain its high standards of service (ASCE 2013; CIRC 2016). Thus, substantial investments must be made to expand, replace, maintain and ensure the safety of an aging infrastructure inventory. However, infrastructure renewal is limited by both funds and time.

In an effort to efficiently address infrastructure needs, the use of sensing, damage detection strategies and structural assessment procedures has increased in recent years. Such efforts are widely termed structural health monitoring (SHM). The three key motivators to exploring an SHM strategy for a given infrastructure asset are to:

- increase user safety;
- minimize cost (maintenance, replacement and/or downtime);
- maximize functionality (capacity, speed and service-life)

Clearly, if infrastructure is not properly maintained or vigilantly inspected, structural failures can occur. Select examples of catastrophic failures that could have *potentially* been avoided had SHM techniques been instituted are: the Silver Bridge collapse (Lichtenstein 1993), Aloha Flight 243 inflight fuselage separation (NTSB 1989), Prestige oil tanker sinking (ABS 2003), and the San Bruno pipeline explosion (NTSB 2010). In fact, the Prestige had identical sister vessels that had been taken out of commission based on results obtained from SHM analyses that had been carried out (Lladós and Petit 2013). In design, there is a minimum threshold of safety that must be met and is strictly regulated by codes and standards. However, assurance that a structure meets such standards can be

dramatically improved via SHM techniques. In addition to preventing failure or loss, multi-facet monitoring schemes allow for optimal use of maintenance resources (Ettouney and Alampalli 2016). Furthermore, detailed knowledge of a structure's performance enables potential extensions to its service-life and operational profile; thereby, saving owners the costs associated with replacement. Extending service lives is also sustainable with infrastructure embodied energy and CO_2 emissions amortized over longer periods of time.

1.2 Requirements for an Effective Monitoring System

Detecting damage or areas that pose safety threats at the earliest possible juncture in time dramatically reduces the risk of death, injury and property damage. Likewise, obtaining the most insightful information about a structure and its response leads to the optimum use of maintenance resources allocated to the asset over its service life. Whether the promptness and impact of monitoring is enhanced through higher quantity or quality of observations, the primary factor to consider is cost versus benefit (Aktan et al. 2000). That is, does the improvement in safety, reduction in operating costs, and expansion of functionality/capacity outweigh the investment required to obtain such an upgrade?

In addressing these objectives, an ideal monitoring system is equipped with structural assessment capabilities that analyze the current state of the structure, detect any changes in state, and relate environmental and operating conditions (EOCs) (*e.g.*, temperature, wind, waves) to structural responses (*e.g.*, strain, displacement, acceleration, damage accumulation such as fatigue). Such systems can be implemented with various approaches. The most basic approach is of course visual inspections, but more quantitative

approaches include global sensing and local forms of non-destructive evaluation (NDE) (Farrar and Worden 2007). While visual inspection is a well-established and well proven method for acquiring information on a structure, it is largely a qualitative approach. Local damage, especially when small or hidden from view, can be difficult to identify visually. Hence, sensing technology is favored when quantitative data is sought. An SHM system designed using sensing technology must be capable of acquiring data associated with the structure EOCs. Furthermore, it must also be capable of accurately measuring global and local structural behavior. SHM systems are also intended to process the data collected to extract actionable information (Staszewski et al. 2004). To have beneficial impact, the information extracted from raw measurements must aid decision makers (more specifically, to make better decisions). Hence, SHM data processing may aim to: identify damage or changes in structural conditions, identify changes in structural behavior, and estimate residual structural capacity, among other processing needs. By offering asset managers more actionable information, the SHM system begins to offer benefits that will clearly outweigh (and justify) system costs.

1.3 Current State of Practice in Structural Health Monitoring

1.3.1 Structural Health Monitoring Overview

There are many forms of SHM, each with its own set of advantages (Sohn et al. 2003). Although visual inspections and routine maintenance are very valuable, they also have their shortcomings. For example, they are only performed periodically and include a degree of subjectivity (Moore et al. 2001). Non-destructive evaluation (NDE) techniques provide more detailed information about a structure but similar to visual inspections, are

executed on a periodic (*i.e.*, not continuous) basis and often in a manual manner. For mobile structures (*e.g.*, naval vessels), NDE is only performed when the structure is at rest and not experiencing typical operational loading. For this reason, permanent monitoring systems directly installed on a structure have been developed that provide continuous data on a structure's operational conditions and responses.

Many of the permanent structural monitoring systems consist of a network of distributed single point sensors that assess global structural behavior (such as modal properties derived from accelerometer data) or highly localized behavior (such as strain at a single location). Today, monitoring systems defined by point measuring sensors dominate the market. While valuable data can be acquired from these point sensors, they require sophisticated data processing schemes to identify damage at locations not collocated with a sensor. These damage detection methods are generally based on posing damage detection as an inverse problem; such problems are difficult to solve and can be ill-posed (Friswell 2007).

The need to improve on single point sensor networks using distributed sensing for certain applications has been highlighted by the use of embedded fiber-optic sensors (Murayama et al. 2012) that provide strain readings along the one dimensional length of the fiber, the use of carbon nanotube sensing skins (Loh et al. 2009) for two-dimensional (2D) sensing via electrical impedance tomography (EIT), the use of piezoelectric sensors (Hay et al. 2006) for 2D spatial sensing, and the use of thermal heat sources (typically heat lamps or lasers) and infrared (IR) cameras to reconstruct 2D and three-dimensional (3D) images inferred from structural heat transfer properties to detect damage (Roemer et al. 2013). Figure 1.1 illustrates the ability of various sensor approaches to accurately detect

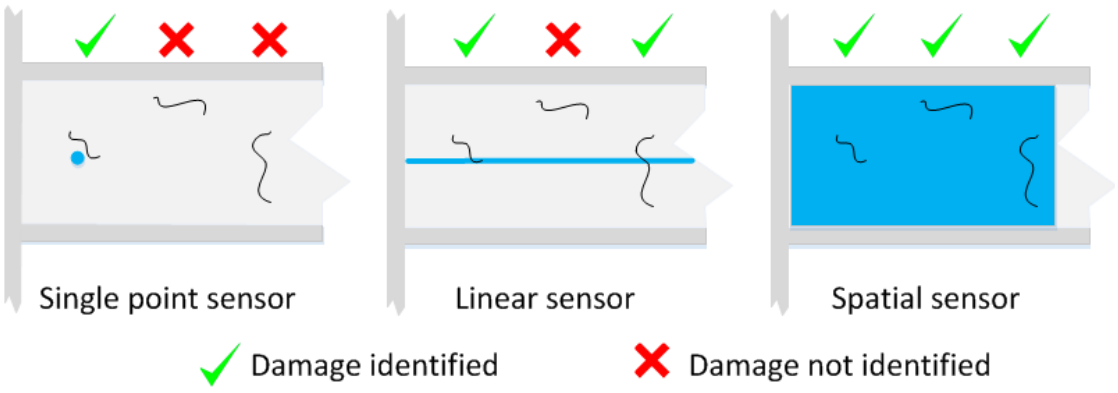

Figure 1.1 Example of different sensor types and each type's ability to detect damage at different locations.

damage. Intuitively, the more area over which the sensor interrogates, the more likely that damage, if present, will be detected.

Another approach to structural assessment is based on life-cycle forecasting. In such methods, one forecasts the EOC a structure might experience and uses models of the structure's response to such EOCs to predict future performance. Such tools have proven valuable in assessing structural deterioration such as fatigue. These life-cycle forecasting tools help to avoid safety issues and optimally schedule maintenance (Kwon and Frangopol 2012). However, the EOC-to-response models, whether they be derived from finite element method (FEM) models, computational fluid dynamics (CFD) models, or from scaled physical models (such as those used by marine engineers in tow tanks), may have inherent limitations such as: 1) not accurately simulating loads leading to inaccurate estimates of structural response; 2) introduce uncertainties due to model assumptions; and, 3) lack sufficient fidelity to capture the full response of a structure (Beck and Katafygiotis 1998; Bertram 2000). For this reason full-scale, on-structure measurement systems are being explored to supplement and inform life-cycle modelling approaches (Hess 2007;

Mottershead and Friswell 1993). In this manner, more accurate or even full-scale empirical relationships between EOC and structural behavior can be determined. The incorporation of explicit accounting of EOCs in more traditional damage detection algorithms is also an area in SHM that needs to be addressed (Worden et al. 2007).

There are several examples of SHM field applications to civil infrastructure. These include monitoring of dams (Kronenberg et al. 1997; Sjödahl et al. 2008; Wu and Su 2005), tunnels and mines (Nutter Jr. and Aldridge 1988; Okundi et al. 2003), and buildings (Jeary et al. 2001; Li et al. 2007). Offshore structures received research attention for a short amount of time (Spidsoe et al. 1980) but due to uncertainties and lack of an integrated industry standard, this area has not been heavily researched (Brownjohn 2007), other than a study by Mangal et al. (2001). Applications of wired continuous *in situ* monitoring systems on rotating wind turbines has not been practical outside of the lab (Bouzid et al. 2014). Focusing on bridges, although literature can track back to basic vibration monitoring of the Golden Gate and Bay Bridges (Carder 1937), this time-period clearly did not possess technology to a level that would permit continuous/digital monitoring. As technology advanced over the years additional systems were implemented that recorded data with magnetic film strips (Abdel-Ghaffar and Scalan 1985; Rainer and Van Selst 1976; Kumarasena et al. 1989; Mclamore et al. 1971). Brownjohn et al. (1994) implemented one of the first SHM systems to incorporate computerized data acquisition of measurements (*i.e.*, digital recording of data). The advent of computerized DAQ systems for SHM increased the rate at which they were implemented. Resulting in a number of significant long-term SHM systems (Andersen and Pedersen 1994; Barrish, Jr. 2000; Cheung et al. 1997; Cross et al. 2013; Sumitoro et al. 2001). In fact, in China there has been extensive

implementation of SHM systems on long-span bridges (Ko and Ni 2005; Wong 2007). However, these systems are "wired" systems (*i.e.*, each sensor is tethered to a central power source and data acquisition system (DAQ)). These wired systems can lead to longer installation times and higher installation costs (making them prohibitive for many infrastructure assets) as compared to alternative (wireless) monitoring systems (which are discussed subsequently). Additionally, these SHM systems focus largely on global monitoring and lack localized methods to detect and assess damage.

In the naval community there exist select examples of full-scale monitoring systems that have been implemented. Davis et al. (2005) and Thomas et al. (2003) instrumented a 282.2 feet (86 m) commercial catamaran with a permanent wired hull monitoring system with the purpose of capturing hull responses to slamming. Cusano, Monti and Velasco (2003) instrumented a 421.9 feet (128.6 m) commercial mono-hull with a wired hull monitoring system to measure ship motions, pressure on the hull and strain in hull elements. In addition to commercial applications, the military has adopted hull monitoring to study their vessels. The U.S. Navy installed a permanent hull monitoring system on the all-aluminum *HSV-2 Swift* which is a 321 feet (98 m) wave piercing catamaran designed for high-speed operations (Brady, Bachman, Donnelly & Griggs 2004; Jacobi, Thomas, Davis & Davidson, 2014). Likewise, full-scale measurements were performed on the hull of the all-aluminum *FSF-1 Sea Fighter*, a 262.1 feet (79.9 m) catamaran designed as a high speed LCS vessel for the U.S. Navy (Fu, Fullerton & Minnick, 2007). However, these deployments were all wired systems (adding to their cost and invasiveness), often required long installation times and gained insight only for very large vessels.

1.3.2 Wireless Monitoring Systems

Despite the great value offered by continuous monitoring systems, such systems have been limited in their application due to high installation times and costs (Seakeeping Committee 2007; Spencer et al. 2016). To lower installation costs, enable denser sensor networks and broaden the scope of feasible applications, wireless sensing technologies have emerged as a viable option (Lynch and Loh 2006). In essence, wireless sensors avoid the use of wires required by traditional tethered data acquisition (DAQ) systems by transmitting the data from the sensor via a wireless radio and providing battery power instead of a wired power-source. The wireless radio can either be directly integrated with the sensor or attached to a small DAQ system that interfaces with the sensor. Likewise, the sensor itself can be self-powered (using energy harvesting techniques) or the small DAQ system to which the sensor is attached may contain batteries that either need replacement or employ energy harvesting techniques (*e.g.*, solar panels). The combination of the wireless DAQ system, power-source and sensor is often referred to as a wireless sensing unit (WSU) or wireless sensor node. In most cases, these nodes transmit data wirelessly to an onsite low-power server, which organizes the data from all nodes and subsequently either archives the data or transmits the data via a cellular modem to owners for further analysis and archival. Notwithstanding the advantages that wireless sensing techniques provide, there is a very limited number of full-scale applications of wireless sensor networks due to hardware and software improvements that still need to be made to improve their scalability (Spencer et al. 2016).

There are successful examples of wireless SHM systems used in the civil engineering field. Maser et al. (1996) were perhaps the first, as they applied a wireless

system for monitoring highway bridges. Shortly thereafter, the Alamosa Canyon Bridge, which had been previously instrumented and had well documented model properties, was used to validate the performance of multiple wireless sensor prototypes both of which collecting acceleration measurements (Lynch et al. 2003; Straser and Kiremidjian 1998). Additional short-term deployments collecting acceleration data on bridges include (Gangone et al. 2011; Glaser 2004; Lynch 2005; Lynch et al. 2006; Wang et al. 2007; Weng et al. 2008; Whelan et al. 2007). More recently, the expansion of these global modal analyses to include known vehicle load, position and dynamic response synchronized with the dynamic response of the bridge, known as vehicle – bridge interaction, has been explored (Kim et al. 2011; Kim and Lynch 2012). There are few examples of non-acceleration based measurement systems; Bennett et al. (1999) embedded strain gages and temperature sensors into highway pavements and collected the data with a wireless sensing unit, and (Galbreath et al. 2003) used displacement transducers to measure truck induced bridge vibrations. However, no measurable insight or action items were informed. Further short-term wireless monitoring systems not instrumented on bridges but on other civil engineering structures include a system installed on a theater balcony (Zimmerman et al. 2008) and the monitoring of wind turbines (Bouzid et al. 2014; Swartz et al. 2010). However, these and all of the previously cited wireless examples were short-term installations, most of which focused on global modal analyses informed by acceleration measurements, with some serving simply as a validation that the wireless sensors communicated successfully.

There are examples of long-term wireless monitoring systems installed on buildings (Chintalapudi et al. 2006; Ou et al. 2005) as well as on bridges (Jang et al. 2010; Kim et al.

2007; Kurata et al. 2012; Meyer et al. 2010; O'Connor et al. 2014; Spencer et al. 2016; Zhang et al. 2016). However, these studies have largely focused on modal parameters that were extracted from acceleration measurements to characterize global properties; meaning, these approaches lacked highly localized response measures well suited for damage identification. Park et al. (2013) implemented a wireless global and local monitoring strategy to monitor static load progression and static structural response of a building during construction.

Despite their cost saving advantages that enable more widespread use of full-scale monitoring, there are limited examples of wireless monitoring systems being deployed on naval vessels. One such example was, a deployment on the *FSF-1* which was used to validate the installation of a wireless hull monitoring system to record ship accelerations and strain responses during sea trials (Swartz et al. 2012). The results from this deployment were used to execute system identification analyses. Although the system provides a powerful and reliable method to collect data wirelessly, it lacked in providing a framework for analyzing damage, forecast life-cycle or to help in decision-making.

Even though wireless monitoring systems have been successfully deployed and tested, most systems have made extensive use of accelerometers to measure structural vibrations and global modal properties. To expand the functionality of wireless monitoring systems, there remains a need to include more local sensing methods in system designs. In doing so, monitoring systems can be designed with greater sensitivity to damage which is inherently a local phenomenon. However, this research area is in its infancy and still faces many obstacles before it can be reliably applied or installed in the field (Dong et al. 2015). For example, there exist few low-power, wireless interrogation techniques for fiber optic

sensors, set up for 1D linear strain sensing (Moyo et al. 2005). Furthermore, wireless data acquisition is still lacking for many of the 2D sensing methods such as EIT spatial sensing techniques using sensing skins and ultrasonic guided waves (Hay et al. 2006; Huang and Loh 2015).

1.3.3 Data Analysis Frameworks

Data support systems (DSS) have been around for a number of decades (Gorry and Scott-Morton 1971). The term describes any automated, computerized system that helps managers arrive at an optimum decision. Over the years, its use has primarily been in business intelligence (Power 2008). Nonetheless, its function is useful across all industries and is used by infrastructure asset managers as well (Garza et al. 1998). A powerful form of DSS is a data-driven DSS that uses observed data as input to the automated decision algorithm. In the case of business intelligence, the input data can often be relatively straightforward to target, observe and analyze. For example, in retail, one objective is to increase sales; so the model can be setup to correlate a number of customer habits to sales numbers. However, with the advent of NDE techniques and to a greater extent SHM techniques, data available to inform data-driven DSS for infrastructure management has the potential to significantly increase. To distinguish the data-driven DSS approaches for application to infrastructure management the term data-to-decision (D2D) (as it is sometimes referred to in the civil engineering industry) is used for the remainder of this dissertation. Towards the goal of implementing more efficient and safer maintenance strategies, D2D frameworks are being developed to enhance SHM techniques in their ability to use data to assist in structural performance assessment and damage detection (Farrar and Lieven 2007) as part of the decision-making processes (Zonta et al. 2014). By

combining multiple data sources (*i.e.*, global and local monitoring, visual inspection, structural analyses), an automated D2D framework can be developed (Alampalli and Ettouney 2010). An early example in the bridge community is the use of data to inform load rating methods that aim to assess bridge capacity. Many of the D2D frameworks have been shifting to reliability-based approaches, in place of traditional structural capacity rating, to evaluating the safety of an asset because they address uncertainties in load estimation and are capable of including multiple hazard and load types (Akgül and Frangopol 2004; Ghosn 2010). Despite the great need for and benefits gained from data-driven D2D, the number of successful real-world implementations of objective D2D systems is very limited due to the requirement of including non-ideal environmental and operating conditions (EOCs) outside of a lab setting (Catbas et al. 2008; Sohn et al. 2003).

1.3.4 Key Areas for Improvement

It can be concluded that although SHM technologies have been evolving rapidly in recent years, they are often generic, typically only include global measurements and lack the ability to inform asset management decisions. Likewise, NDE technology is valuable in its own right and can provide detailed localized information; however, it is largely a manual process that is costly and only occurs periodically. Finally, there exist many D2D theories and frameworks. However, for the most part, these are not based on actual sensor data that has been collected and confidently processed to inform specific, critical decisions. Therefore, for SHM technologies to add value and justify the investment required for their application, these three fields must be fused, in a sense. All three can be utilized to their fullest extent by targeting specific asset management decisions of interest and structuring the sensing and analysis approach with a strategy that is focused on the end goal of

furnishing decision-making insight. Depending on the desired decision or parameter of interest, various SHM techniques, both global and local can be implemented. Furthermore, NDE techniques can be modified such that they are capable of continuous SHM application, which can further empower SHM data processing techniques. SHM has great potential to improve infrastructure and consequently, society, but can only do so if utilized properly. Moreover, it must be robust, reliable and cost-efficient so its adoption is economically feasible. More importantly, it must be focused in its design and application such that it furnishes actionable insight and informs asset management decisions.

1.4 Research Objectives and Contribution to the Field

This dissertation aims to address the strong need for comprehensive (global and local sensing approaches) monitoring architectures that drive a D2D framework for asset management. The overarching goal is to develop and test a D2D framework that furnishes actionable insights by integrating data analyses and sensor measurements, both global and local, in an automated system. The dissertation accomplishes this goal by developing a modular wireless monitoring system architecture that can be deployed to collect both global (*e.g.*, accelerations) and local (*e.g.*, component strain) structural responses. While generic wireless monitoring systems have been deployed on large structures, this dissertation emphasizes wireless monitoring systems designed to specifically drive a decision-making process.

The key contributions are the development of two wireless monitoring systems and corresponding D2D frameworks (one for short-term deployment on a naval vessel, and the second for a long-term permanent deployment on a railroad bridge), the development of a

novel thermal imaging technique and a wireless device capable of driving multiple spatial sensing approaches. The short-term deployment is unique in its ability to be rapidly deployed, it adds to the limited body of knowledge of on-board measurement systems (especially to the extremely limited examples of on-board wireless systems), it is the first to monitor such a small, complex *Boat* class vessel and it achieves a complete D2D framework. The permanent monitoring system also achieves a complete D2D framework but must be more robust than the rapid-to-deploy system and has a novel approach to automatically determining relative tautness between eyebar elements and it provides an automated alert system. The proposed thermal imaging technique is the first low-cost, robust, non-invasive thermal spatial sensing technique of its kind and is also capable of being deployed wirelessly. The multi-functional wireless device used to drive the thermal imaging technique is crucial to the thermal technique, as well as other spatial sensing techniques (namely the EIT technique validated wirelessly herein), being capable of permanent wireless installation (recall wireless application drives the cost down and increases the feasibility of an SHM system being adopted into practice).

1.4.1 Wireless monitoring systems and D2D frameworks

Two applications are considered herein: short-term monitoring of an aluminum ship hull and long-term monitoring of a long-span railroad bridge. In the short-term hull study, the hull monitoring system is designed to feed quantitative data to a life-cycle analysis considering the fatigue damage accumulation of a critical ship hull element. The D2D framework for this study requires explicit accounting of the hull EOCs in addition to monitoring ship responses to sea wave loads. Hence, the hull monitoring system is designed to measure over short deployment periods the global motions of the ship to

estimate the ship EOC state. Then, local strain measurements are taken of a fatigue critical hull element to monitor fatigue accumulation. In this manner, forward-looking life-cycle analysis of the ship can now explore the fatigue life of the hull using EOC – fatigue accumulation models/relationships derived from wireless hull monitoring data.

The second application considers long-term wireless monitoring of a railroad truss bridge to derive a D2D framework for a railroad. Here, the D2D framework aims to accomplish two tasks: rapid alerting of overloaded or disproportionally loaded structural elements and identification of hazard events (specifically ship collisions and seismic events). To accomplish this goal, a trigger-based permanent wireless monitoring system that targets specific critical components specified by the bridge owner is implemented. The trigger is used to conserve energy by limiting system on-time and data collection to load events: 1) train crossings; 2) ship collision with the bridge pier; and 3) seismic events. The second aspect of the system is the development of an automated analytical framework that addresses the component of primary monitoring concern, which is a fatigue critical eyebar element. The eyebar element is a tensile element that consists of six (6) parallel eyebar links. Because they experience large live loads (*i.e.*, heavy trains crossing the bridge), it is imperative the eyebar links see relatively equal tensile load. If one eyebar takes a disproportionate share of the tensile load, it can see an acceleration of fatigue accumulation which may result in major failure such as on the San Francisco – Oakland Bay Bridge (Gostautas and Tamutus 2015; Reid 2010). Normally, the railroad relies on visual inspectors to physically shake each eyebar and time their vibrations to crudely assess relative tautness in parallel eyebar links (UPR 2013). The permanent monitoring system installs accelerometers on the eyebar links to measure transverse accelerations. Using

automated algorithms based on frequency domain processing, eyebar relative tautness is tracked with alerts sent to the bridge owner when one eyebar begins to take a disproportionate share of the element tensile load.

1.4.2 Incorporation of spatial sensing into wireless monitoring systems

The frameworks developed for the field applications discussed in this dissertation are very valuable in assisting in decision-making. Nevertheless, there is often a need to directly observe damage. This can be done through spatial sensing techniques, or as they are sometimes termed, image reconstruction techniques. Image reconstruction provides a visualization of the component of interest and potential damage (Lin and Yuan 2001). Such a visualization can be extremely valuable in the decision-making process and can make D2D frameworks even more powerful. Automated frameworks similar to those discussed above, can provide alerts and quantitative life-cycle forecasting, while the spatial sensing results not only increase the area over which these analyses can be performed, they also allow the bridge owner to actually see the state of the component or area over which spatial interrogation is executed. This likely eliminates the chance of damage going undetected and improving the owner's ability to make informed decisions.

Clearly, in many instances spatial sensing of critical components is required to comprehensively assess and more accurately provide actionable insight. One such method of spatial reconstruction is infrared (IR) thermography, which supplies a known heat source (*i.e.*, laser or heat lamp) to a specimen and records the temperature change for each pixel of the IR image as heat propagates across the specimen. This differentiates itself from ultrasonics because the heat propagates across the specimen (and potential damage) in a diffusive manner (whereas ultrasonic waves follow refractive properties, which is not

feasible for some surfaces and materials that do not transmit sound well enough and for complex geometries that mingle refraction waves too much for an image to be reconstructed). Electrical impedance tomography (EIT) is also a diffusive process; however, its implementation requires the integration or application of sensing skins which is an intricate and potentially costly process that is not feasible for some field applications. Nonetheless, even with its advantages over other spatial sensing techniques, however, they lack deployment robustness and are high cost (Maldague 2002; Schlichting et al. 2012).

Therefore, this dissertation develops a novel heat transfer-based spatial damage detection method that leverages the low-cost of heaters and temperature sensors in order for the approach to be feasible for permanent installation; both in terms of robustness and cost. The derived method is similar to that of X-ray computed tomography (CT). However, the theories for X-ray CT must be adapted to properly represent heat transfer as well as account for the relatively large and immobile sensor spacing used on a structure (i.e., there is a finite number of heaters/sensors permanently installed around the perimeter of the area of interest). A finite element method (FEM) model is used to verify the analytical derivation of individual steps within the method as well as simulate results for both damaged and undamaged scenarios of aluminum plate specimens to validate the damage detection technique. Experimental results from both damaged and undamaged aluminum plate specimens are used to validate the FEM model and to justify theoretical assumptions. Finally, experimental results are used to fully validate the accuracy of the proposed thermal CT method.

For the proposed thermal CT to be fully wireless it requires the development of a multi-channel wireless actuator (to supply heat) and sensor. Furthermore, the

aforementioned EIT technique (Huang and Loh 2015; Pyo et al. 2011) needs further development of a wireless interrogation device in order to be fully wireless and capable of multi-channel impedance analysis (actuation and sampling frequency need increased). Therefore, a multi-functional, multi-channel wireless impedance analyzer is proposed. The device is required to: 1) function completely wirelessly (*e.g.*, power, output control, measurements, data transmission); 2) output DC and any AC waveform (*e.g.*, zero-mean, non-zero mean, sine, triangle) in the kHz range; 3) choose between current controlled and voltage controlled output; 4) measure voltage and current, with analog-to-digital conversion (ADC) in the kHz range; 5) perform electrical impedance spectroscopy with a four-probe sensing approach; 6) output (source), sink and perform measurements at 32 addressable channels, and 7) have an adjustable output impedance to match that of the specimen being interrogated. With the listed functionalities this device is tested by wirelessly performing fully automated accurate electrical impedance spectroscopy (EIS) measurements, wireless electrical impedance tomography (EIT) experimental tests and wireless thermal CT experimental tests.

1.5 Dissertation Outline

The key objective driving the dissertation is to address the strong need for comprehensive (global and local sensing approaches) monitoring architecture that drives a D2D framework for infrastructure asset management. This is highlighted in the dissertation outline shown in Figure 1.2 which illustrates how each chapter fits in with the overarching goal. This goal is achieved by targeting a specific set of decisions of importance to the asset owner as the objective for a monitoring system and designing the

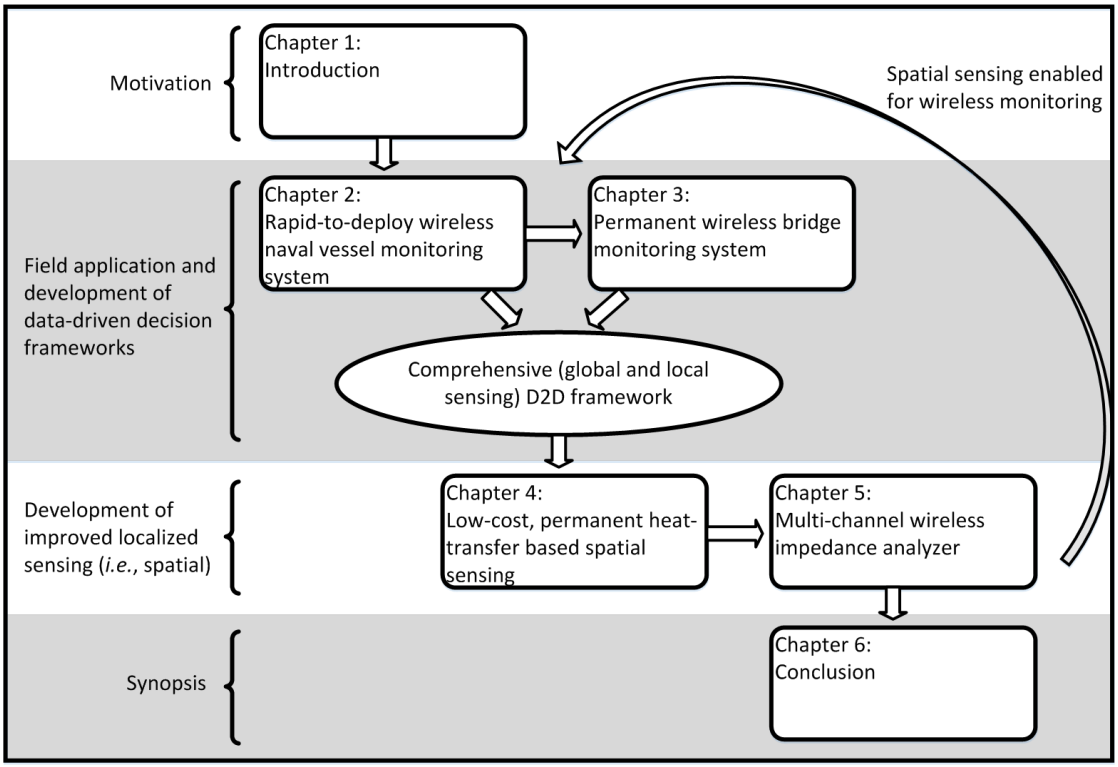

Figure 1.2 Diagram of key topics and outline of dissertation.

instrumentation and measurement strategy, and analytical framework such that it obtains quantifiable insight that informs critical decisions. This D2D approach is developed and tested by integrating data analyses and sensor measurements, both global and local, from wireless, cost-efficient, field application of two monitoring systems manner.

Chapter 2 presents the successful deployment of a "first-of-its-kind" short-term wireless hull monitoring system on a United States Coast Guard vessel at sea. The vessel selected is a high-speed aluminum vessel for which long-term fatigue failure is a concern. This is coupled with an innovative data driven analytical framework that provides meaningful insight that can be used in life-cycle forecasting and maintenance scheduling by the USCG. Global acceleration (*i.e.*, inertial measurements) are used to relate sea EOC state to ship response. In turn, ship motions are related to local fatigue measurements on a

pre-identified hull stiffener element of primary concern. Thus, real sea conditions and real damage accumulation (as opposed to modelled/simulated) are quantified and available for life-cycle decision-making.

The success of the USCG deployment and life-cycle decision framework is built upon in *Chapter 3* by expanding the global and local instrumentation approach from short-term to long-term by installing a permanent wireless monitoring system on a multi-hazard long-span railroad bridge. The long-term nature of this deployment requires more robust instrumentation and power management strategies. The aim of the monitoring system is to aid the bridge owner in making informed decisions about specific areas of concern. In the case of this particular bridge the owner identifies excessive loading events (*i.e.*, train crossing, ship collision, earthquake) and accelerated fatigue accumulation in the eyebar element as items that the sensing strategy and data processing should inform. Towards this end, the bridge has tri-axial accelerometers for use in global modal analyses as well as multiple hanger and truss components instrumented with strain gages to infer load information. These global sensing data are processed automatically to alert the bridge owner if certain load thresholds have been exceeded. Lastly, a local approach is employed on a vertical eyebar truss component of key importance to bridge reliability and safety. A similar alert system is employed that monitors any major changes in load distribution of the eyebar element.

Both of field applications reinforce the need to improve localized sensing approaches such as spatial sensing, or image reconstruction. Therefore, *Chapter 4* discusses the development of a novel, low-cost, wireless, permanently installable spatial sensing technique, which uses heat transfer physics to detect cracks in metallic structures.

A thermal computed tomography approach is developed to reconstruct the 2D image of the instrumented structural component to identify local damage directly.

In order for this new spatial sensing technique to be wireless, a multi-functional, multi-channel wireless impedance analyzer is developed and discussed in *Chapter 5*. This device has 32 addressable channels that connect to the sensors and actuators of a sensing setup. Each channel is capable of both sensing and actuation. The output of the device can be current or voltage controlled and DC or AC of any waveform while the input achieves high ADC sampling rates and transmits the data wirelessly. Not only does this device enable the wireless thermal computed tomography technique of *Chapter 4*, but also, its multi-functional output enables the wireless application of other spatial sensing techniques that are being developed in the community (*e.g.*, EIT).

The dissertation concludes in *Chapter 6* with a summary of the completed work, contributions and how this work can be extended to additional applications and areas where extensions of this research could be beneficial.

CHAPTER 2

A NOVEL METHOD TO ANALYZE AND PREDICT FATIGUE IN NAVAL VESSELS USING A RAPID-TO-DEPLOY SHORT-TERM WIRELESS MONITORING SYSTEM

This chapter proposes a wireless full-scale hull monitoring system that is quick to install as a short-term monitoring solution. On-board hull measurements have the potential to increase the accuracy of ship response predictions at a lower cost than computer simulation or towing tank models. The performance of the wireless hull monitoring system is validated on the all-aluminum United States Coast Guard (USCG) Response Boat-Medium (RB-M). The hull monitoring system is designed to measure global ship motions and local hull strain responses during high speed operations and in harsh weather conditions. An analytical framework is developed to extract sea states from inertial measurements recorded at the ship center-of-gravity and in a bow compartment. To assess the fatigue life of the hull during harsh weather operations, response amplitude operators (RAOs) are empirically derived to map sea states to root mean square accelerations and strain cycles measured from a critical high stress hull element. A RAO that maps sea state to consumed fatigue in the hull, so termed a consumed fatigue operator (CFO), is presented for life-cycle asset management. The study reveals reliable and accurate hull monitoring during a one week sea trial. RAO and CFO fit to hull response data are proven to provide accurate estimates of hull behavior.

2.1 Background

Modelling the behavior and forecasting the health of naval vessels is vitally important in ensuring ships are safe and cost-effective to operate. Detailed knowledge of hull performance during a vessel's service life can lead to improved decision-making by vessel operators, especially surrounding issues such as optimization of maintenance strategies, extending ship service lives, and expanding operational envelopes. To provide a quantitative basis for these decisions, the measurement of hull behavior during seaway loading is needed. To experimentally observe hull behavior, hydrodynamic model testing can be performed using scaled vessel models in a towing tank. Such methods measure seaway loads on the hull and empirically derive response amplitude operator (RAO) functions mapping hull responses to sea states. However, model testing in towing tanks can be costly and may not accurately simulate all seaway loads such as local hull loads that occur during wave slamming (Bertram 2000). In addition, hull models typically do not provide a basis for mapping hull loads into local component responses to assess the long-term performance and health of the hull. More importantly, it is very hard to sense loads at model scale. Pressure transducers only give point loads, not spatial loads, and models typically do not have structural systems that can measure integrated loads (*e.g.*, stiffener element). Alternatively, computational fluid dynamics (CFD) and finite element method (FEM) numerical modelling can be coupled to simulate hull responses to sea loads (Piro 2013). This approach is also challenging due to the need for complex models as defined by a large number of nodes and the need for extensive model calibration.

To overcome the limitations of experimental tank testing and numerical simulation, hull monitoring systems can be installed in operational vessels to observe hull responses to

sea loads and to assess the relationship between structural behavior and long-term hull health. Owners such as the United States Navy (USN), United States Coast Guard (USCG) and commercial shippers are all considering the adoption of hull monitoring technologies to acquire response data during operations at sea. For example, the USN is exploring permanent hull monitoring to track the performance and health of the littoral combat ship (LCS) fleet (Hess 2007). The LCS fleet are high-speed aluminum ships with unique hull designs; due to large slamming and whipping loads on their hulls during high speed operations, there is a concern about the potential for premature fatigue failures (Collette & Incecik, 2006; Drummen & Holtmann, 2014; Kapsenberg, 2011; Kwon & Frangopol, 2012). Similarly, the USCG is interested in monitoring the performance of their high-speed aluminum vessels in order to evaluate the expansion of their operational envelopes (Kowalyshyn & Metcalf 2006). Especially challenging for the USCG is the relatively small size of their high-speed vessels; the response of a smaller vessel to seaway load is highly complex. For example, openings, windows and compartments in a small vessel may play a larger role in the hull response compared to the same detail in a larger vessel such as a container ship. Thus, yielding numerical modeling, without validation, nearly useless. Hence, instrumentation of operational vessels during high speed operations at sea is desired. For example, the USCG has explored an on-board hull monitoring system that can be used to quantify the slamming-induced stress levels in the bow of the 45 foot (13.7 m) Response Boat – Medium (RB-M) (Salinas 2012).

Hull monitoring is a mature technology that has been in use for more than half a century. One of the earliest examples of a full-scale hull measurement systems was the installation of sensors interfaced to rolling drum recorders on Dutch destroyers in 1957

(Warnsinck & Denis 1957). By the 1970s, digital hull monitoring systems were in use making data collection more convenient and reliable (Dickey, DeLong & Gregov, 1976). Although full-scale hull measurements are beneficial, the high costs of installing hull monitoring systems has limited their number in practice. This situation has recently begun to change due to lower cost sensors emerging (*e.g.,* solid state sensors) and the availability of more convenient communication options (*e.g.,* use of existing shipboard networks for sensor data communication). There are examples of using full-scale measurements to determine sea conditions (environmental operating conditions (EOCs)) (Nielsen 2017); however, these are carried out on much larger vessels or off-shore structures whose response is not as complex or nonlinear as smaller vessels. Furthermore, there have been many recent examples of hull monitoring to measure ship motions and hull responses. Cusano, Monti and Velasco (2003) who instrumented a 421.9 feet (128.6 m) commercial mono-hull with a wired hull monitoring to measure ship motions, pressure on the hull and strain in hull elements. In another study, a 282.2 feet (86 m) commercial catamaran was monitored with a permanent wired hull monitoring system whose design was tailored to capture hull responses to slamming (Davis, Watson & Holloway, 2005; Thomas, Davis, Holloway, Watson & Roberts, 2003). The military has also adopted hull monitoring to study their vessels. The U.S. Navy installed a permanent hull monitoring system on the all-aluminum *HSV-2 Swift* which is a 321 feet (98 m) wave piercing catamaran designed for high-speed operations (Brady, Bachman, Donnelly & Griggs 2004; Jacobi, Thomas, Davis & Davidson, 2014). To correlate ship responses to seaway conditions, the *HSV-2* was also equipped with a radar wave-height sensor. Similarly, full-scale measurements were performed on the hull of the all-aluminum *FSF-1 Sea Fighter*, a 262.1 feet (79.9 m)

catamaran designed as a high speed LCS vessel for the U.S. Navy (Fu, Fullerton & Minnick, 2007). Like the *HSV-2*, a radar system was installed in the *Sea Fighter* bow to measure wave heights. The *FSF-1* was also used by Swartz et al. (2012) to validate the installation of a wireless hull monitoring system to record ship accelerations and strain responses during sea trials in the Pacific Ocean.

While permanent hull monitoring systems continue to grow in popularity, there remains a need for short-term hull monitoring deployments where sensors are deployed for short periods of time (*e.g.*, weeks) to assess ship behavior in a variety of operational states. Due to their short-term installations, such systems must be low-cost, easy to install and not interfere with crew and/or vessel operations. Systems that meet these criteria could be valuable for validating design assumptions, generating data to calibrate numerical models, and to gain empirical evidence of structural behavior during extreme loading conditions that would otherwise be difficult to observe in hydrodynamic towing tank modelling or to accurately simulate using numerical models. To maximize the benefit of short-term hull monitoring, such systems must have a means of logging ship motions that can be used to estimate ship environmental and operational conditions (EOCs). The collection of EOCs and hull responses can then serve as the basis for the derivation of RAO functions that provide a mapping of sea state and its associated loading to specific hull responses that are critical to the accumulation of damage in a hull. Such a system would cost-effectively address the needs of operators that seek to quantify the performance of their fleets for future life-cycle health analysis. For example, an owner like the USCG could utilize empirically derived RAO that predict strain levels in fatigue critical hull elements to predict the life-

cycle accumulation of fatigue in their high-speed aluminum hulls based on estimated operational profiles.

The overarching goal of this chapter is to develop a cost-effective approach to analytically assessing the performance and fatigue life of operational high speed aluminum vessels using short-term hull monitoring. A key study objective is the development of a rapid-to-deploy wireless hull monitoring system that can be used to acquire response data from ship hulls during seakeeping trials. The wireless hull monitoring strategy addresses the cost and installation issues associated with traditional wired hull monitoring systems. Another study objective is the formulation of an analytical framework that processes inertial measurements of the monitored hull to infer wave heights, wave encounter frequencies and ship heading. These EOC then serve as the basis for empirically calibrating RAO functions for the prediction of hull responses for each EOC state. The chapter highlights how the developed framework can quantitatively assess the consumed fatigue life of the hull based on hull measurements for subsequent life-cycle assessments and decision-making.

Figure 2.1 presents the proposed analytical framework that aims to improve on current practice. Typically, an EOC for a given vessel is determined based on the number of hours, or percentage of time, the vessel is expected to operate in given sea conditions. For each of these unique sea condition bins a RAO is determined through wave tank models or computer model simulations. These RAOs can then be used with more complex models to determine stresses and corresponding fatigue which can be used in life-cycle analyses. The proposed method presented in this paper directly relates sea conditions to ship motions via empirical RAOs; it also empirically relates ship motions to strain and corresponding

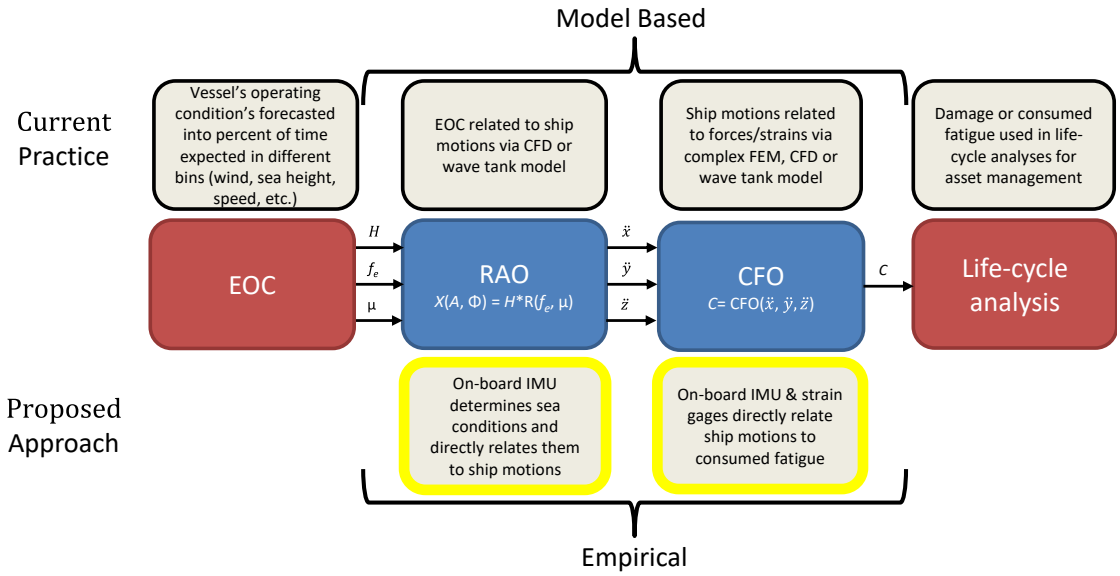

Figure 2.1 Conceptual flowchart of current design and life-cycle analysis practice and proposed improvement.

consumed fatigue (consumed fatigue operator (CFO)). Therefore, the need for wave tank or computer models is avoided and direct measurements are used to develop RAOs and CFOs. The proposed method could be implemented as follows: 1) perform short-term sea trials on a single vessel to develop RAOs and CFOs; 2) forecast EOC for same vessel or identical vessels operating elsewhere; 3) use empirical RAOs and CFOs to more accurately predict stresses and consumed fatigue for input into design and life-cycle analyses. The study presented herein acts as a proof-of-concept that on-board measurements can be gathered efficiently and used as part of an improved analytical framework. The development of life-cycle analyses are not part of this study but clearly stand to benefit from the improved determination of RAOs and CFOs.

The study advances the body of knowledge in two significant ways. First, the study validates the use of short-term wireless hull monitoring for fatigue assessment using the RB-M high speed aluminum hull which is from the *Boat* vessel classification (less than 65 feet (19.8 m)); previous studies in the literature have primarily focused on significantly

larger vessels. Second, the study provides a data-driven analytical framework for the assessment of seaway EOCs and the empirical derivation of RAOs and consumed fatigue operators (CFOs) required for life-cycle analysis of the vessel. The outline of this chapter is as follows. First, the chapter describes the wireless monitoring system as designed for short-term (*e.g.*, weeks) deployment on high-speed aluminum hulls. The performance of the proposed wireless hull monitoring system including measurement of hull strain responses of a critical hull element is validated over one week of sea trials using a RB-M vessel. Second, the chapter describes an analytical framework for hull fatigue assessment including extraction of sea EOCs and the development of RAOs and CFOs correlating hull responses to EOC state. Finally, the chapter concludes with a summary of key findings and presents future work that can further advance the framework.

2.2 Wireless Hull Monitoring of 45' Response Boat – Medium

The USCG has a large fleet of multi-functional vessels that are classified as *Boats*. Historically, USCG littoral operations were serviced by the 41 foot (12.5 m) Utility Boat (UTB) which were introduced into service in 1973 (USCG 2016). To modernize its fleet for increased security operations, the USCG started to replace the UTB in 2008 with the higher speed RB-M. Today, the UTB has been completely phased out and the UCSG utilizes 174 RB-M to fulfil its shore-based operations across the United States. The RB-M is an all-aluminum boat designed to operate safely up to 12 feet (3.7 m) seas, 50 knots (93 km/hr) winds, and 50 nautical miles (92.6 km) offshore. The RB-M hull is a deep-V, double-chine planing hull optimized for its high-speed operations and stability. However, the structural integrity of the vessel may be compromised under heavy weather

environments, specifically when significant wave heights exceed 8 feet (2.4 m) (Shepard & Curtis 2010). During heavy weather, the boat could experience excessive roll angles and capsize although the ship is self-righting. Also, the bow structure may experience over-stress due to wave impacts while the deck and side of the deck house could experience local buckling due to excessive global hull bending loads (Debord 2013). The USCG is seeking to expand the operational envelope of the boat to allow it to operate in heavy weather conditions where there is a possibility the ship will experience global accelerations exceeding the 4 g design load and increased slamming events that accelerate consumed fatigue life of hull components (Debord 2013). The USCG is exploring a short-term hull monitoring solution to assess the performance of the hull during rough sea states to determine the accumulation of fatigue damage in a critical hull stiffener element previously identified by FEM numerical simulation as a high stress hull element. The study in this chapter deploys a low-cost wireless hull monitoring system on a RB-M asset stationed at the National Motor Lifeboat School (NMLBS) at Cape Disappointment near Ilwaco, WA (Figure 2.2). The Cape Disappointment RB-M provides the opportunity to record hull responses corresponding to heavier loading conditions due to the rough sea conditions common to the Colombia River where it enters the Pacific Ocean during October.

2.2.1 Wireless Instrumentation Plan

A wireless hull monitoring system offers the advantages of a quick and cost-effective installation in the vessel because the installation of wiring is not needed. The wireless hull monitoring system is designed for the RB-M using the *Narada* wireless sensor node developed at the University of Michigan (Swartz et al., 2005); *Narada* has been

(a)

(b)

Figure 2.2 Instrumented 45' RB-M: (a) departing NMLBS at Cape Disappointment, WA; (b) plane view with frame numbers (WTB = water tight bulkhead).

validated previously for wireless hull monitoring on the *FSF-1 Sea Fighter* as reported by Swartz et al. (2012). A challenge for any wireless hull monitoring system is the compartmentalized nature of hulls with metallic compartments acting like Faraday cages. However, wireless signals can propagate across bulkheads using their various penetrations but the energy levels of the signals are severely reduced. As expected, the thick aluminum

bulkheads between the water-tight compartments of the RB-M significantly reduce the range of the wireless sensors but not to a point that wireless telemetry is infeasible.

The instrumentation plan for the monitoring system installed on the RB-M at the NMLBS is provided in Figure 2.3. The coordinate system used to define sensor locations and orientations in the RB-M is presented in Figure 2.4 (which also shows the POWERSEA model to be discussed subsequently). The boat heading, μ, not to be confused with the yaw, is the ship orientation with respect to the wave front and is defined from negative to positive 90˚ coupled with an indicator if the vessel is travelling in the same direction as the waves or not (*i.e.*, following versus head seas, respectively). The instrumentation plan consists of two sensor types: accelerometers to measure ship motions and strain gages (with thermal compensation) to measure hull responses.

The sensors are installed in the first three forward compartments: bow, survivor cabin, and auxiliary compartment each separated by a water tight bulkhead (WTB) as shown in Figure 2.3. Two tri-axial accelerometers are installed to measure the ship surge, sway and heave (*x*, *y*, and *z*, respectively): one in the bow at frame 14 (Figure 2.5a) and another at the ship center-of-gravity (COG) in the auxiliary compartment at frame 7 (Figure 2.5b). The tri-axial accelerometers are *Silicon Designs 2422-005* (SDI 2016) which have a range of $\pm 5g$, bandwidth of 400 Hz and a sensitivity of 0.8 V/g. The combination of the bow and COG tri-axial accelerometers provide a means of observing the pitch, Θ, of the vessel. An additional tri-axial accelerometer is installed off-center (OC) at frame 7; only the vertical orientation is measured to observe the vessel roll, Φ.

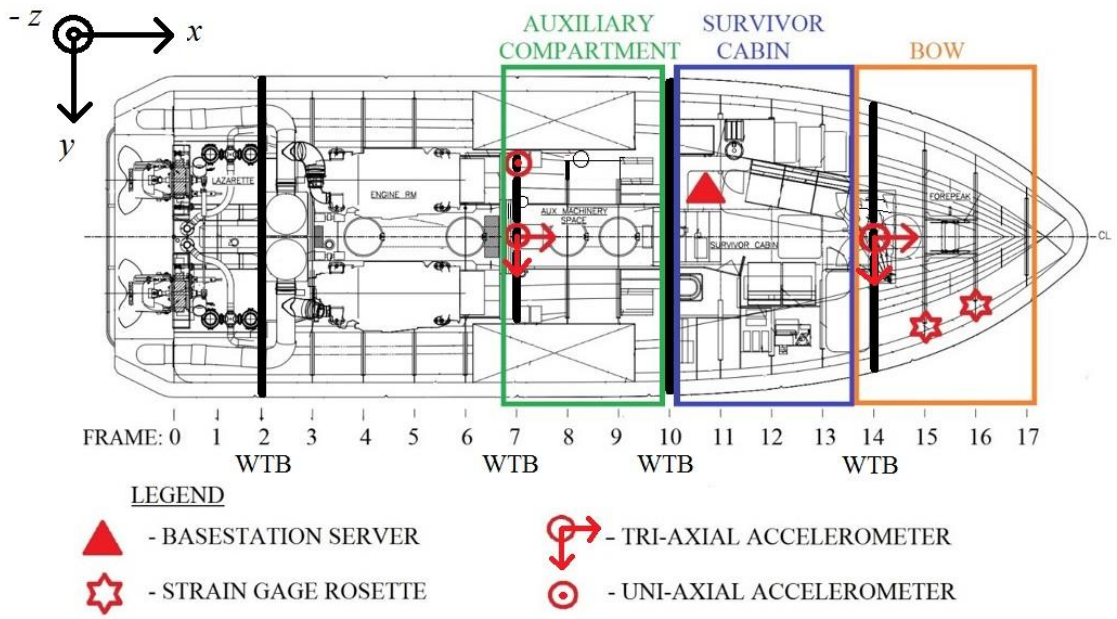

Figure 2.3 Plan view of USCG 45' RB-M with sensor installation locations identified.

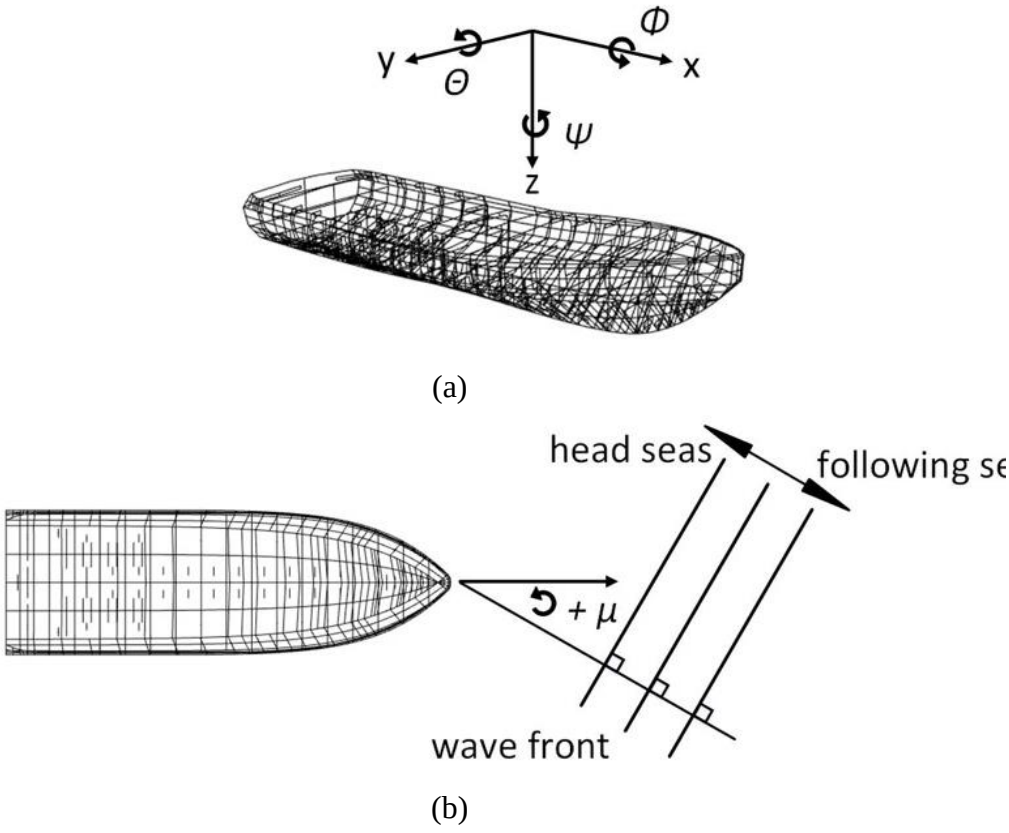

Figure 2.4 Definition of ship coordinate system: (a) six axes of hull response, including surge (x), sway (y), heave (z), roll (Φ), pitch (Θ), and yaw (Ψ); (b) ship orientation (heading, μ) relative to wave motion.

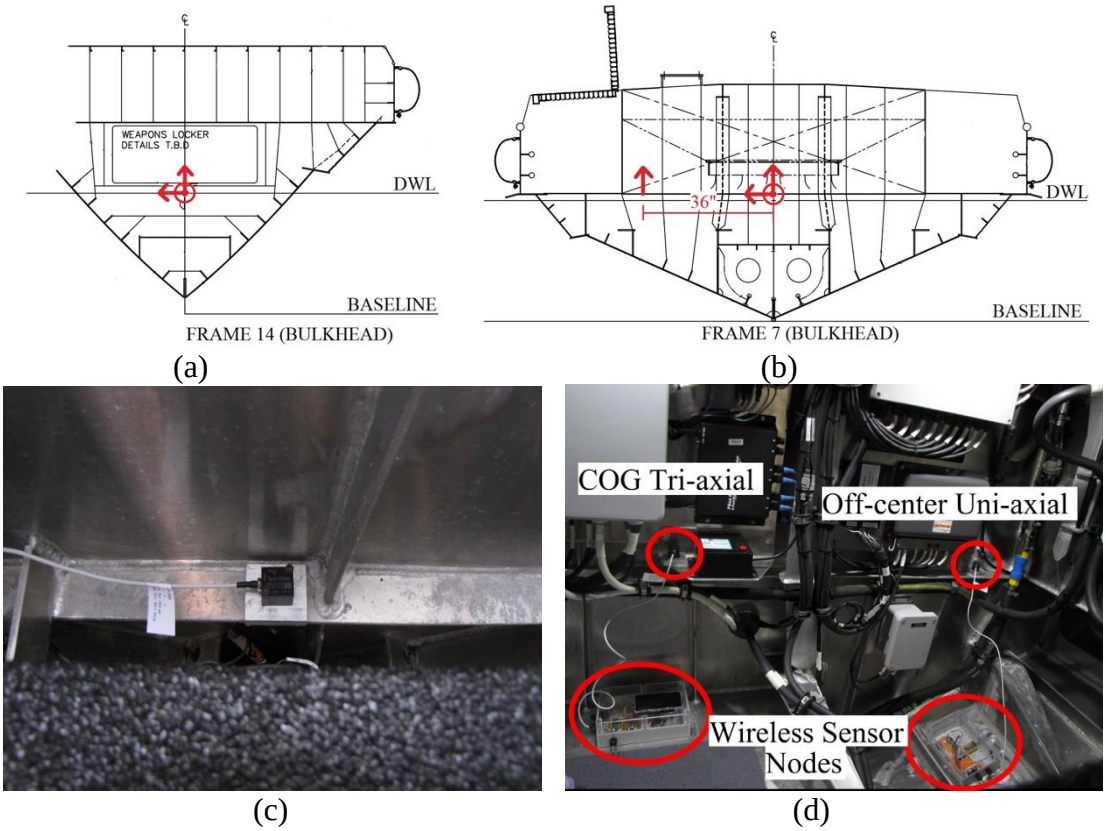

Figure 2.5 Accelerometers installation: (a) in bow at frame 14 cross-section facing towards front of vessel; (b) in auxiliary compartment at frame 7 cross-section; (c) picture of tri-axial accelerometer in bow and (d) at the center-of-gravity (COG) with the uni-axial accelerometer off-center.

A bow stiffener element beneath the lower chine between frames 15 and 16 previously identified by the USCG as a high stress element is instrumented at its two ends with a *Vishay WA-XX 120WR-350* (Micro Measurements, 2016) strain rosette (Figure 2.6). Each gage in the rosette has a nominal resistance of 350 Ω and a gage factor of 2.05. A half-bridge Wheatstone circuit is used for all three channels of each rosette in conjunction with rosettes experiencing only thermal strain to temperature compensate.

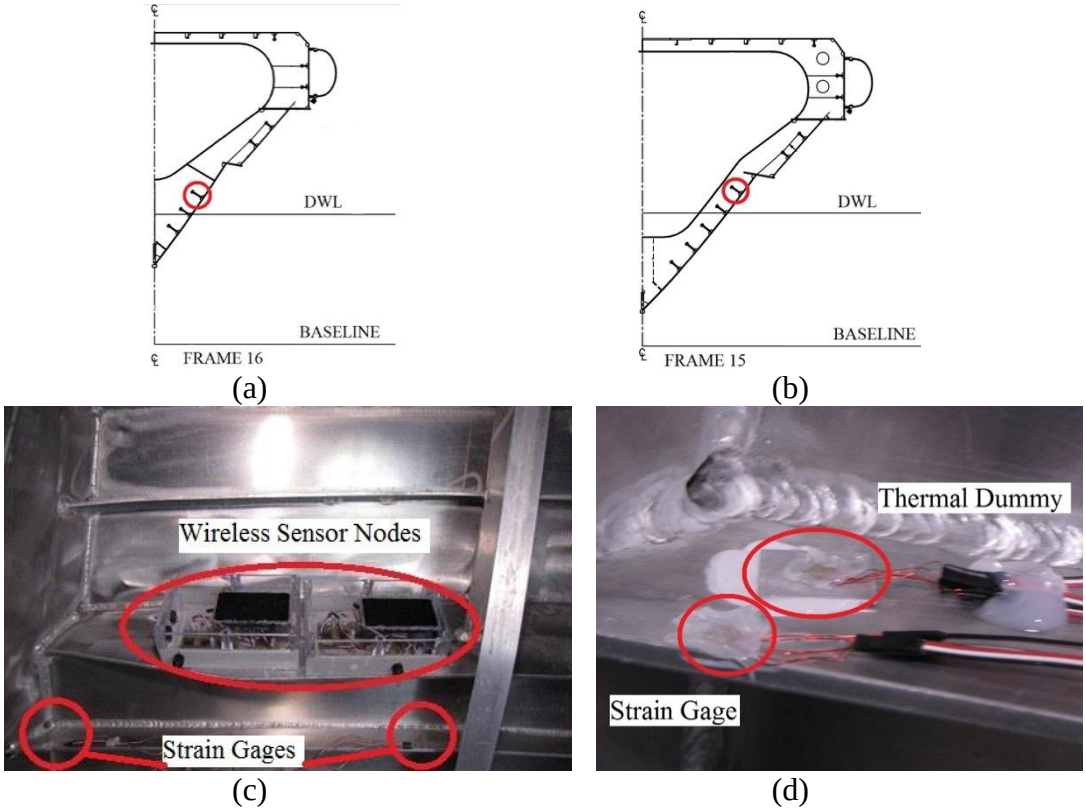

Figure 2.6 Strain gage rosettes in hull bow: (a) frame 16 cross-section facing towards front of vessel; (b) frame 15 cross-section; (c) location of sensors and wireless sensor enclosures; (d) mechanical strain rosette attached with epoxy to stiffener and temperature compensation rosette resting on plate attached with thermal grease.

Each sensing channel is attached to a *Narada* wireless sensor for data acquisition (including 16-bit digitization) and communication to the system basestation using power amplified IEEE802.15.4 transceivers operating on the 2.4 GHz wireless spectrum segment. Each *Narada* node is packaged in watertight enclosure along with batteries and signal conditioning circuitry (*e.g.*, anti-aliasing filter, Wheatstone bridge, and signal amplifier). A requirement of the short-term installation is that it be non-permanent and hence, easily removed. To achieve the objective, each enclosure is bonded to the hull using double sided tape (to hold the enclosure in place) and a small amount of epoxy on the bottom of the enclosure. Silicone caulk is then applied to the perimeter of the enclosure to prevent sliding

and to protect the tape and epoxy from water exposure. The installation procedure consisting of mounting two rosettes, three tri-axial accelerometers, and five (5) *Narada* enclosures is completed in a single afternoon. The sensors and nodes are durable, even on test runs experiencing very high sea states, and easily removed without permanently altering the hull at the end of the study.

Wireless communication directs the data from the *Narada* nodes in the bow and auxiliary compartments to a wireless basestation installed in the survivor cabin (Figure 2.7). Each wireless sensor node is propagating its signal across one water tight bulkhead. The basestation utilizes a PC-104 (WinSystems 2016) single board computer to which an IEEE802.15.4 wireless transceiver (TI, 2013) is attached. The basestation is responsible

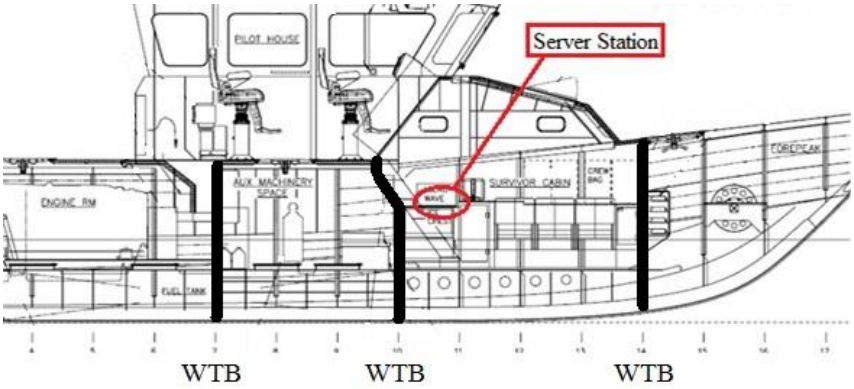

(a)

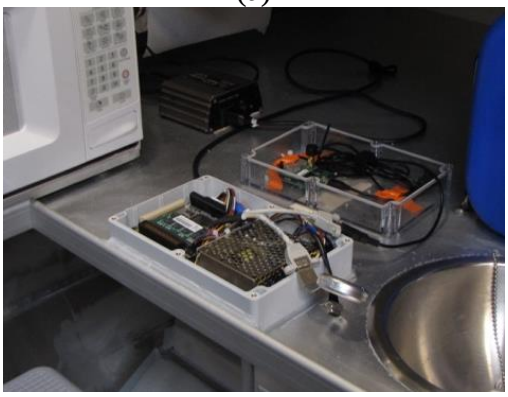

(b)

Figure 2.7 Basestation server in survivor cabin: (a) location; (b) photograph.

for the operation of the hull monitoring system including time synchronization, wireless data collection, data storage, and real-time data processing. The basestation PC-104 runs the Linux-based Ubuntu operating system. The basestation is programmed to collect data nearly continuously while the ship is under operation at sea. The basestation commands the wireless sensor nodes to synchronize to a beacon signal after which they collect data for a prescribed period. Upon completion, the basestation receives the data back from each *Narada* node one node at a time. Data collected is stored at the basestation on a compact flash drive. For the sea trials on the RB-M, the basestation is configured to collect data for 10 minutes with 1 minute following to transmit the data before starting again. This approach ensures the monitoring system is time synchronized repeatedly to minimize clock drifts that may occur at each wireless sensor over long periods without synchronization.

In addition to the wireless sensors collecting the RB-M motions and strain, a captain's log is kept by the ship crew. Sea state data is also retrieved from the National Buoy Data Center (NBDC) for a nearby buoy. The captain's log records observed wave periods, heights and ship speed; however, these are only recorded periodically and are based on human estimation of the sea parameters. The NBDC data eliminate the subjectivity and provide an exact time stamp at set intervals. Yet, these observations may not accurately represent the sea environment at the exact location of the vessel, especially considering their large time discretization. Therefore, the captain's log and NBDC are only used for qualitative reference; thus, quantitative data analyses focus solely on data collected from the installed strain gages and accelerometers.

2.2.2 Hull Monitoring System Performance

During sea trials (Monday, October 13 to Thursday, October 16, 2014), the RB-M accelerations and strains are recorded continuously at 50 or 100 Hz (depending on user configuration). The basestation operating protocol results in robust acquisition of the wireless hull monitoring system data. The wireless transmission of the data across the solid aluminum bulkheads (i.e., between the bow and the survivor cabin, and the auxiliary machinery compartment and the survivor cabin) is proven to be very robust. Figure 2.8 illustrates the packet transmission success rate through the bulkhead for all sensors during the four days of sea trials. The plot shows data collected by the basestation where a solid square marker indicates data is received and logged for a 10-minute dataset. For the first three days (October 13-15, 2014), the sampling frequency is 50 Hz; to increase this to 100 Hz for the final day (October 16, 2014), some of the channels are turned off as can be seen on the right of Figure 2.8. The data packets are successfully transmitted through the thick bulkheads 89% of the time (1363 successful out of a possible 1535). The loss of bow accelerations on the first day of testing is later discovered to be due to a loose connection

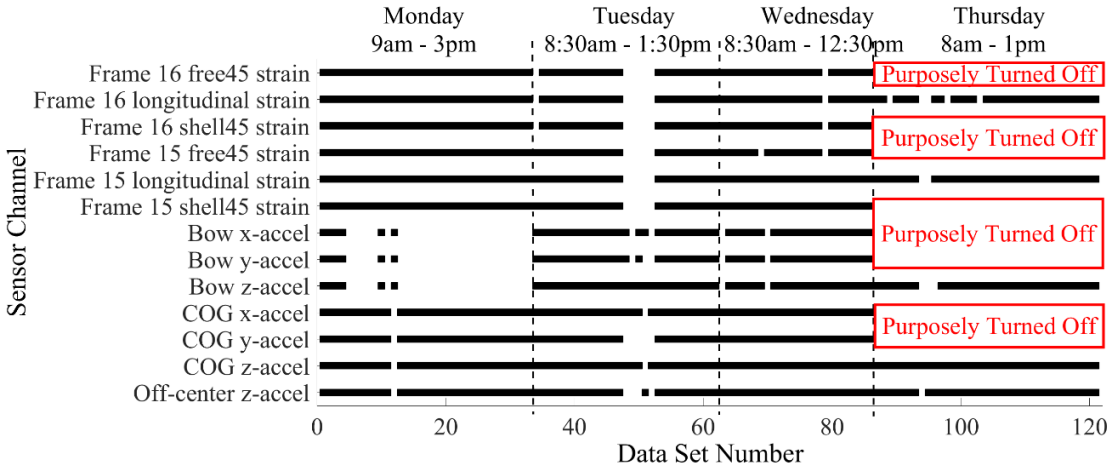

Figure 2.8 Packet transfer (data collection) successful execution (89% successful transmission).

between the tri-axial accelerometer and a *Narada* node. If this is ignored, the data transmission success rate is above 95%.

A comparison of measured accelerations at the COG for the entire first day are shown in Figure 2.9. Also shown are the wave heights logged by the ship crew. The magnitude of heave roughly correlates with wave heights. Figure 2.10 plots the *z*-acceleration (in the heave direction) for all three accelerometers for 30 seconds. The difference in magnitudes between the auxiliary and bow data is an indication of vessel pitch, while the difference between the COG and OC accelerations is an indication of vessel roll. Figure 2.11 plots the *x*-, *y*- and *z*-axes of acceleration in the bow. The *z*-direction has the largest magnitude; however, the *x*- and *y*-accelerations are still present and are a function of the vessel's heading. Figure 2.12 plots longitudinal strain data from both ends of the bow stiffener element (at frame 15 and frame 16) with clearly identifiable wave events over the 30 seconds shown. Figure 2.13 plots the *z*-axis acceleration at the vessel

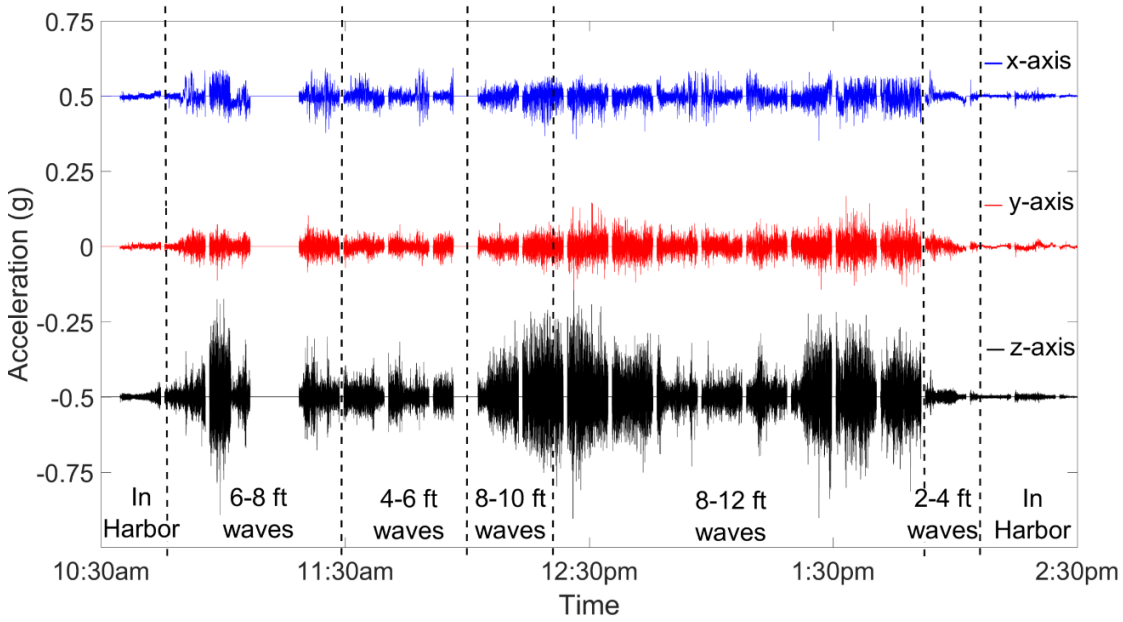

Figure 2.9 Auxiliary (COG) accelerations and sea wave heights on Monday, October 13, 2014 (time is local time).

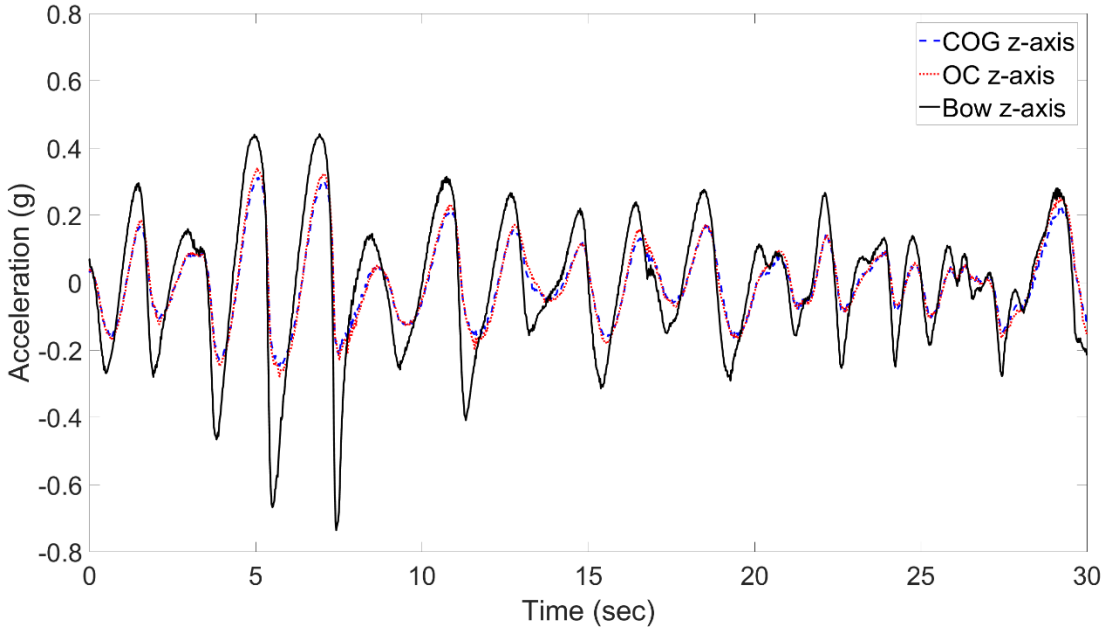

Figure 2.10 Acceleration time-series in the *z*-axis for all three accelerometers (09:41 PST, Tuesday, October 14, 2014): center of gravity (COG), off-center (OC) and bow.

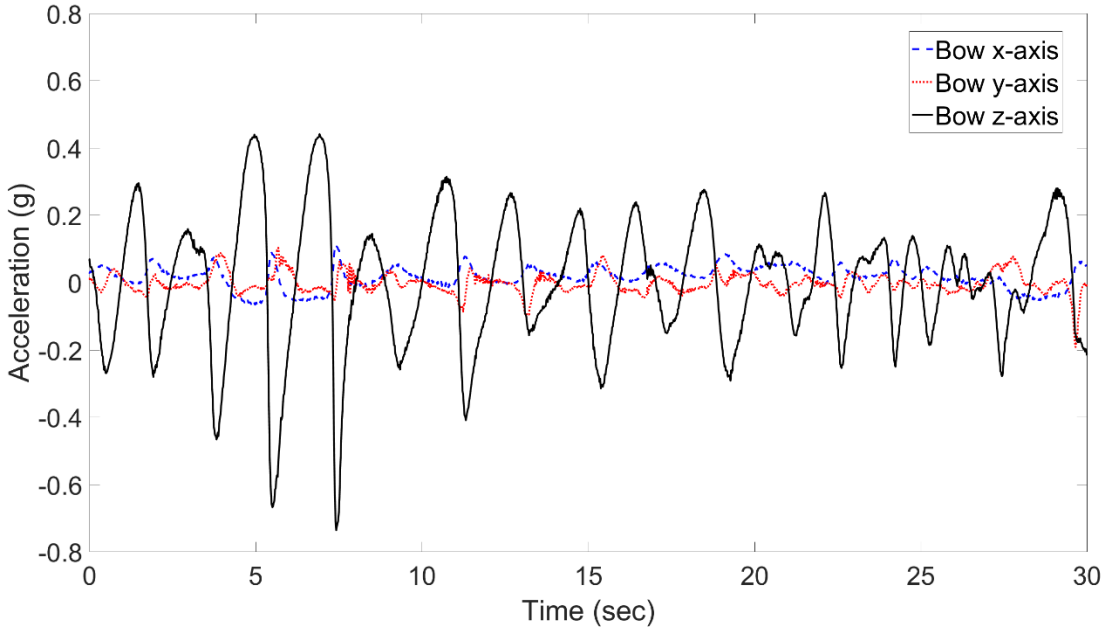

Figure 2.11 Acceleration time-series in the *x*-, *y*- and *z*-axis for the bow accelerometer (09:41 PST Tuesday, October 14, 2014).

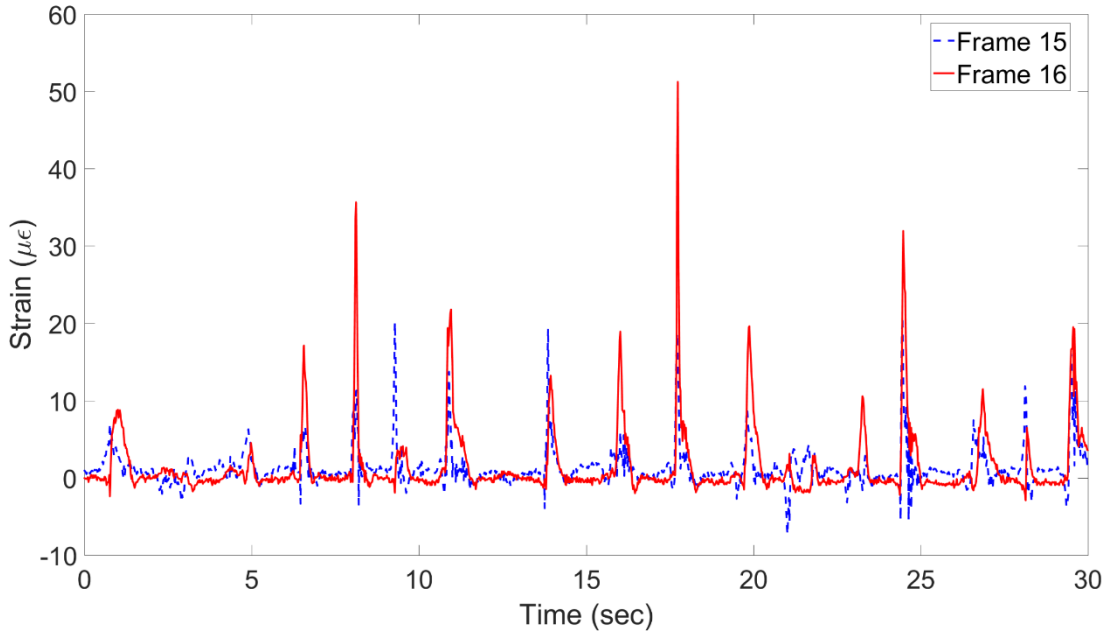

Figure 2.12 Strain time-series at both ends of hull stiffener near frame 15 and frame 16, respectively (12:32 PST, Monday, October 13, 2014).

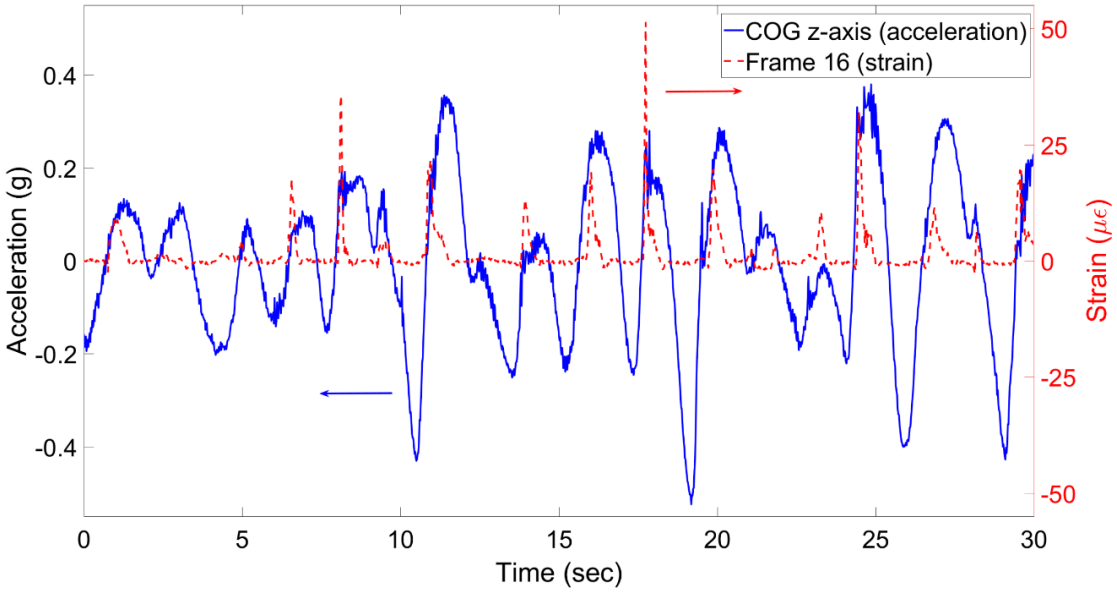

Figure 2.13 Time-series of *z*-axis acceleration at the COG and strain at the stiffener near frame 16 (12:32 PST, Monday, October 13, 2014).

COG and the strain on the side of the stiffener near frame 16 (closest to the end of the bow) for the same observation period (12:32 PST, Monday, October 13, 2014). The crew specifies this observation period as having wave heights of 8 to 12 feet (2.4 to 3.7 m). The peak strains occur when the ship is at maximum downward acceleration (recall, positive heave, *z*, is in downward direction) which occurs when the ship is rising up to the wave crest; the physics of this is explained by Lind, Stansby, Rogers & Lloyd (2015). For slamming, or more extreme peaks, the acceleration exhibits a saw tooth, or ringing, response as a flexible body structural mode is excited from the slamming impulse. Examples of this can be seen at time stamps of approximately 8, 17 and 25 seconds in Figure 2.13. Clearly, slamming events on the hull bow represent a significantly larger strain response in the hull, as would be expected.

2.3 Automated Data Processing Architecture

Response amplitude operators (RAOs) are an analytical tool used in reliability-based design of ship hulls. The RAO function, *R*, takes as input the frequency and angle at which waves impact a hull to determine an operator that is multiplied by the wave height to determine the ship response, *X*, such as its displacements and rotations:

$$X(A, \phi) = H \cdot R(f_e, \mu), \tag{2.1}$$

where, A and ϕ are the amplitude and phase of the ship response, respectively, H is the wave height, f_e is the wave encounter frequency and μ is the ship heading with respect to the waves. Note, Equation 2.1 makes they assumption that the response, *X*, scales linearly with wave height, *H*. Ship motions are then used to determine design forces for members and to model fatigue. These are typically determined using scaled models in towing tanks

or CFD numerical models. In this study, an alternative approach is taken where the RAO functions are empirically derived from sea trials during a short-term hull monitoring campaign to predict root mean square (RMS) accelerations, hull strains, and consumed fatigue life of critical high stress hull components.

The analytical framework proposed herein consists of three major modules. In the first, the ship motions are used to derive the sea state as EOC parameters. Specifically, the accelerations measured at the COG, OC from the COG, and in the bow, are used to derive the encounter frequency, wave height, and ship heading individually. The second module utilizes a regression approach to best fit a nonlinear mapping between sea state and the measured RMS acceleration, *i.e.*, empirical RAO functions (Equation 2.1). The third model then develops the empirical CFO functions that map RMS acceleration to strain levels and corresponding consumed fatigue life for future hull life-cycle assessments.

2.3.1 Determination of Sea Condition from On-Board Measurements

Methods are derived to determine sea state (f_e, H, and μ) using the available inertial measurements from the RB-M. Once derived, these methods are validated using a model of the RB-M created using MATLAB (TMI, 2013) to simulate the hull motion in a variety of sea states. In addition, the ship motion software POWERSEA (SMA, 1999) is used to model the RB-M motions in head seas (*i.e.*, with zero heading). The key purpose of using POWERSEA is to include the hydrodynamic interaction between the vessel hull and the waves it is encountering. However, POWERSEA is unable to simulate ship motions in non-zero heading conditions necessitating a MATLAB model where heading can be varied. The lack of efficient, off-head-seas numerical formulations is another reason cost-effective full-scale monitoring systems can greatly improve the current practice.

2.3.1.1 Derivation of Sea State from Hull Accelerations

The inertial measurements of the ship collected from the RB-M accelerometers are used to estimate the sea state (f_e, H, and μ). To accurately calculate the sea state, the measured acceleration data is broken down into individual wave events. This is necessary because simply aggregating or averaging data over a long period negates the significance of the instantaneous interactions between various components of the data in addition to accumulating integration errors over long integration periods. Each wave event is defined as one wave encounter period, T, and can easily be distinguished, as shown in Figures 2.10, 2.11 and 2.13, by searching for positive zero-mean crossings in the heave (z) acceleration data. That is, each wave event is defined as the data between consecutive points at which the acceleration crosses from negative to positive. The encounter frequency by definition is the inverse of the wave encounter period. The wave height is determined by twice integrating the heave (z) acceleration measured at the COG with respect to time and dividing the difference of the maximum (peak) and minimum (trough) by a hydrodynamic correcting factor, k, derived from POWERSEA as will be described:

$$H = \frac{\max\left(\iint_0^T \ddot{z}_{COG} dt\right) - \min\left(\iint_0^T \ddot{z}_{COG} dt\right)}{k}. \tag{2.2}$$

Note, special heed must be taken when numerically integrating the acceleration data that the resulting velocity data is shifted using an integration constant such that the velocity is zero at the same time stamps as the maximum and minimum accelerations, respectively. Otherwise, the second integration to displacement is inaccurate. The hydrodynamic correcting factor, k, is intended to correct the wave height estimate by accounting for the hull COG rising more, or less, with respect to the water level depending on the wave encounter frequency. The factor is defined as the ratio of the vessel COG displacement,

z_{COG}, over a wave period *(i.e.*, effective wave height) relative to the actual water surface, z_{wave}, wave height:

$$k = \frac{\max_{t\epsilon[0,T]} z_{COG} - \min_{t\epsilon[0,T]} z_{COG}}{\max_{t\epsilon[0,T]} z_{wave} - \min_{t\epsilon[0,T]} z_{wave}}. \tag{2.3}$$

The hydrodynamic correcting factor is obtained using POWERSEA, a numerical simulation environment for predicting the motions of planning boats in various sea conditions. A model of the RB-M hull is created in POWERSEA and is shown in Figure 2.4. The input parameters to POWERSEA for definition of the sea conditions includes ocean depth, wave period, wave height and vessel speed (in either heading or following seas). From these simulations, the encounter frequency, heave position and wave position are extracted for various sea states and used in Equation 2.3 to determine *k*, which is plotted in Figure 2.14.

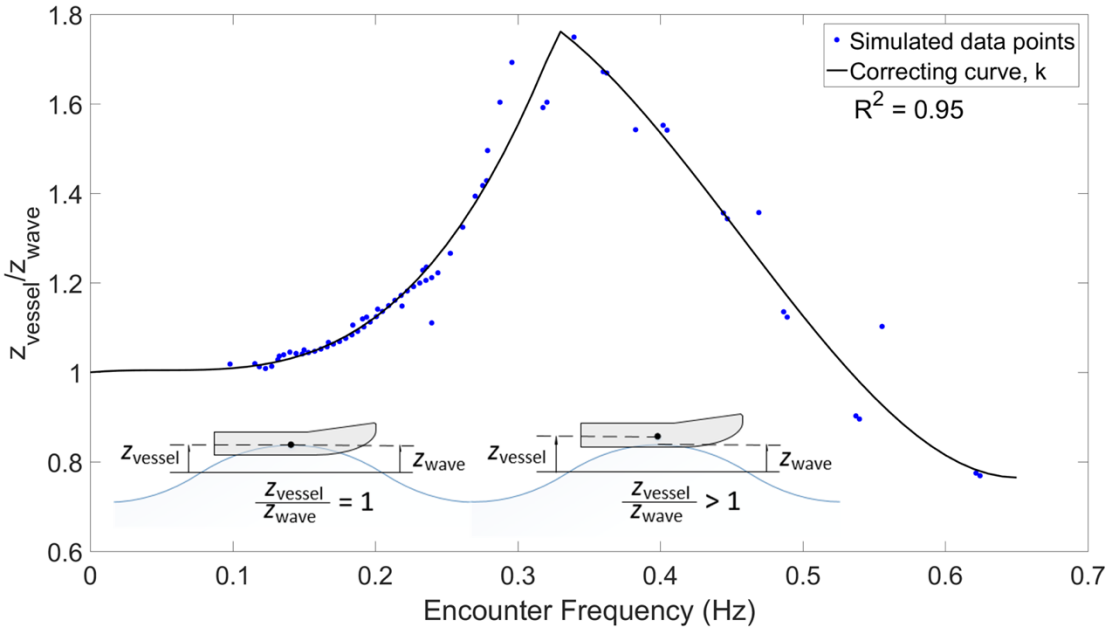

Figure 2.14 POWERSEA simulation results of encounter frequency versus vessel position normalized to sea position as illustrated in the two inset illustrations.

The vessel heading, μ, relative to a wave field affects the ship pitch, Θ, and roll, Φ, behavior. Davis et al. (2005) previously proposed performing an instantaneous calculation (at every time instance) for heading, μ, using:

$$\tan(\mu) = \frac{\tan(\Phi)}{\tan(-\Theta)}, \tag{2.4}$$

based on measurement of pitch and roll at the COG. Recall, the RB-M is not instrumented with a gyroscope; therefore, a means of using acceleration readings to determine pitch and roll is necessary. While multiple methods are available to estimate pitch and roll from accelerometer signals, a method based on the COG accelerometer is considered (Pedley 2013). The method will assume the vessel surge acceleration is zero which is reasonable over a single wave period. The pitch and roll at any given time can be determined as:

$$\tan(\Theta) = \frac{-\ddot{x}_{COG}}{\ddot{z}_{COG}}, \tag{2.5}$$

$$\tan(\Phi) = \frac{\ddot{y}_{COG}}{\ddot{z}_{COG}}. \tag{2.6}$$

Because the heading is comparing the pitch and roll relative to each other, the following equation can be used to derive ship heading:

$$\tan(\mu) = \frac{\ddot{y}_{COG}}{\ddot{x}_{COG}}. \tag{2.7}$$

Similar to the estimation of wave height, H, the vessel heading is determined for a single wave event. To enhance the robustness of the heading estimate when noise is present in the accelerometer signal, Equation 2.7 is modified to consider the peak-to-peak change in accelerations over the wave period, T:

$$\tan(\mu) = \frac{\max\limits_{t\epsilon[0,T]} \ddot{y}_{COG} - \min\limits_{t\epsilon[0,T]} \ddot{y}_{COG}}{\max\limits_{t\epsilon[0,T]} \ddot{x}_{COG} - \min\limits_{t\epsilon[0,T]} \ddot{x}_{COG}}. \tag{2.8}$$

To determine if the heading is positive or negative (*i.e.*, starboard or portside, respectively), the relative phase between the *x*- and *y*-accelerations is considered. When they are in-phase, the heading is positive; when out-of-phase, the heading is negative.

2.3.1.2 Validation Model

To validate the proposed inversion method of extracting sea state from ship inertial measurements, a rigid body ship with dimensions identical to the RB-M is created in MATLAB and exposed to varying sea conditions including variations in wave height, wave length, wave period, vessel speed and vessel heading. The wave height, wave period and vessel speed variables are selected to be in the ranges logged by both the captain and NBDC during sea trials with the RB-M. All possible heading scenarios are explored. The wave length is determined by setting the general wave equation and the sea wave speed equation (Young 1999), shown respectively, equal to each other and solving iteratively:

$$v_{wave} = \frac{\lambda}{T}, \tag{2.9}$$

$$v_{wave} = \sqrt{\frac{g\lambda}{2\pi}\tanh\left(\frac{2\pi d}{\lambda}\right)}, \tag{2.10}$$

where λ is the wave length, v_{wave} is the wave speed, g is gravity and d is the sea depth with a range of 36 – 120 feet (11 to 37 m) as determined with GIS data (ArcGIS 2016). This results in wave lengths between 200 and 320 feet (61 – 98 m), which is consistent with typical ocean wave lengths (Garrison & Ellis, 2014). The model outputs are the accelerations at the three locations where accelerometers are located on the full-scale RB-M. The vessel is assumed to only have rigid body motions because preliminary data analyses from sea trials show that wave motions are dominant in the measured ship accelerations. Figures 2.10, 2.11 and 2.13 support this observation with ship accelerations

dominated by wave motion with encounter periods near 1.7 sec. The model describes the rigid body RB-M with six degrees-of-freedom (*i.e.*, heave, surge, sway, pitch, roll, and yaw) with the accelerations at the actual measurement locations determined assuming the accelerometers are fixed to a rigid plane representing the hull.

Waves at sea often follow a trochoidal wave form; however, they are generally modelled as sinusoidal waves (SMA, 1999). A single sine wave is used (instead of a summation of sine waves) because the dominant wave field during these trials is wind driven, long-period swells. Thus, the elementary equation for heave position, *z*, at the COG is:

$$z_{COG} = \frac{H}{2} cos(\omega_e t) = \frac{H}{2} \cos(2\pi f_e t). \tag{2.11}$$

The effective or encounter frequency, f_e, is influenced by the wave speed, v_{wave}, vessel speed, v_{vessel}, and vessel heading as follows:

$$f_{vessel} = \frac{v_{vessel}}{\lambda} \cos(\mu), \tag{2.12}$$

$$f_{wave} = \frac{v_{wave}}{\lambda}, \tag{2.13}$$

$$f_e = f_{wave} \pm f_{vessel}, \tag{2.14}$$

where f_{wave} is the wave frequency and f_{vessel} is the vessel frequency assuming the wave is a standing wave. The two frequencies in Equation 2.14 are added or subtracted depending on whether the vessel is heading or following seas. In addition, the heave position of the RB-M is adjusted in the model to include hydrodynamic effects using the correcting factor, *k*, determined by POWERSEA:

$$z_{COG} = \frac{kH}{2} \cos\left(2\pi \left(\frac{v_{wave} \pm v_{vessel} \cos(\mu)}{\lambda}\right) t\right). \tag{2.15}$$

The surge and sway of the ship are also modelled. The sway is zero under the assumption that the ship is on a straight heading (*i.e.*, not turning). The surge position is defined as:

$$x_{COG} = v_{vessel}t. \tag{2.16}$$

During the simulation, the hull is modelled as a rigid plane and is assumed to be parallel to the wave surface. This is justified because the ship length (45 feet) is much shorter than the wave length (~300 feet). Under this assumption, first the gradient of the wave surface, τ, is calculated at the COG then the hull pitch, Θ, and roll, Φ, components are determined as:

$$\Theta = \tan^{-1}(\tau\cos(\mu)), \tag{2.17}$$

$$\Phi = \tan^{-1}(\tau\sin(-\mu)). \tag{2.18}$$

As can be seen, pitch and roll are dependent on the heading which is intuitive. If the ship is in heading seas ($\mu = 0°$) then the hull only has pitch while if the ship is in beam seas ($\mu = 90°$) then the hull only has a roll component. Due to the assumption of the ship remaining on a constant heading (i.e., not turning), the yaw is simply zero ($\Psi = 0$).

Simulation of the RB-M acceleration readings are generated using the model and the known geometry of the hull. Here, the longitudinal distance between the bow and COG accelerometers, L_{bow}, is 16.3 ft (5.0 m) and the transverse distance between the off-center (OC) and COG accelerometers, L_{OC}, is 3.0 ft (0.91 m). The simulated OC and bow coordinates of the ship are:

$$x_{OC} = x_{COG}, \tag{2.19}$$

$$y_{OC} = y_{COG} + L_{OC}\cos\Phi, \tag{2.20}$$

$$z_{OC} = z_{COG} + L_{OC}\sin\Phi, \tag{2.21}$$

$$x_{bow} = x_{COG} + L_{bow}\cos\Theta, \tag{2.22}$$

$$y_{bow} = y_{COG}, \tag{2.23}$$

$$z_{bow} = z_{COG} + L_{bow}\sin\Theta. \tag{2.24}$$

The translational accelerations for all three axes of each sensor are calculated by taking the derivative with respect to time twice (accelerations are reported in units of *g*). Additionally, the acceleration due to gravity that changes with the rotation of the vessel is calculated and added to the simulated accelerometer outputs. For example, with the vessel at rest the *x*- and *y*-accelerations are 0, while *z*-acceleration is equal to gravity (1 *g*). As the vessel is modelled as a rigid body, the accelerations due to gravity ($\ddot{x}_g, \ddot{y}_g, \ddot{z}_g$) are the same for all three sensor locations and are determined as follows:

$$\ddot{x}_g = \sin(-\Theta), \tag{2.25}$$

$$\ddot{y}_g = \sin(\Phi), \tag{2.26}$$

$$\ddot{z}_g = \sqrt{1 - \ddot{x}_g{}^2 - \ddot{y}_g{}^2} - 1. \tag{2.27}$$

The value of 1 is subtracted from $\ddot{z}_g$ to be consistent with the real, on-board sensors, which are zero mean adjusted when the vessel is at rest at the dock before sea trials. The accelerations due to gravity are added to all three sensors ship motion accelerations to calculate the final acceleration output for the simulated accelerometer readings.

An extensive set of simulations are made of the RB-M using the MATLAB model to provide simulated data from which the proposed sea state estimation algorithm can be validated. A wide variety of ship headings, wave heights and encounter frequencies are simulated sweeping through values observed during sea trials with simulated accelerometer readings logged at a 50 Hz sampling rate. A small amount of white noise (based on noise floor variance of the actual accelerometers) is added to the simulated sensor readings to

enhance their realism. This data is low-pass filtered in the same manner as the on-board data then sea conditions are calculated using only the acceleration data. The simulated accelerometer data is divided into individual wave events with the proposed sea state extraction algorithm applied to each wave event. Only after the sea state for each wave event is calculated, the final numbers (*i.e.*, encounter frequency, wave height and heading) are averaged for each 10-minute segments. A sample comparison of input sea conditions and calculated conditions is shown in Table 2.1 and demonstrates the accuracy of the approach to calculating sea conditions. Once validated, the algorithm is applied to the sea trial data from the full-scale RB-M.

2.3.2 Hull Response Analysis

The RB-M hull response can be divided into two parts: the rigid body ship movements and the flexible body stresses these movements impose on various hull components. The rigid body motions are important in design to determine the loads imposed on various components of the ship while the latter response is of critical importance to the life-cycle analysis of the vessel performance and health.

2.3.2.1 Relate measured sea conditions to acceleration response

A peak expected acceleration allows designing for the maximum expected force on the hull. However, due to the stochastic nature of a sea wave field it is prudent to relate sea conditions to accelerations averaged over set time periods. Therefore, the root mean square (RMS) of hull acceleration is calculated for the same 10-minute time segments; corresponding averaged sea conditions are calculated for the same duration. After determining the sea conditions and the vessel's response, RAOs, calculated using full-scale

Table 2.1 Simulated sea conditions compared to sea conditions calculated using accelerometer readings with noise and sampling error introduced.

	Wave Height (ft)	Heading (˚)	Encounter Frequency (Hz)
Simulation Input	6	-75	0.141
Calculation	5.94	-73.9	0.141
Simulation Input	6	-45	0.170
Calculation	5.93	-44.8	0.170
Simulation Input	6	-15	0.186
Calculation	5.75	-15.5	0.186
Simulation Input	10	15	0.186
Calculation	9.52	15.4	0.185
Simulation Input	10	45	0.170
Calculation	9.48	44.8	0.170
Simulation Input	10	75	0.141
Calculation	9.92	74.8	0.142

data, are determined. Referencing Equation 2.1, moving wave height to the left side of the equation and having acceleration as the response output, the following equation is used to solve for the vessel RAOs:

$$\frac{X(\ddot{z})}{H} = R(f_e, \mu). \tag{2.28}$$

More specifically, the quotient of *z*-acceleration RMS and height for each 10-minute segment is taken as the dependent variable in a regression model with encounter frequency and heading as the independent variables/predictors. Unlike traditional RAOs that consider hull responses from zero to infinite frequencies, this RAO model only considers the range of frequencies observed in sea trials (*i.e.*, 0.2 to 0.85 Hz, not 0 to ∞ Hz). The model optimizes for the coefficients, α_1, α_2, α_3, β_1, β_2 and β_3, of the third order predictor terms of the equation:

$$\frac{\ddot{z}}{H} = \alpha_1 f_e + \alpha_2 f_e^2 + \alpha_3 f_e^3 + \beta_1 \mu + \beta_2 \mu^2 + \beta_3 \mu^3 + B_Z, \tag{2.29}$$

where B_Z is the $\ddot{z}$ intercept. Using Equation 2.29, relationships between sea conditions and ship accelerations at both the COG and bow are found as shown in Figure 2.15. Each data point represents the RMS acceleration and mean sea conditions during a 10-minute segment of data. The high R^2 values of 0.82 and 0.86, respectively, validate the ability of rapid-to-deploy full-scale measurement systems to accurately determine vessel RAOs.

In practice, entities such as the USCG could use empirical RAOs to more accurately and cost efficiently design and plan for accelerations/forces experienced by the vessel as well as its crew members. For example, a short-term deployment of the proposed system would allow for a vessel specific RAO containing a sufficient set of sea conditions to be determined (*e.g.*, for a large range of encounter frequencies). Then, probabilistic maritime and weather data could be used to determine the number of hours a vessel would operate in given sea conditions. Next, these conditions could be used as input to the empirical RAO. Finally, a design and operational strategy determined based on vessel specific characteristics that could be obtained at quicker rates and lower cost.

2.3.2.2 Relate measured accelerations to consumed fatigue

On-board measurements allow the above approach to be taken one step further and measure not only acceleration responses but also component level damage at critical locations. The USGC had previously conducted analyses on the 45' RB-M that informed this study's decision to install the strain gages on the bow stiffener experiencing the highest stress levels in the vessel. To gain meaningful insight from the data and begin assessing the fatigue life of the ship, the fatigue consumed by the stiffener near each frame is calculated.

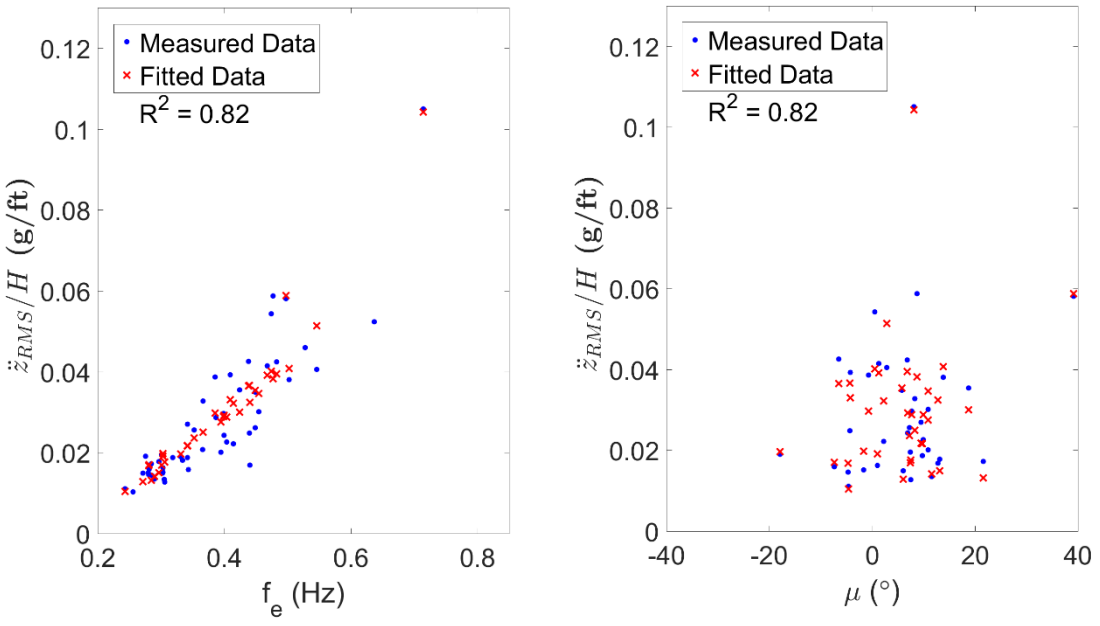

(a)

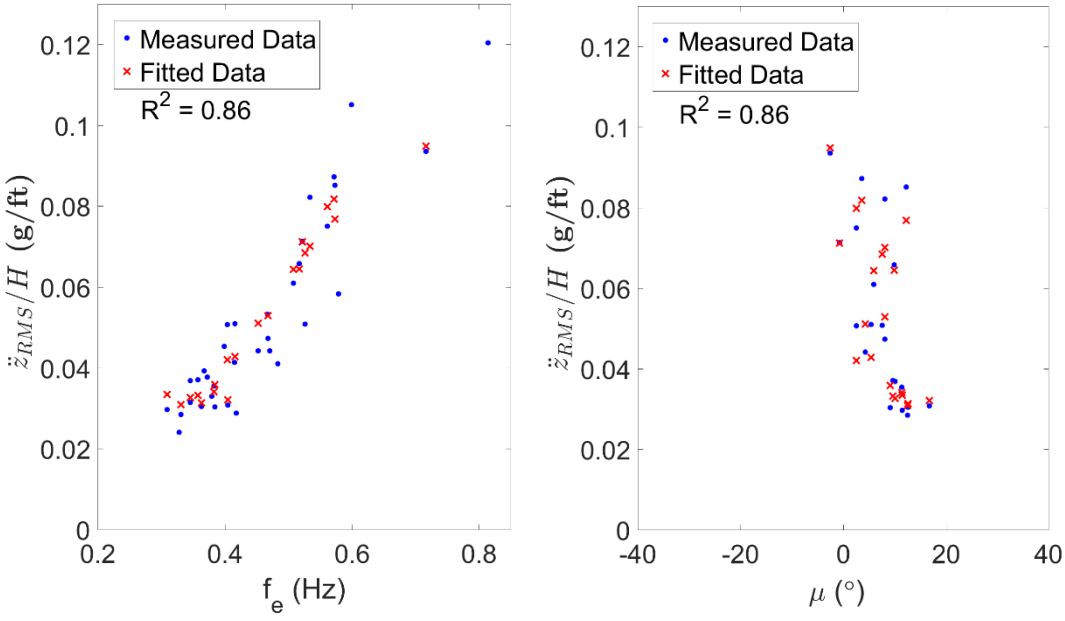

(b)

Figure 2.15 Response amplitude operators (RAOs) relating ship heave acceleration response versus sea state: (a) COG; (b) bow. Note, the regression model takes as input H, f_e and μ; all of the plots are normalized to H; the plots on the left are projected on f_e and the plots on the right are projected on μ.

The consumed fatigue life is calculated using Miner's Rule (Miner, 1945):

$$C = \sum_{i=1}^{k} \frac{n_i}{N_i}, \tag{2.30}$$

where, C is the fraction of the consumed fatigue, n_i is the number of cycles accumulated at stress S_i, and N_i is the number of cycles a specimen can withstand at the given stress range (S_i). Therefore, consumed fatigue is calculated for every stress state and summed together. S_i and N_i are determined using equations for *S-N* curves for aluminum specimens published by the Naval Surface Warfare Center Carderock Division (Kihl, Adler & Devine, 2014). However, the stress cycles experienced by the stiffeners during the field test at NMLBS are much lower than those calculated by the Carderock study so the Carderock *S-N* curves are extrapolated to the low stress regime experienced during sea trials. The cycle count, n_i, is calculated using a rainflow counting algorithm applied to the strain sensor data for the stiffener in the bow. This is then converted to stress using Hooke's Law ($\sigma=E\epsilon$), with E = 10,200 ksi (70 GPa). The stress cycle rainflow counts are shown in Figure 2.16. The consumed fatigue life for each 10-minute segment is calculated and used to estimate the life-cycle of the two frames instrumented. The consumed fatigue near frame 15 and 16 are calculated to be at 0.4 x 10^{-4} % and 1.1 x 10^{-4} % of their total fatigue lives, respectively. Fatigue being consumed at this low rate during the week of field measurements results in an expected service life of well beyond the 20 years that the vessel was designed for (Shepard & Curtis 2010). However, during the field test, the wave lengths are very long relative to vessel length and very rarely do the waves exceed 8 feet (2.4 m), this is confirmed by both the buoy data and the on-board calculations using ship motions. Recall, the typical operational profile is for up to 8 feet; therefore, it should be expected that in

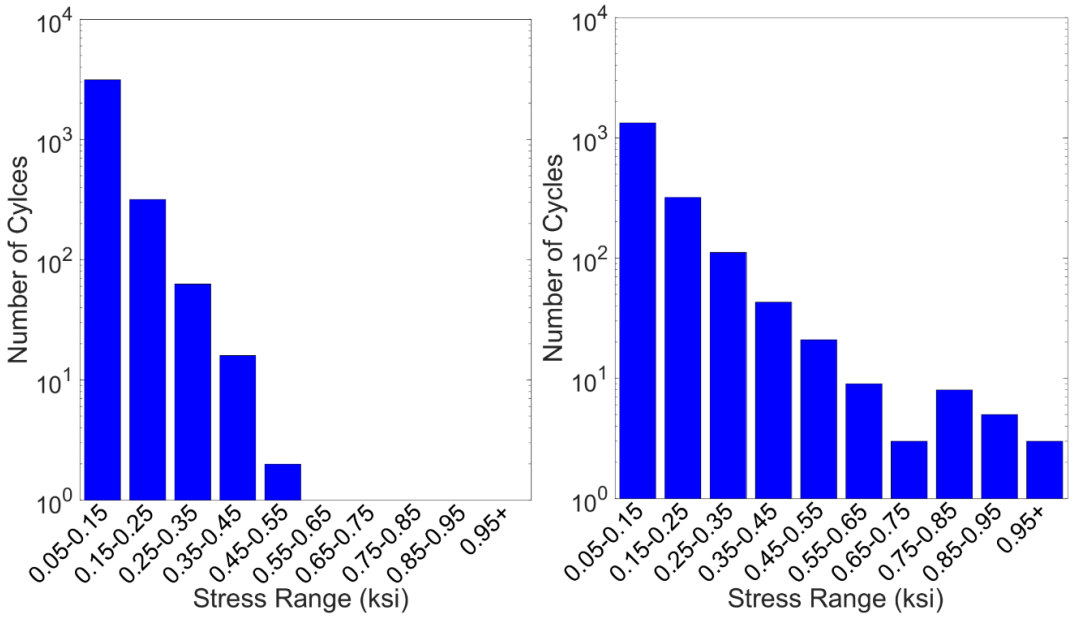

(a) (b)

Figure 2.16 Rainflow histograms of stress for location on stiffener near: (a) frame 15; (b) frame 16.

seas of less than 8 feet that fatigue life should not be an issue. Nevertheless, this set of full-scale measurements stand as a proof-of-concept that such an approach can be used to more accurately and cost efficiently characterize the 45' RB-M in high seas or with an increased operating profile, where there would indeed exist increased susceptibility to fatigue damage. Even so, the lower levels of consumed fatigue in this study provide a quantifiable measure of the cumulative effect of stress on the hull. This in turn allows for a straightforward means of relating ship motions to fatigue life.

In examining the strain response of the vessel, the effects of slamming are significant; this underscores the need to include them in life-cycle analyses. The rate of change of stress ($d\sigma/dt$) was used to clearly identify slams (Thomas et al. 2003). The distribution of slamming events versus non-slamming events is shown in Figure 2.17 for strain near frames 15 and 16. Although there is a low percentage of slamming events

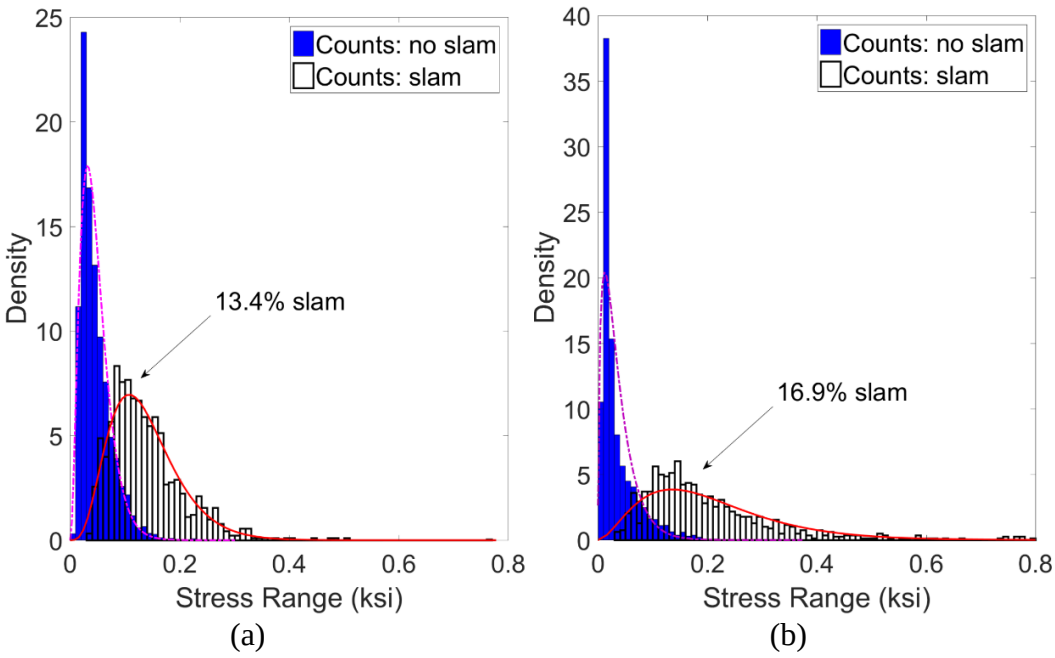

Figure 2.17 Power density function (PDF) of stress ranges for no slamming vs. slamming events: (a) frame 15; (b) frame 16.

(13.4% and 16.9%, respectively), these slamming events account for 54.2% and 90.7% of the consumed fatigue for frame 15 and 16, respectively. The stiffener end near frame 16 experiences the larger rate of slamming with the slam response contributing significantly to consumed fatigue. This faster accumulation of fatigue damage at frame 16 is due to this being the location where the hull enters and impacts waves, both in terms of its distance from the front of the boat and below the chine. The result highlights the very local nature of fatigue damage in ship hulls. In future deployments, it would be useful in characterizing the vessel to include strain gages near frame 17 and on a stiffener above and below the current installation to precisely localize critical stiffeners and connections in the hull.

Similar to the empirical RAOs found previously for hull accelerations, relationships between hull RMS accelerations and consumed fatigue for each 10-minute segment are found to complete the following equation for the consumed fatigue operator (CFO):

$$C = CFO(\ddot{x}, \ddot{y}, \ddot{z}). \tag{2.31}$$

The CFO is solved using the following model with γ_1, γ_2, γ_3, ζ_1, ζ_2, ζ_3, η_1, η_2 and η_3 as coefficients to the input predictors and B_C as the consumed fatigue, C, intercept:

$$\mathrm{C} = \gamma_1\ddot{x} + \gamma_2\ddot{x}^2 + \gamma_3\ddot{x}^3 + \zeta_1\ddot{y} + \zeta_2\ddot{y}^2 + \zeta_3\ddot{y}^3 + \eta_1\ddot{z} + \eta_2\ddot{z}^2 + \eta_3\ddot{z}^3 + B_C. \tag{2.32}$$

This is done to determine four unique relationships: COG RMS *z*-acceleration to frame 15 consumed fatigue, COG RMS *z*-acceleration to frame 16 consumed fatigue, bow RMS *z*-acceleration to frame 15 consumed fatigue and bow RMS *z*-acceleration to frame 16 consumed fatigue. These relationships are displayed in Figure 2.18. The respective R^2 values are 0.78, 0.77, 0.43 and 0.67. The lower value of 0.43 for the CFO relating bow RMS *z*-acceleration and consumed fatigue near frame 15 is likely due to two factors: first, the bow accelerometer is the one sensor with data collection difficulties on Monday (see Figure 2.8) so there is a limited amount of data. Second, the consumed fatigue near frame 15 is much lower. These two conditions occurring simultaneously results in a lower correlation. More sea trials, especially in higher sea states, would likely improve the CFO RMS *z*-acceleration for bow versus frame 15. Withstanding the lower R^2 for this CFO, the other three CFOs have high correlation and validate the use of the proposed full-scale measurement approach to performing life-cycle analyses.

An improved life-cycle analysis approach could be implemented by empirically determining RAO and CFO functions, as proposed herein, to a specific vessel by means of short-term full-scale monitoring deployments. These operators could be very accurate, as proven by the high correlation for the RAOs and CFOs determined using this approach, and include all forms of stress loading (such as slamming). They would also eliminate the

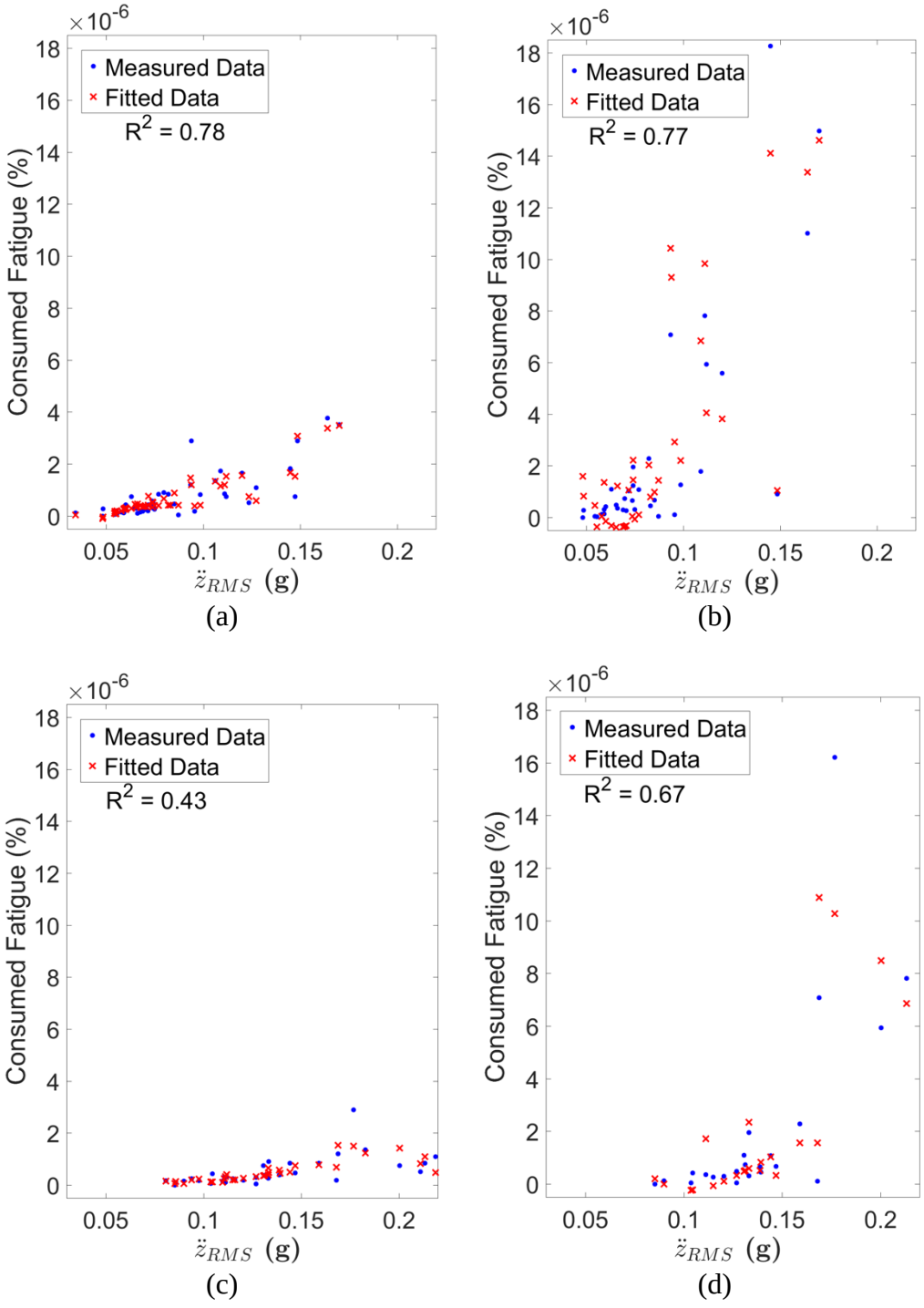

Figure 2.18 Consumed fatigue operators (CFOs) of ship heave accelerations versus consumed fatigue (stress): (a) COG versus frame 15; (b) COG versus frame 16; (c) bow versus frame 15; (d) bow versus frame 16. Note, the regression takes *x*-, *y*- and *z*-acceleration as input but is projected across *z*-acceleration on the abscissas in this plot.

reliance on often costly and uncertain modelling approaches. The sea condition operational profile, or EOC, could be input to the CFO and component specific stress and corresponding consumed fatigue behavior predicted and used as a powerful tool to accurately manage the life-cycle of a vessel.

2.4 Chapter Summary

The study presented in this chapter aims to develop a rapid-to-deploy hull monitoring system with an associated analytical framework that uses hull measurements to assess the performance of a vessel over its full life-cycle. The system is realized by means of a wireless hull monitoring strategy. The analytical objective is met with the development of a framework to determine sea conditions, or environmental operating conditions (EOCs), using inertial measurements, relate sea conditions to acceleration/force responses on the vessel via response amplitude operators (RAOs), and relate vessel accelerations to a measurement of damage using consumed fatigue operators (CFOs). The short-term monitoring system herein is unique in both its ability to be quickly implemented and its application to a smaller vessel. It also provides an innovative data-driven framework for the assessment of EOCs, RAOs and CFOs for use in life-cycle analyses. Vessel owners could use the method validated in this study to more accurately and cost efficiently design and plan for accelerations/forces and damage/fatigue experienced by vessels in their fleets. For example, by acquiring empirical ROA and CFO functions through a short-term monitoring framework, they can use these relationships to estimate hull behavior over a vessels future operational life cycle as defined by time periods of operation in different EOC states.

The wireless hull monitoring system is successfully installed in a matter of hours and removed in even less time leaving no trace. The monitoring system consisting of 13 measurement channels is very reliable over 4 days of continuous operation with a communication success rate of nearly 90%; this is impressive given the bulkheads the wireless signals must penetrate for data communication. The data obtained from the monitoring system is used to accurately determine sea state; the approach to do so being validated using POWERSEA and MATLAB models. The sea state is related to ship acceleration using multiple input regression models that return RAOs with high correlations. The strain measurements and the effects of slamming at two critical stiffener locations are examined and quantified using consumed fatigue calculations. The vessel accelerations are related to consumed fatigue at the respective locations using multiple input regression models that return CFOs with high correlations.

For this method to be fully implemented, a larger set of data would need to be gathered to increase the EOC profile over which observations are made. However, this study serves as a proof-of-concept that such an endeavor would yield impactful results. Future studies could be improved by either collecting data for a longer period (e.g., 2 – 4 weeks instead of 1 week) or by navigating the vessel on a defined path across somewhat pre-determined sea conditions as is done in typical sea trial studies. For example, navigating in an octagon, similar to Fu et al. (2007), that encompasses a buoy would allow for headings and wave heights to be easily determined. However, to maintain the self-sufficient system (not rely on off-board data such as buoy measurements) it would be beneficial to include a wave radar detector to increase the accuracy of calculated wave heights and headings (Thornhill& Stredulinksky 2010). Moreover, future deployments

could include additional strain gages or other fatigue monitoring techniques, such as acoustic emission (Anastasopoulos, Kourousis, Botten & Wang, 2009), to gain component specific fatigue information at more locations and to better localize fatigue behavior. These proposed augmentations to the monitoring system could be easily integrated into the current architecture used in the study for this chapter. Whether additional sensors are added, or not, the rapid-to-deploy monitoring system validated in this study can be extended to other vessels and EOCs to improve design and life-cycle approaches by providing a data-driven support system.

The USCG, USN or other entities could use the method validated in this study to more accurately and cost efficiently design and plan for accelerations/forces and damage/fatigue experienced by vessels in their fleets. This improved life-cycle analysis tool could be achieved using empirical RAO and CFO functions which could be obtained with higher fidelity, in a quicker time frame and at a lower cost than the typical wave tank, CFD, or FEM modelling approaches. For example, a short-term deployment of the proposed system would allow vessel specific RAO and component specific CFO functions to be determined that contain a sufficient set of sea conditions. Then, probabilistic maritime and weather data could be used to determine the number of hours a vessel would operate in given sea conditions. Next, these conditions used as input to the empirical RAOs and CFOs. These operators would predict stress loading and fatigue behavior to be used as a powerful decision-making tool to more accurately and efficiently execute life-cycle management strategies.

CHAPTER 3

LONG-TERM WIRELESS STRUCTURAL HEALTH MONITORING OF RAILROAD BRIDGES

Rail is an important mode of transportation that moves 40% of domestic freight tonnage in the United States (Moteff and Parfomak 2004). A key element of the rail network are bridges; in the U.S. there are more than 76,000 railroad bridges with more than half of them constructed before 1920. Railroad companies bear responsibility for ensuring bridges are safe and well maintained. However, this can be a challenging task given the age and size of many of the bridges a railroad manages. Railroads are interested in going beyond traditional visual inspections by adopting monitoring technologies to track the performance of their bridges (Otter et al. 2012). However, to justify the costs associated with monitoring, monitoring must beneficially impact the decision-making of railroads. In this chapter, a long-term wireless monitoring system is proposed for monitoring the performance of a long-span railroad bridge called the Harahan Bridge (Memphis, TN). Wireless monitoring is a cost-effective approach for monitoring critical bridge components. To reap benefits, the wireless monitoring system is proposed to drive a D2D framework that is tailored to address two railroad needs. First, the wireless monitoring system and associated data processing modules are designed to identify when the bridge is exposed to major load events including train loads, barge collision, and earthquakes. The maximum load is estimated in instrumented bridge components and alerts sent when

element responses exceed established thresholds. Second, the D2D framework seeks to design a wireless monitoring system that can alert bridge managers of overloaded structural components deemed as critical elements (or elements of chief concern). In this chapter, the monitoring strategy is focused on monitoring a critical eyebar element of the Harahan Bridge primary truss system. Specifically, the automated data processing of the D2D framework estimates the proportionality of tensile load on the individual parallel eyebar links of the eyebar element with the bridge owner alerted when one or more eyebars takes a disproportionate fraction of the tensile load. This chapter first gives a background further outlining the motivation for and objectives of the SHM system and D2D framework. The components of the monitoring system are presented, followed by data analyses contributing to the automated D2D framework. The chapter concludes with a summary of the findings from the wireless bridge monitoring system.

3.1 Background

3.1.1 Motivation

Extreme load events are a primary concern for bridges exposed to hazards. For example, bridges located in seismic regions are susceptible to ground motion which can lead to large lateral demands on bridges and residual displacements. This can be a serious issue for a number of reasons. First, seismic loads can induce damage in key structural components that can require bridge closures to assess bridge health and to implement repairs (McCulloch and Bonilla 1970). Common damage mechanisms include vertical buckling, span displacements, and collapse of bridge piers. Undetected seismic induced damage can also render the bridge as unsafe for use by trains. Another concern associated

with earthquakes are residual bridge displacements that can alter the track; track deflections pose a serious safety risk due to train derailments (Byers 1999). The man-made hazard of collisions are another concern for bridge owners. For example, short span rail bridges over roads can be exposed to truck collisions while bridges over bodies of water can be exposed to barge and ship collisions. When reported, bridges exposed to collisions can be inspected and evaluated; however, when they are not reported collisions can lead to track displacements and possible train derailment. The 1993 Big Bayou Canot bridge collapse in Alabama is a poignant example. A barge struck a CSX swing bridge over the Big Bayou Canot in heavy fog resulting in residual displacement of the track (Smothers 1993). A few hours after being struck, an Amtrak train on the line derailed due to the unknown track displacement resulting in the death of 47 passengers. Due to these types of hazard events, interest in the adoption of bridge monitoring systems has grown in the rail industry. Structural monitoring offers railroads a more robust basis for identifying issues associated with bridges in their networks (Otter et al. 2012). Specifically, railroads desire monitoring systems that can identify loads imposed on their structures with alerts offered when loads are unexpected (e.g., barge collision) and when structural responses are excessive.

Even under normal loading conditions (e.g., train loads), there is further interest in the adoption of structural health monitoring to determine the live load response of rail bridges. Rail bridges, unlike their counterparts in highways, have an extremely high live load-dead load ratio. Understanding bridge responses under train loads is critical to understand the capacity of bridge structures in addition to managing common bridge deterioration mechanisms. For example, repeated cycles of high live loads from train axles makes fatigue a major management concern for steel bridges (Imam et al. 2006). The high

live load-dead load ratio of rail bridges also leaves critical elements (such as eyebars similar to those that failed on the San Francisco – Oakland Bay highway bridge (Gostautas and Tamutus 2015; Reid 2010)) under an even greater risk of fatigue accumulation. With fatigue being a local damage mechanism, local sensing methods are needed to track fatigue accumulation (Leander et al. 2010). Low-cost sensing methods such as wireless sensors can be used to monitor the strain response of fatigue critical bridge components to track the accumulation of fatigue damage. Railroads would ideally wish to be made aware of accelerated fatigue accumulation as it can be a cause for concern.

3.1.2 Data-to-decision Framework

In response to these needs, this chapter explores a comprehensive wireless monitoring system architecture designed to facilitate decision-making by railroads managing rail bridge assets. The monitoring system is designed as a permanent monitoring system to acquire both the global acceleration response and the local strain and acceleration responses of critical bridge components on the Harahan Bridge (which is owned by Union Pacific Railroad). The wireless monitoring system in this study is designed to specifically accomplish two goals: alert the bridge owner of extreme load events including seismic ground motion and lateral vehicle collisions, and to track fatigue accumulation in critical tensile truss bridge elements. The monitoring system is intended to be a permanent fixture on the bridge collecting data based on trigger events such as train loads and lateral motions. The monitoring system is interfaced to the Internet where data is pushed to an SQL data server for storage and data processing. An alert system is designed to alert bridge owners of extreme load events and excessive response of critical bridge components. In addition to notifying the bridge owner of potential safety issues, continuous monitoring of the bridge

response combined with traditional (visual) inspections will also assist in improving bridge maintenance strategies.

The functionality of the D2D framework is laid out in Figure 3.1. When a train crossing or other loading event (*i.e.*, barge collision, earthquake) triggers the system, the basestation sends a command for every sensor to wake up from a low-power mode and begin collecting data. After data collection at each wireless sensor node, data is transferred wirelessly to the basestation (there is a second basestation for redundancy which will be discussed in the instrumentation section). The data now stored in the basestation is transferred on a scheduled basis via the Internet to a dedicated data server at the University of Michigan. This server then automatically performs the following tasks: 1) stores the data in an organized database; 2) processes the data (*e.g.*, fatigue analyses, load distribution); and 3) sends email alerts to interested parties (*i.e.*, Union Pacific field

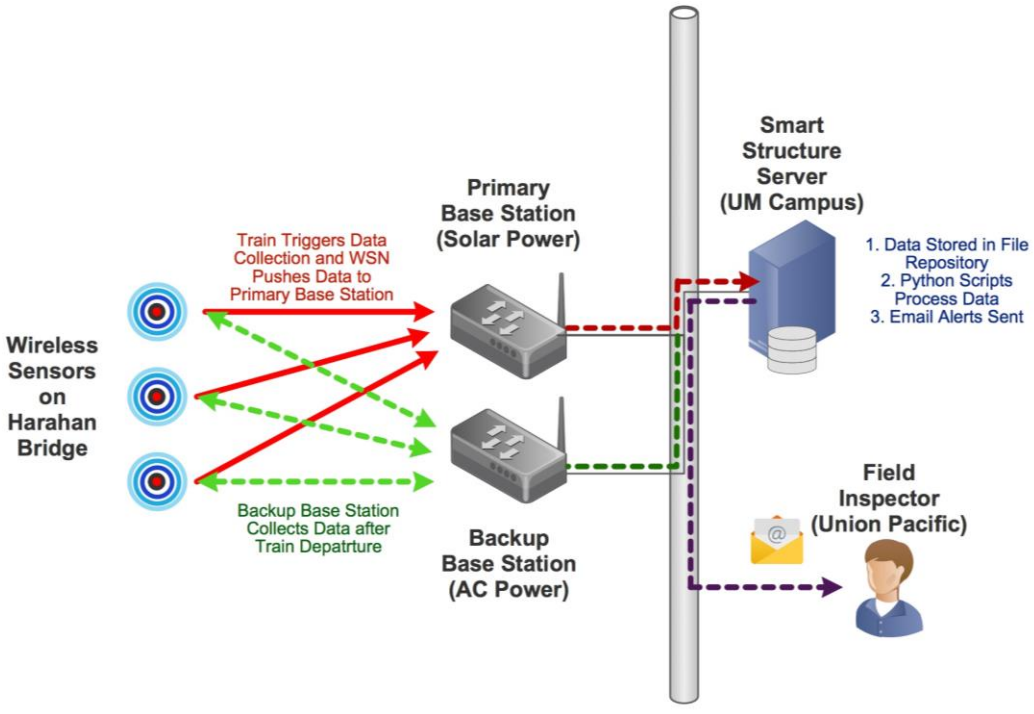

Figure 3.1 Data-to-decision framework and alert system.

inspector). The alert sends an email notification of the potential issue with some level of detail so that the owner can assess if further investigation is needed onsite.

The D2D framework outlined in this chapter can be the central building block of a broader asset management strategy, such as the one conceptualized in Figure 3.2. The asset management strategy is centered around a data-driven framework complete with data sourcing, analysis, and metrics around which decisions could be made. In essence, the proposed D2D framework could complement existing decision-making that is based on visual inspection and other analyses. The broader D2D links hazards (*e.g.*, earthquakes, collisions, aging), or areas of concern, to critical decisions or actions. With this objective in mind, sources of information (*e.g.*, sensors, visual inspections) are strategically determined. In particular, a sensing strategy and analytical framework are determined that address the hazards and provide quantitative insight into how the hazards can be managed. Each hazard and decision can be segmented into a component specific level (local), bridge level (global and system interaction of multiple components), or network level (considers multiple bridges and other assets in a sub-junction or set of sub-junctions). The data analysis focuses on calculating factors of safety, costs associated with addressing certain issues (*e.g.*, cost to perform maintenance versus probability and cost that not performing maintenance will result in a retrofit being required) and the ability of the bridge or network to continue functioning (or downtime for repair) if damage were to occur on a component or the entire bridge. These calculations result in quantifiable insight to be used in scheduling and prioritizing asset maintenance.

The research completed herein contributes to a very important and significant step towards a network wide powerful data-driven D2D framework for asset management. This

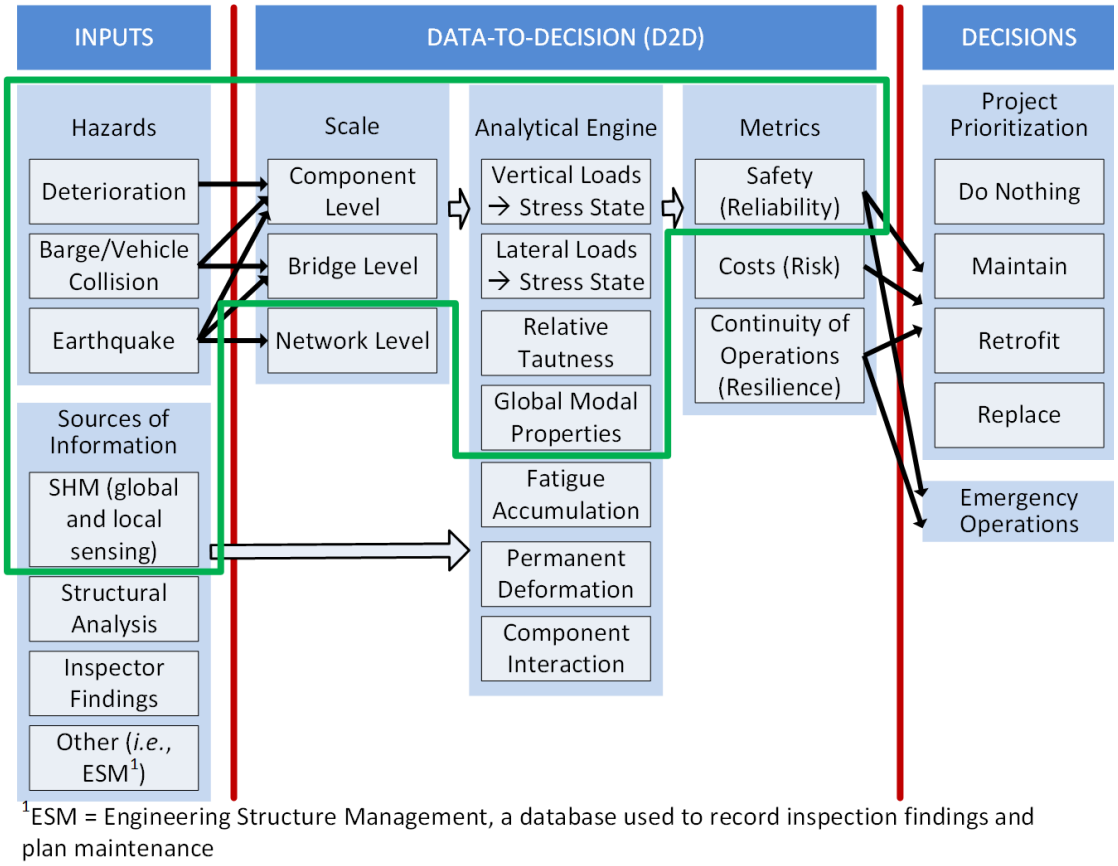

Figure 3.2 Data-to-decision framework; the key tasks implemented in this chapter are enclosed by the green line.

chapter focuses on the D2D portion of the asset management tool. Specifically, the focus comprises the SHM system that addresses all the identified hazards, local sensing focused on component safety (reliability), global sensing focused on bridge level safety and a resultant output metric that can easily be used by bridge owners to inform decisions (these focuses are outlined in green in Figure 3.2),. More precisely, the D2D system sends alert email notifications to the bridge owner when possibly safety issues arise and provides data to the owner to further assess potential issues.

3.1.3 Harahan Bridge

The Harahan Bridge, pictured in Figure 3.3, spans the Mississippi River near Memphis, Tennessee. It is part of the Memphis sub-junction of the Union Pacific Railroad network. This bridge stands to benefit greatly from a D2D system because of its exposure to multiple hazards. It is located in the New Madrid fault zone, may experience scour or flooding events from the Mississippi River and is susceptible to barge collisions. Weathering and loading can also contribute to deterioration of individual structural members including corrosion and fatigue; these effects are deemed as an aging "hazard." Thus, both global and local sensing approaches are needed.

The Harahan Bridge is a five-span cantilever truss bridge designed by Ralph Modjeski and opened in 1916. The carbon and alloy steel structure supports two rail lines carrying trains 4913 feet (1497.5 m) across the Mississippi River just west of Memphis. Note that the main bridge (five spans) stretches 2550 feet (777.2 m); to the west of the five main spans is a tower girder and viaduct that continues 2363 feet (720.2 m). The majority

Figure 3.3 View of Harahan Bridge looking south from east bank (Machnitzki 2010).

of the cross-section (Figure 3.4) carries railroad traffic; there are two side roadways that are not owned by Union Pacific, one currently unused and the other serving as a pedestrian walkway. As can be seen in Figure 3.4, the cross-section of the bridge consists of four smaller floor stringers (two on each side) supporting the lightly/unused roadways, two truss chords located at the bottom of each truss, and four interior floor stringers.

3.2 Wireless Bridge Monitoring System Design

3.2.1 Bridge Instrumentation

This section discusses the design and installation of the wireless monitoring system integrated onto the Harahan Bridge. The key purpose of the monitoring system is to provide a data for the D2D framework. A sensor instrumentation strategy is developed with the objective of implementing an alert system that considers both local and global

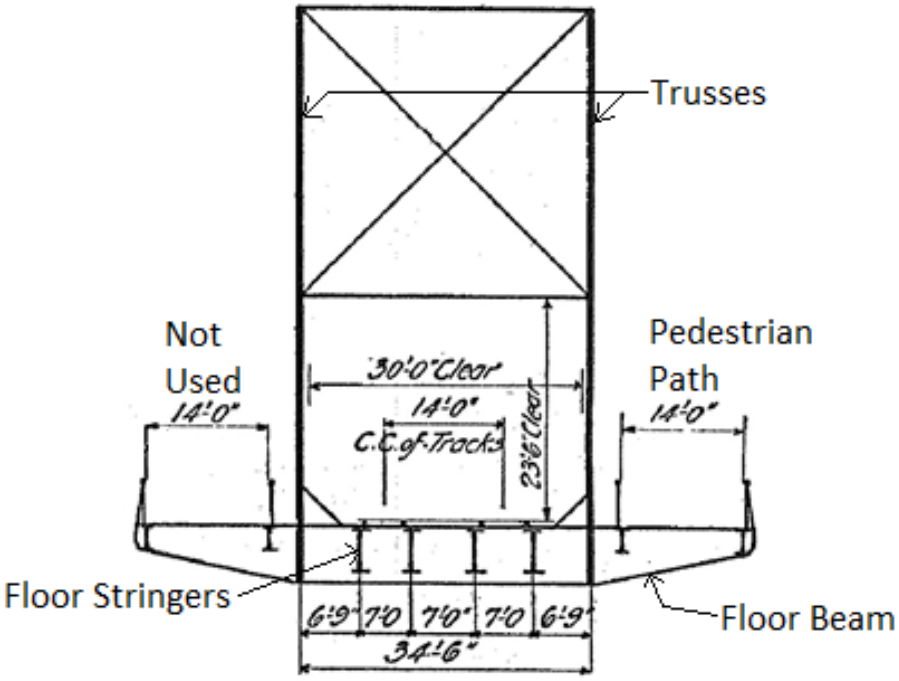

Figure 3.4 Cross-section of Harahan Bridge.

bridge behavior. Past visual inspection records, bridge owner input and preliminary FEM models are used to inform the instrumentation strategy. The instrumentation focuses on the east side (the side closest to Memphis, TN) of the bridge and address the need to monitor the following bridge properties:

- global modal properties;
- lateral loads (*i.e.*, earthquake, wind and barge collision);
- vertical loads;
- relative tautness of parallel eyebars.

The sensor layout is outlined in Table 3.1 and shown Figure 3.5. Notice that a single sensor can serve multiple functionalities. In consultation with the bridge owner, the eyebar elements in the Harahan truss system are of great interest The Harahan has 67 (28 top chord, 4 bottom chord, 31 diagonal truss and 4 vertical truss) such elements which consist of 6 parallel eyebar plates (in most cases) on each truss (north and south) designed to carry axial tension. These elements are generally long chord elements carrying high axial loads. They can be prone to fatigue damage over time (such was the case in the San Francisco – Oakland Bay Bridge (Gostautas and Tamutus 2015; Reid 2010)). In addition, the load distribution across the parallel eyebar plates can change leading to greater axial load on plates (leading to an acceleration of fatigue damage accumulation). Due to these concerns, the monitoring system selects eyebar chord LS0 – US0 (on the north and south truss system) as a primary component to monitor. LS0 – US0 is a vertical member with a length of 55 feet 1 ½ inches (16.8 m); it is comprised of a lower built-up section (US0 – MS0) that is 13 feet 3 inches (4 m) with a gross cross-sectional area of 127.5 inches^2 (822.6 cm^2) and an upper eyebar element (MS0 – US0) that is 41 feet 10 ½ inches (12.8 m)

Table 3.1 Equipment summary

Qty	Equipment type	Model	Location	Sensing type	Key attributes
12	Weldable strain gages (1 channel each)	Hitec HBWF-35-125-6-10GP-TR	LS0 – MS0, LC5 – MC5	Local strain	Gage factor = 4.3, gain = 500, resolution = 0.028 με, range = +/-930 με
12	Accelerometers (uni-axial – 1 channel each)	Silicon Design 2012-002	MS0 – US0	Local acceleration	Sensitivity = 1000 mV/g, resolution = 76 μg, range = +/-2g, frequency = 0 – 300 Hz
4	Accelerometers (tri-axial – 3 channels each)	Silicon Design 2422-005	LS0, LS2	Global acceleration	Sensitivity = 400 mV/g, resolution = 191 μg, range = +/- 5g, frequency = 0 – 400 Hz
2	Geophone	GeoSpace Geo-11D 4.5-380 VT	Basestations (pedestrian walkway, and pier)	Global velocity (trigger)	Sensitivity = 0.81 V/in/sec, resolution = 0.006 in/sec, natural frequency = 4.5 Hz,
14	*Narada* wireless sensor nodes	-	-	-	IEEE802.15.4 operating at 2.4 GHz (ZigBee)
36, {2}	Wireless channels {wired channels}	-	-	-	-

and.consists of 6 parallel eyebars. Each eyebar cross-section is 16 inches x 1 ¾ inches (40.6 cm x 4.4 cm) resulting in a cross-sectional area of 28 inches^2 (180.6 cm^2) per eyebar and 168 inches^2 (1083.9 cm^2) overall. To acquire insight to the train locomotive/car axle loads, the system also monitors the LC5 – MC5 chord which is adjacent to the eyebar chords in the same truss panel. The element is a built-up box section with a length of 27 feet 4 ¼ inches (8.3 m) and a gross cross-sectional area of 39 inches^2 (251.6 cm^2). Due to the geometric configuration of the vertical truss chord with only longitudinal chords framing into the chord's lower node, in theory it should carry the entirety of the train axle loads. Hence, monitoring axial strain should give a crude measure of train axle loads. The

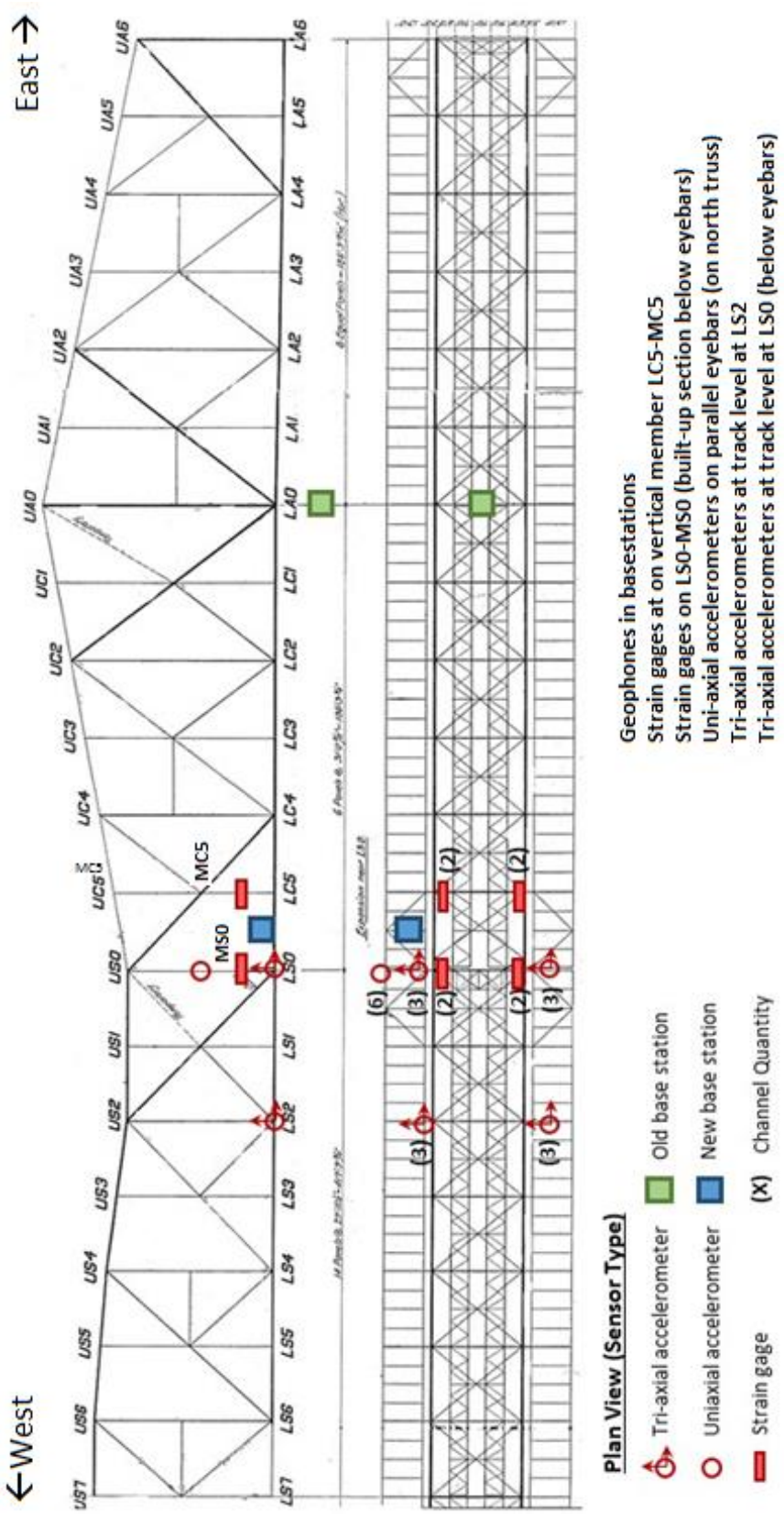

Figure 3.5 Harahan Bridge instrumentation plan.

instrumentation used to monitor the eyebar chords and vertical truss chords is described next.

The system contains 36 wireless measurement channels and 14 wireless sensing nodes (*Narada* wireless sensing nodes (Swartz et al. 2005)). There are also two wired channels for the geophones located inside the two basestations. Each wireless sensor node (Figure 3.6) consists of two waterproof transparent plastic boxes that are connected to each other with short wires. One is the wireless sensor box which seals the sensor(s), *Narada*, and sensor interface circuitry (e.g. filter, gain) and the other is the power box which seals

(a)

(b)

Figure 3.6 Wireless sensor node: (a) left box contains battery and solar controller, and the right box contains the sensor (accelerometer), *Narada*, and conditioning circuits; (b) solar panel used for power.

a rechargeable battery and a solar charger controller. Each box is 8 ¾ inches x 5 ¾" inches x 2 5/16" inches (22.2 cm x 14.6 cm x 7.5 cm) and can be mounted to steel surfaces using rare earth magnets. Each node is powered by a 9" x 15" (22.9 cm x 38.1 cm) 10 W solar panel. As can be seen in the sensor layout of Figure 3.5, the D2D framework focuses on the critical elements on the east portion of the bridge. However, this same sensing methodology can be expanded from the east portion of the bridge to other critical elements on the remainder of the bridge. Furthermore, the successful D2D framework can be extended to additional bridges on the rail network. The remainder of this section will focus on the specific sensors installed and a description of the elements they monitor.

3.2.1.1 Basestation

The basestation is used to control the wireless sensor network (including data collection triggering), receive sensor measurements and transmit them to the University of Michigan server. The basestation consists of one PC-104 single board computer, one Morningstar 12V solar controller, one 12V SLA rechargeable battery, one 12V/5V DC converter, one Logitech HD Pro Webcam C920, one GeoSpace 11D geophone, one Sprint LTE USB modem, and one CC2420 RF transceiver (operating on ZigBee 2.4 GHz frequency) that is connected to an external high-gain omni-directional antenna. The basestation is powered by a 165 W solar panel (57 13/16" x 9 5/16" (146.8 cm x 66.8 cm)). All the components of the basestation (except the solar panel, antennas and camera) are enclosed in a waterproof metal box that is 15 ¾" x 15 ¾" x 7 ⅞" (40 cm x 40 cm x 20 cm). The camera is enclosed in a separate watertight container that is 6 ¾" x 4 ¾" x 2 ¼" (17.1 x 12.1 x 5.7 cm). The box and the external components are mounted to a pedestrian walkway located on the north side of the bridge as shown in Figure 3.7.

(a)

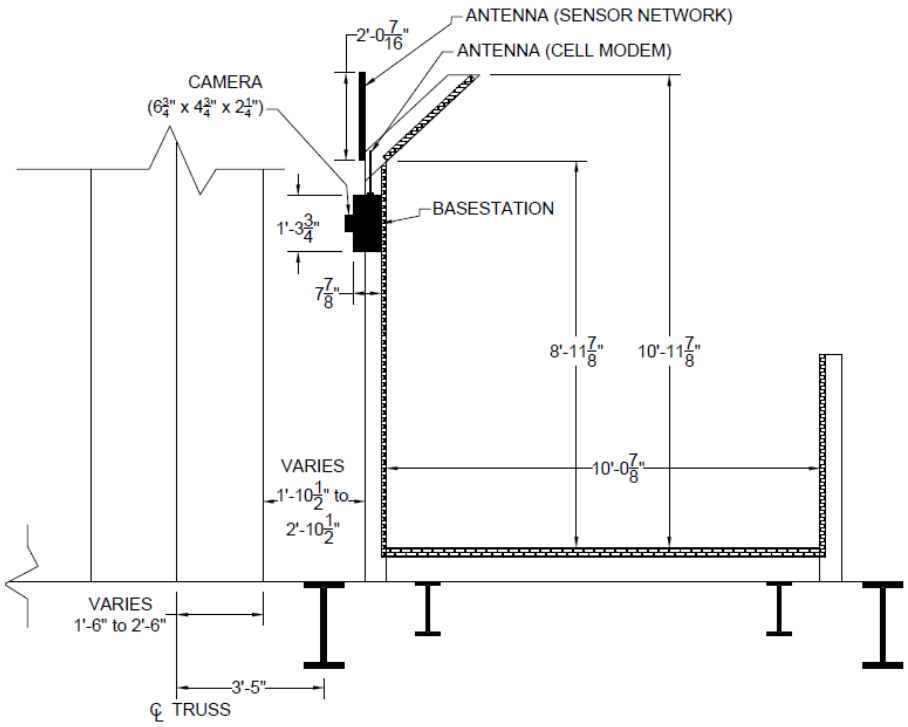

(b)

Figure 3.7 Primary basestation: (a) photograph from track level showing (from left to right) cell antenna, server enclosure, camera, ZigBee antenna, solar panel; (b) cross-section drawing of pedestrian walkway.

The geophone within the basestation enclosure is set to measure vertical velocity data continuously as wireless communication power overhead is avoided because this sensor connects directly to the server. When a train approaches the bridge it causes the geophone response to exceed a threshold of 1.24 in/s (3.15 cm/s). This triggers the server to send a wake-up command to the wireless nodes giving them sufficient time to power up and begin recording data. This "sleep-mode/wake-up mode" protocol allows for the sensor nodes to be powered by much smaller solar panels (which is vital for deployment on a structure), remain active through the night or overcast weather and for them to only record data during loading events. This threshold is set such that as a train approaches the eastern portion of the bridge, the threshold is exceeded before the train reaches the location of the other sensors. As a result, the wireless sensors have enough time to wake up and begin taking measurements. Additionally, the threshold is set high enough that is limits the number of non-loading vibrations that cause false triggers. Although a trigger is a vital component of the system, it can also be triggered manually at any time via an Internet connection to the basestation server (which has a cellular modem).

There is a second basestation located on the piercap just to the east of the primary basestation and wireless sensors; this basestation is shown in Figure 3.8. This basestation is connected to a 110 V AC outlet for power. Therefore, it contains the same equipment as the primary basestation except the solar panel, solar controller and rechargeable battery. This leads to smaller dimensions of the server enclosure (11 $^{13}/_{16}$" x 9 $^{13}/_{16}$" x 7 ⅞" (30 cm x 25 cm x 20 cm)). This station does not communicate as efficiently with the sensor nodes due to its distance and the fact that steel elements and 9 inch (22.9 cm) thick concrete fire blocking obstruct the line of sight between the sensors and basestation. However, because

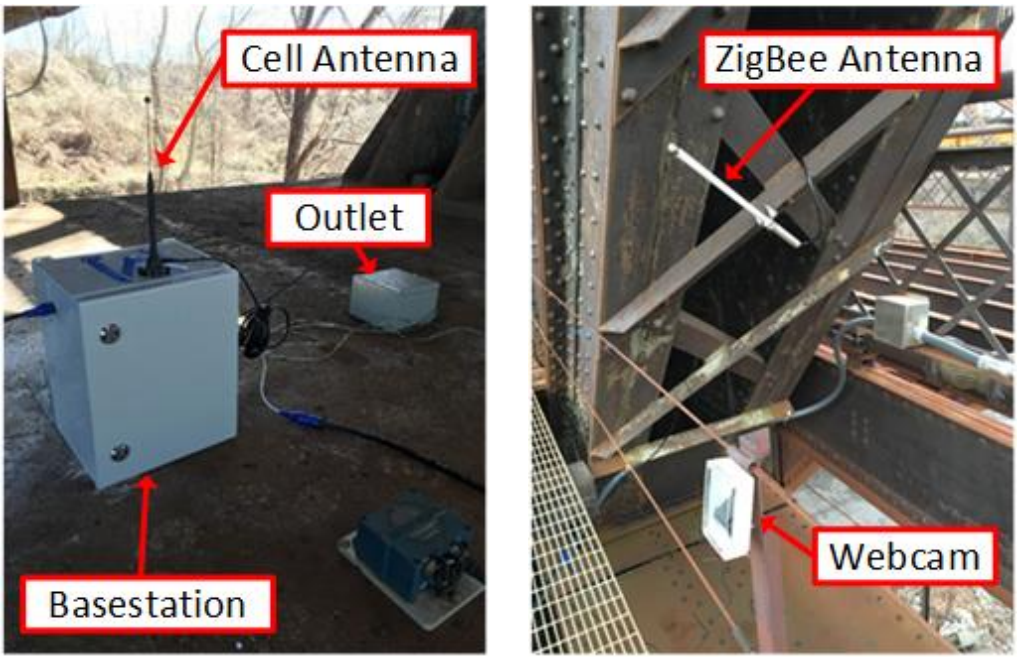

(a) (b)

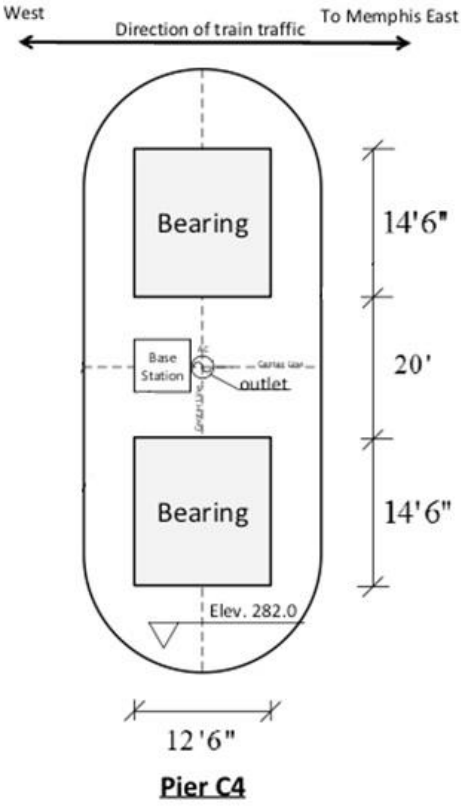

(c)

Figure 3.8 Secondary Harahan basestation: (a) photograph on piercap (from left to right) server enclosure with cell antenna on top, 110 V AC power box; (b) photograph, ZigBee antenna at track level; (c), drawing, secondary basestation installation on piercap.

of its reliable power it serves as an access point in the event of overcast, low solar power scenarios in which the primary basestation may be inaccessible. In addition to adding redundancy to the monitoring system, the geophone in the second basestation is oriented laterally to the bridge so that it can measure barge collision or seismic induced motions.

3.2.1.2 Global Modal Properties and Lateral Loads

There are four Silicon Design Model 2422 tri-axial accelerometers (SDI 2016) magnetically mounted in the floor beams near the outer truss chords at cross-sections S2 and S0 (Figure 3.5). These accelerometers are oriented with the *x*-axis longitudinal to the bridge, *y*-axis transverse to the bridge and *z*-axis vertical. Figure 3.9 depicts one of these sensors. The combination of the four tri-axial accelerometers contribute to understanding of the bridge global modal properties. Modal properties extracted from these sensors will serve to fine tune FEM models of the bridge as well as act as indicators of global changes

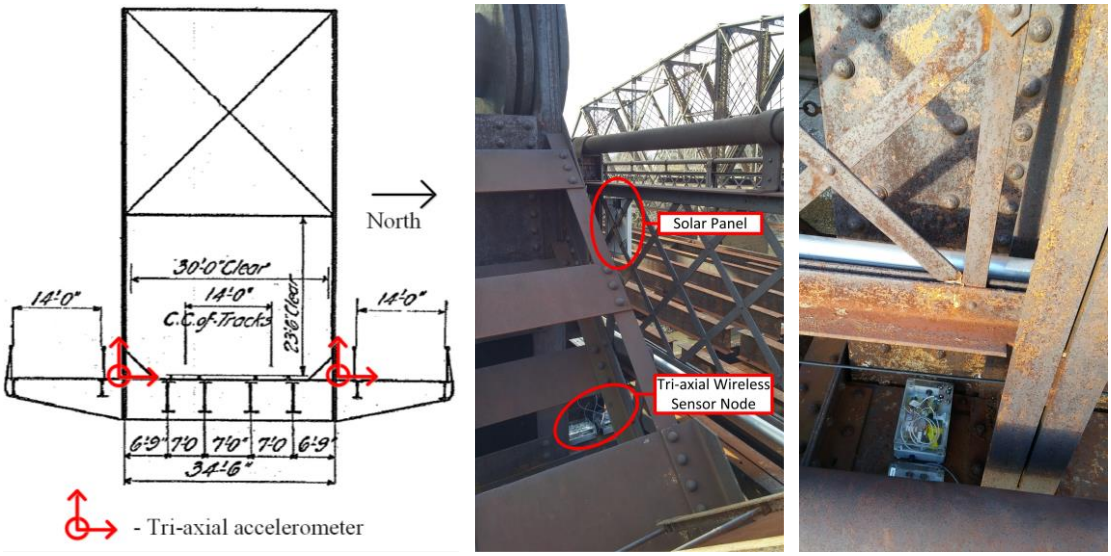

(a) (b) (c)

Figure 3.9 Tri-axial accelerometer wireless sensor node on LS0 – MS0 south truss: (a) installation on floor beam; (b) picture at LS0 – MS0 eyebar chord; (c) close-up picture.

to the bridge structure (*i.e.*, changes induced by damage). They also contribute to the lateral load monitoring and quantify the effects of wind as well as potential earthquakes or barge collisions acting on the bridge.

3.2.1.3 Truss Component Vertical Loads

The array of strain gages instrumented on the bridge are used to determine the load imposed on the bridge (train locomotive/car axle loads and total train global load) and the behavior of key truss elements (pure axial or not). Train information taken from wheel impact load detector (WILD) data and correlated to strain readings (match same train to same dataset) at multiple members on the bridge will provide a rough measure of train axle loads. This set of load data, along with strain data from the Harahan Bridge will serve as the basis for assessing component capacity versus demand, which may change due to component deterioration or changes in component boundary conditions. Hitec Products Inc. HBWF-35-125-6-10GP-TR weldable strain gages with temperature compensation (HPI 2017) are installed on the bottom section of members LS0 – MS0 and LC5 – MC5. Figure 3.10 shows a strain gage welded to a truss member. For each cross-section (LS0 – MS0 and LC5 – MC5) four gages are installed; one on the inner portion (facing the track) and one on the outer portion (facing out from the bridge) of each member on both sides of the bridge (*i.e.*, south and north truss); see Figure 3.11. Both sections are built-up sections consisting of steel box tubes with gross cross-sectional areas of 127.5 inches^2 (822.6 cm^2) and 39 inches^2 (251.6 cm^2), respectively.

(a) (b)

Figure 3.10 Strain gages (Hitec HBWF-35-125-6-10GP-TR) installed on the builtup section of S0 and vertical hangers C3: (a) pre-paint; (b) post-paint.

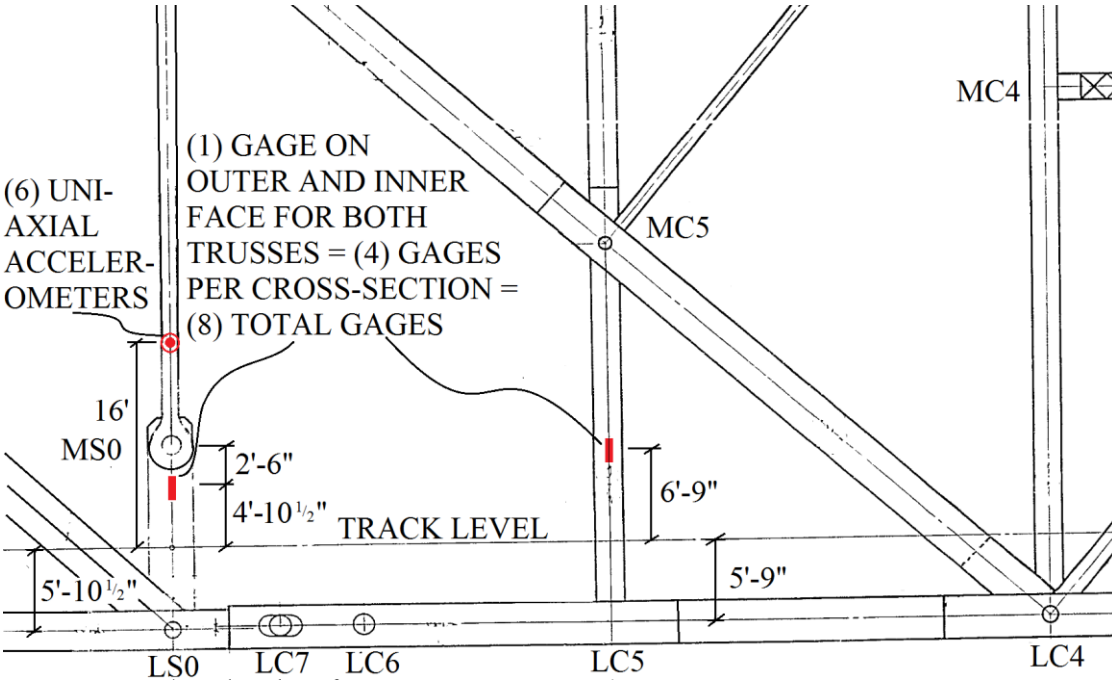

Figure 3.11 Schematic of strain gage and uni-axial accelerometer locations.

At member LS0 – MS0 the strain gages are welded on the built-up section 2 feet 6 inches (76.2 cm) below the bottom eyebar pin and 4 feet 10 ½ inches (148.6 cm) above track level on each truss. One of the installed gages is shown in Figure 3.12a. The gages on the built-up section use strain to infer the aggregate effect of the load on the member; whereas the uni-axial accelerometers on the eyebars indicate the individual eyebar's contribution to carrying the load (the uni-axial accelerometers and relative tautness are discussed subsequently). The reason for gages on the outer and inner faces of the members is to detect out-of-plane bending of the members or asymmetric strain. Having both trusses (north and south side of the bridge) instrumented allows the effects of bridge torsion and asymmetric loading to be examined. It is worth mentioning, member LS0 - US0 carries only a portion of the individual axle loads locally (due to an angled chord taking load at nod LS0); however, it has a large contribution to carrying the entire (global) load of the whole train as it crosses the bridge. Therefore, for each train crossing the strain should reveal both a large magnitude strain cycle associated with the train weight loading the bridge globally and much smaller cycles superimposed which correspond to local axle load carried by the member.

Member LC5 – MC5 is under a relatively small tension dead load but because it is the only vertical support at its respective cross-section, it carries a large portion of the vertical live load for each train axle as it crosses over the bridge. This provides a means of crudely assessing the axle load for each axle of the train. In addition, fatigue analyses can be done on this element given the large number of cycles per train. Each member on either

(a) (b)

Figure 3.12 Installed strain gages on the inner face (facing the track) of the north truss: (a) LS0 – MS0; (b) LC5 – MC5.

side of the bridge is instrumented with strain gages on their outer and inner faces 6 feet 9 inches (2.06 m) above track level, one such strain gage is shown in Figure 3.12b.

3.2.1.4 Eyebar Relative Tautness

There are six eyebars on each truss side (12 total) that constitute truss chord MS0 - US0. Each of the eyebars on the north truss is instrumented with a uni-axial accelerometer oriented to monitor out-of-plane vibration 16 feet above the track level (Figures 3.11, 3.13 and 3.14). The fundamental frequency, corresponding to the axial load being carried by each eyebar relative to the other eyebars can be calculated from these frequencies. This is a primary area of maintenance concern noted by the bridge owner and is checked manually by bridge inspectors regularly.

(a) (b) (c)

Figure 3.13 Member north truss LS0 – US0: (a) entire member (built-up section on bottom portion, 6 eyebars on upper portion; close-up on top (b) and bottom (b) of MS0 – US0 and designation of individual eyebar links.

Figure 3.14 Uni-axial accelerometers installed on eyebar portion of MS0 – US0.

3.3 Monitoring System Performance and Automated Data Processing of Bridge Behavior

3.3.1 Communication Reliability

From June 16, 2016 to January 31, 2017, the system has been in full operation and has been triggered 5,061 times. The datasets are collected from the strain gage and eyebar acceleration channels at 200 Hz for a period of 30 seconds per trigger event and for the tri-axial accelerometers (for global modal analysis) at 50 Hz for 60 seconds per trigger event. The lower sampling frequency is because the tri-axial accelerometers are used only for global frequency analyses which only has significant attributes at a lower frequencies. Based on a FEM analysis, the primary modal frequencies are 0.679 Hz (transverse), 0.878 Hz (transverse), 1.08 Hz (transverse), 1.39 Hz (vertical), and 1.50 Hz (torsional). For this 8-month period the successful wireless data packet transmission rate has been approximately 60% (52,384 packets have been successfully transmitted out of a possible 89,011). The packet transmission data are shown in Figure 3.15. Four of the nodes from the June 2016 installation trip experience hardware errors in charging the sensor node batteries with the solar panels. This issue is determined to be due to improper connections caused by a smaller gage wire than the other nodes. Aside from this hardware matter, certain factors cause the system to not successfully transmit some data packets (*i.e.*, no communication

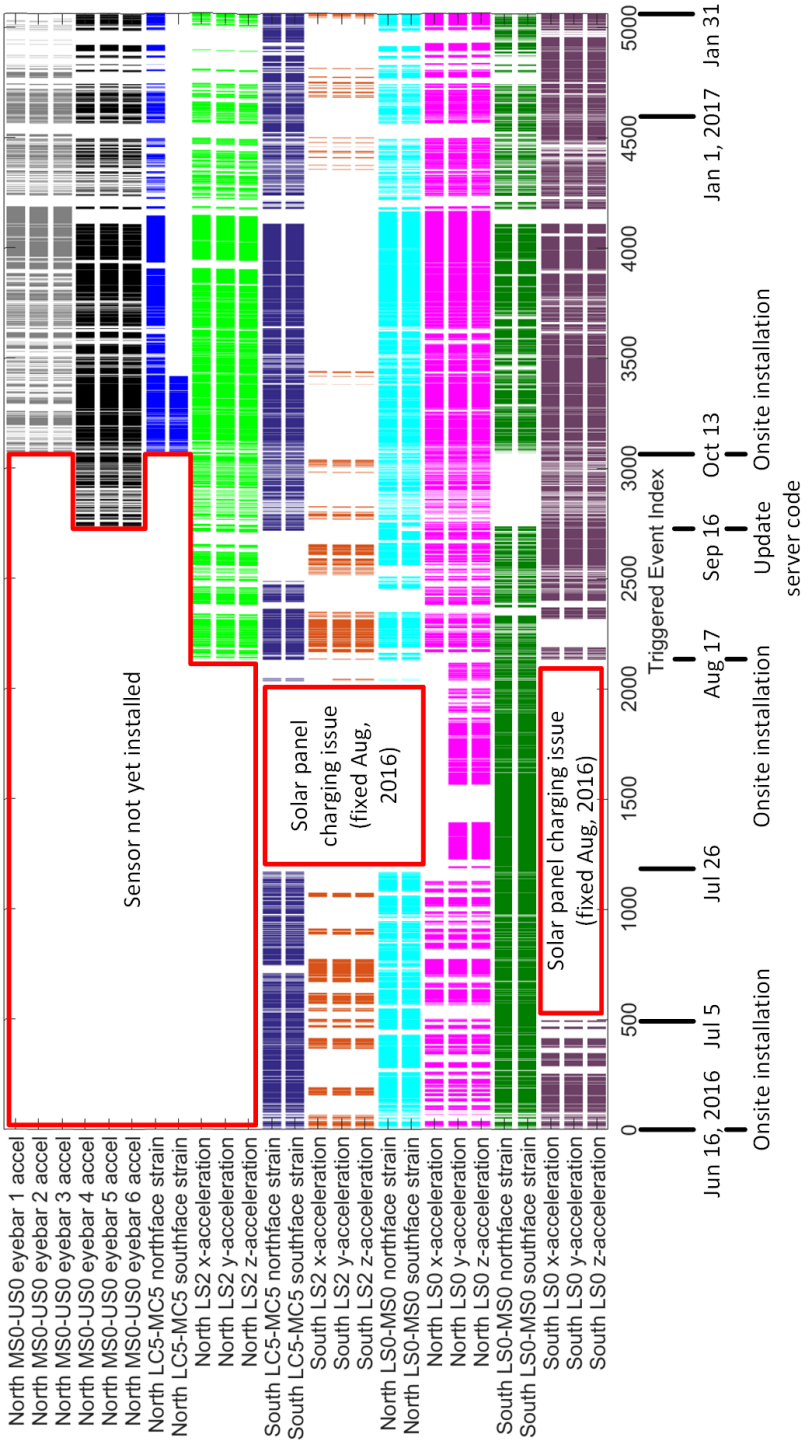

Figure 3.15 Successful wireless data packet transmission; abscissas is the trigger event numbered sequentially (correlates roughly to time but triggers are not on a scheduled basis); below abscissas, significant instances are related to both trigger event and date; each row represents a single sensor channel; the colors separate wireless sensor nodes (which contain more than one channel); a successful data transmission is indicated by a thin tick line, white spaces indicated an unsuccessful data packet transmission.

with the server) for an event. In particular, after a series of cloudy days the solar powered nodes can run too low on power and have to recharge, or the track-level nodes on the southern side of the bridge can lose communication when tall trains pass between the nodes on the south side of the bridge and the basestation on the north side. Nevertheless, the nearly 60% successful data transfer rate provides a sufficient amount of data to perform the proper analyses and alert the bridge owner of changes in bridge performance at the target areas of interest.

3.3.2 Global Modal Properties and Lateral Loads

The acceleration data from the four tri-axial accelerometers at track level are analyzed in the frequency domain. Figure 3.16 shows a sample fast Fourier transform (fft) of a train event on October 30, 2016. Notice the fundamental frequencies of the various mode shapes (*e.g.*, transverse, vertical, torsional) being excited below 4 Hz, with component, or local, modes being excited at higher frequencies. The Harahan Bridge has

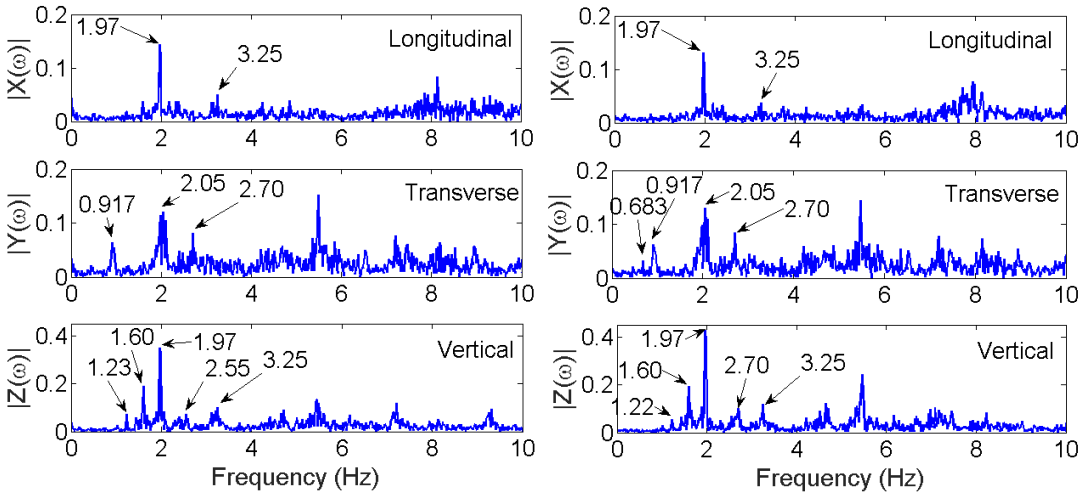

Figure 3.16 Frequency domain response (fft) to a train event at 19:02 EST, Sunday, October 30, 2016, recall, *x*-axis is longitudinal, *y*-axis is transverse and *z*-axis is vertical to bridge: (a) South LS2 (b) North LS2.

been modeled in the CSiBridge add-on to SAP2000 (CSiBridge 2013), a commercial FEM package. The bridge modal properties as extracted from the FEM model and as measured by the four tri-axial accelerometers are tabulated in Table 3.2. As seen in Table 3.2, the modal frequencies line up well but calibration of the FEM model can be performed to align the model better with the experimentally determined modal frequencies. These accelerometers also monitor lateral accelerations derived from ground motion or barge collisions. However, since being instrumented the bridge has not experienced these types of heavy lateral loadings.

3.3.3 Truss Component Vertical Loads

Figure 3.17 shows a sample time history of strain at the south truss at LS0 – MS0 and LC5 – MC5. Notice, the strain steadily increases at LS0 – MS0 (which is the member that carries the load in a more global manner), whereas, the strain remains relatively low until the moment the train reaches the member at LC5 – MC5. The strain levels are being monitored as part of the alert system, such that if the strain exceeds a certain threshold an email is sent to the bridge owner. Two approaches to determine this threshold are considered. The first approach follows the American Railway Engineering and Maintenance-of-Way Association design guidelines (AREMA 2016) which are similar to Allowable Stress Design (ASD) and are the same guidelines followed in designing railway

Table 3.2 Simulated and measured modal frequencies.

Mode #	**Mode type**	**Simulated modal frequency (Hz)**	**Experimental (measured) modal frequency (Hz)**
1	Transverse	0.679	0.683
2	Transverse	0.878	0.917
3	Transverse	1.08	-
4	Vertical	1.39	1.23
5	Torsional	1.50	-

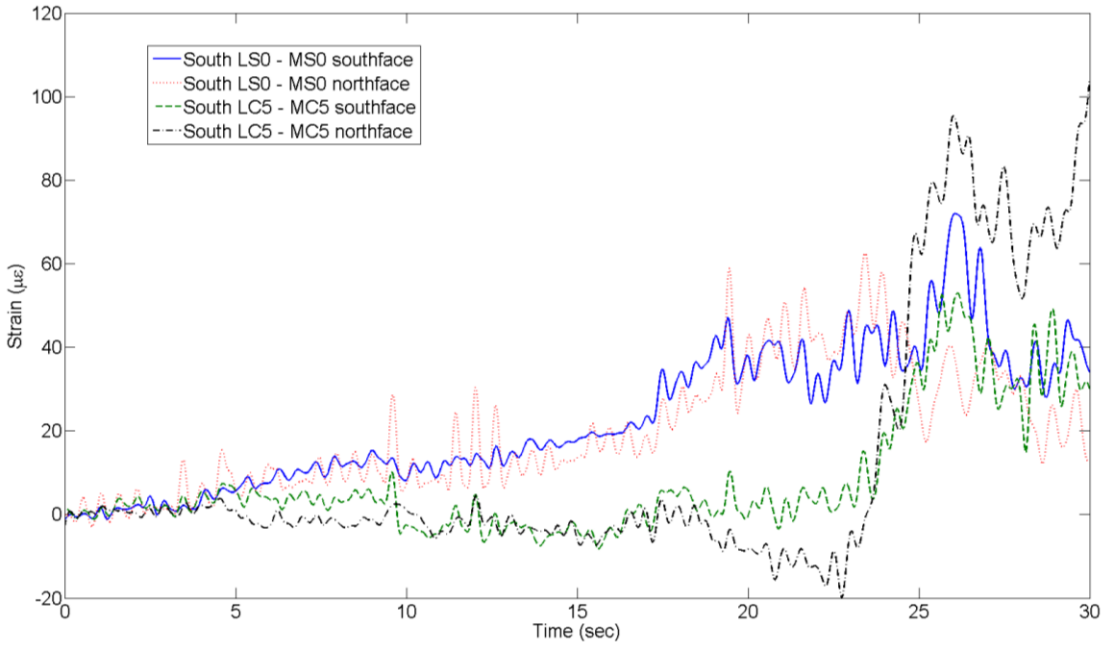

Figure 3.17 Strain time series for LS0 – MS0 south truss and LC5 – MC5 south truss, collected at 13:56 EST, Monday, November 14, 2016

bridges. Following the AREMA guidelines, a combination of various load types is considered and the resultant stress from this load combination must be below a certain percentage (specified based on member type, *e.g.*, axial tension, axial compression, floor beam) of the yield stress of the material with which the member is constructed (the percentage criteria is essentially the inverse factor of safety). However, these guidelines do not account for uncertainty in the dead load, they simply require an overall factor of safety above a certain value. Because the dead load is the only load type not being measured (the strain gage measures strain from all other types of loads) a second approach is considered that accounts for uncertainty in dead load. The second approach follows AASHTO LRFD (AASHTO 2012) design guidelines. However, even following these guidelines that give a more conservative estimate of dead load, the AREMA guidelines still result in a lower, or more conservative, strain threshold. Where this is an alert system signaling further attention needs to be given to a specific component, the threshold that

alerts the trigger should be conservative. Additionally, railway bridges' design practice follows AREMA design guidelines so it is only practical to have the alert system follow the same guidelines. Therefore, the alert system threshold is calculated following AREMA guidelines, these guidelines consider any combination of the following loads resulting in the largest stress on a member:

$$D_L + L_L + I_{LL} + W_T + W_B + L_{CF} + L_N + (L_B \; or \; L_T) + L_{ICE} + E \leq (S_{LS}\sigma_y)A_g, \quad (3.1)$$

where, D_L is dead load, L_L is live load, I_{LL} impact live load, W_T is wind load on the train, W_B is wind load on the bridge, L_{CF} is the centrifugal force load (if tracks have curvature, which is not the case on Harahan), L_N is nosing or rocking load, L_B is braking load, L_T is traction load, L_{ICE} is ice load, E is seismic (or earthquake) load, $S_{LS}$is the limit state (or permissible percentage of the yield stress), σ_y is the yield stress, and A_G is the gross section area of the member. Because the instrumented members are axial loaded members and axial strain is being measured, all of the load types are captured with the strain gage measurement except the D_L which must be estimated from engineering reports/design documentation or FEM models. Therefore, the equation becomes:

$$D_L + L_M \leq (S_{LS}\sigma_y)A_g, \quad (3.2)$$

where, L_M is the measured load; which is equal to $EA_g\epsilon_M$, where E is the modulus of elasticity and ϵ_M is the measured strain. Substituting for L_M and isolating ϵ_M on the left side of the equation yields:

$$\epsilon_M \leq \frac{S_{LS}\sigma_y}{E} - \frac{D_L}{EA_g}. \quad (3.3)$$

Both LS0 – MS0 and LC5 – MC5 are tension floorbeam hangers connected with rivets; therefore S_{LS} = 0.40 per AREMA (AREMA 2016). The members are alloy steel (LS0 – MS0) and carbon steel (LC5 – MC5) with σ_y of 50 ksi (345 MPa) and 37 ksi (255 MPa), respectively. Both steel materials have a modulus, E, of 29,000 ksi (200 GPa). The dead loads, D_L, are determined from the engineering design drawings, and verified with the SAP2000 model, to be 1,332 kips (5,925 kN) tension and 115 kips (512 kN) tension, respectively. The gross cross-section areas, A_g, are 127.5 in^2 (822.6 cm^2) and 39 in^2 (251.6 cm^2), respectively. Using these values to calculate the limit state, or measured strain threshold at the members being monitored results in $\epsilon_M \leq 329\ \mu\epsilon$ for LS0 – MS0 and $\epsilon_M \leq 409\ \mu\epsilon$ for LC5 – MC5. In order to provide ample warning and allow for preventative maintenance to be performed if limit states are indeed being reached, the alert system is set to trigger at 2/3 of the maximum strain threshold allowed (*i.e.*, 329 $\mu\epsilon$ for LS0 – MS0 and 409 $\mu\epsilon$ for LC5 – MC5). This means the alert for the four strain gages on LS0 – MS0 is set to send a notification if the strain in one or more gages exceeds 220 $\mu\epsilon$ and the alert for the four strain gages on LC5 – MC5 is sent if a gage measures a strain greater than 272 $\mu\epsilon$. The threshold of 2/3 the limit state can be adjusted by the bridge owner if desired.

3.3.4 Eyebar Relative Tautness

Each eyebar link in the eyebar truss components (MS0 – US0) is designed to carry an even portion of the tensile load at the given member. These links are governed by two limit states: similar to the built-up sections (LS0 – MS0 and LC5 – MC5), the eyebars must not exceed a certain stress threshold; additionally, fatigue in the parallel eyebars relative to each other must not be disproportional, otherwise, if the load is not distributed evenly and

one eyebar link carries a large portion of the load, it can experience accelerated fatigue accumulation which may result in major failure such as on the San Francisco – Oakland Bay Bridge (Gostautas and Tamutus 2015; Reid 2010). Standard practice for Union Pacific is to inspect these elements by physically shaking each eyebar and counting the number of vibration cycles relative to the other eyebar links to crudely assess relative tautness in parallel eyebar links (UPR 2013). The wireless sensing strategy allows for this analysis to be both quantitative and performed continuously rather than periodically. Rather than monitor these two limit states with strain as the measurand, acceleration is alternatively monitored. This is because acceleration can be used to determine the eyebar links relative tautness to each other by taking into account both dead and live load (whereas strain only measures live load). More importantly, measuring out-of-plane acceleration to derive natural frequencies directly relates to the current practice that visual inspectors employ to determine natural frequencies. Thus, making the adoption of this automated D2D framework more feasible.

The load in each eyebar link can be calculated using the following equation (Kollár 2003):

$$\frac{\omega_i^2}{\omega_0^2} = 1 + \frac{N_i}{N_E}, \tag{3.4}$$

where, ω_i is the measured natural frequency of eyebar *i* in a loaded state, ω_0 is the natural frequency of the eyebar if it were unloaded, N_i is the total axial load ($D_L + L_L + \cdots$ other loads, and positive, (+), denotes tensile loading) in eyebar *i*, and N_E is the Euler buckling load for the eyebar. Note that ω_i and ω_0 must either both be in radians or both be in Hz (*i.e.*, f_i and f_0). Rearranging Equation 3.4 gives:

$$N_i = N_E(\frac{\omega_i^2}{\omega_0^2} - 1), \tag{3.5}$$

with the Euler buckling load is defined as (Hibbeler 2011):

$$N_E = \frac{n^2\pi^2 EI}{L^2}. \tag{3.6}$$

Here, n is determined based on the boundary conditions of the eyebar ($n = 1$ for simply supported and $n = 2$ for fixed-fixed support) and L is the length of the eyebar. The unloaded natural frequency is defined as (Blevins 2016):

$$\omega_0 = k^2\sqrt{\frac{EI}{A_g\rho L^4}}, \tag{3.7}$$

where, k is determined based on the boundary conditions of the eyebar ($k = 3.142$ for simply supported and $k = 4.730$ for fixed-fixed support) and ρ is the density of the eyebar. The total load for the eyebar truss component is the summation of the load in each link:

$$N = \sum_{i=1}^{m_{eb}} N_i, \tag{3.8}$$

where, m_{eb} is the number of eyebar links in the component (six (6) for MS0 – US0). The ratio of load proportion carried by each eyebar, R_i, is:

$$R_i = \frac{N_i}{N}, \tag{3.9}$$

For MS0 – US0 the properties are: E of 29,000 ksi (200 GPa), the dimensions of each eyebar link are 16 inches x 1 ¾ inches (40.64 cm x 4.45 cm) and result in an A_g of 28 inches^2 (180.6 cm^2) and I of 7.1458 inches^4 (2.9743 x 10^{-6} m^4), L of 41 feet 10 ½ inches (12.7635 m) and ρ of 0.2836 lbm/in^3 (7849 kg/m^3). The boundary conditions (which determine n and k) for the eyebar links for out-of-plane bending are fixed-fixed based on the engineering drawings and observation of the as-built structure. This determination of

boundary conditions is also validated subsequently with dead load-only calculations using measured data, and Equations 3.5 and 3.8 resulting in the correct dead load as determined through engineering drawings. These equations and accompanying properties are combined with the measured fundamental frequency of the eyebar links to monitor the eyebar loading. Figure 3.18 shows the frequency response of each eyebar to a single train loading event with the fundamental frequencies labeled. The fundamental frequencies result in calculated loads of 252.8 kips (1125 kN), 285.4 kips (1270 kN), 271.2 kips (1206 kN), 226.3 kips (1007 kN), 248.3 kips (1104 kN) and 266.5 kips (1185 kN) for Eyebars 1, 2, 3, 4, 5 and 6, respectively. This in turn corresponds to respective load distribution ratios of 16.3%, 18.4%, 17.5%, 14.6%, 16.0% and 17.2% which is close to the ideal 16.67% expected when perfectly balanced. Note that stress concentration points and non-axial behavior where ignored for the purposes of this relative tautness analysis.

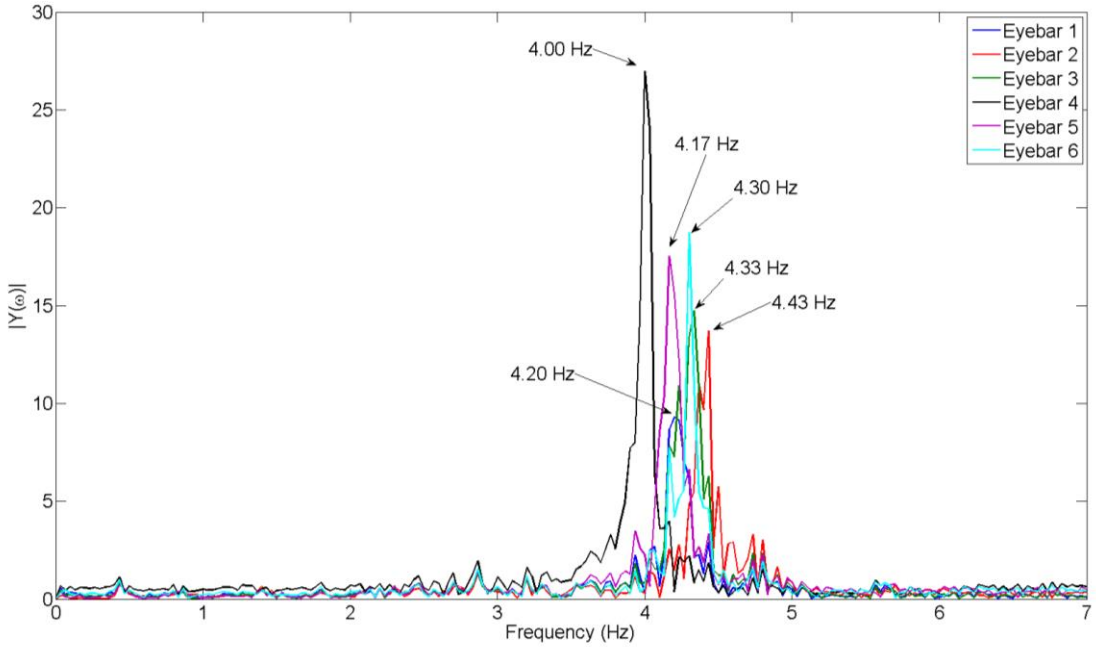

Figure 3.18 Frequency domain response (fft) of out-of-plane acceleration for each eyebar link at MS0 – US0 on the north truss to a train event at 19:21 EST, Tuesday, December 20, 2016.

These same calculations are carried out for all train events that successfully collect acceleration data for all six eyebar accelerometers from December 15, 2016 – January 31, 2017 and are shown in Figures 3.19 and 3.20. The results for the load in each eyebar for a given train event (Figure 3.19) are compared to the limit state presented in Equation 3.2, substituting $N_i = D_L + L_M$, and using the eyebar yield stress of $\sigma_y = 55$ ksi (379 MPa), S_{LS} = 0.40 because the axial eyebars are part of a hanger member, A_g = 28 in^2 (180.6 cm^2) results in a limit state of 616 kips (2740 kN), using the threshold of 2/3 the limit state results in a trigger threshold of 411 kips (1828 kN). All of the events monitored to this point (a portion of which are shown in Figure 3.19) fall below this threshold.

A perfect load distribution scenario would result in each eyebar carrying 16.67% of the load. However, the eyebar component exhibits an uneven distribution of loading as can be seen in Figure 3.20. Figure 3.20 plots the percent load distribution each eyebar

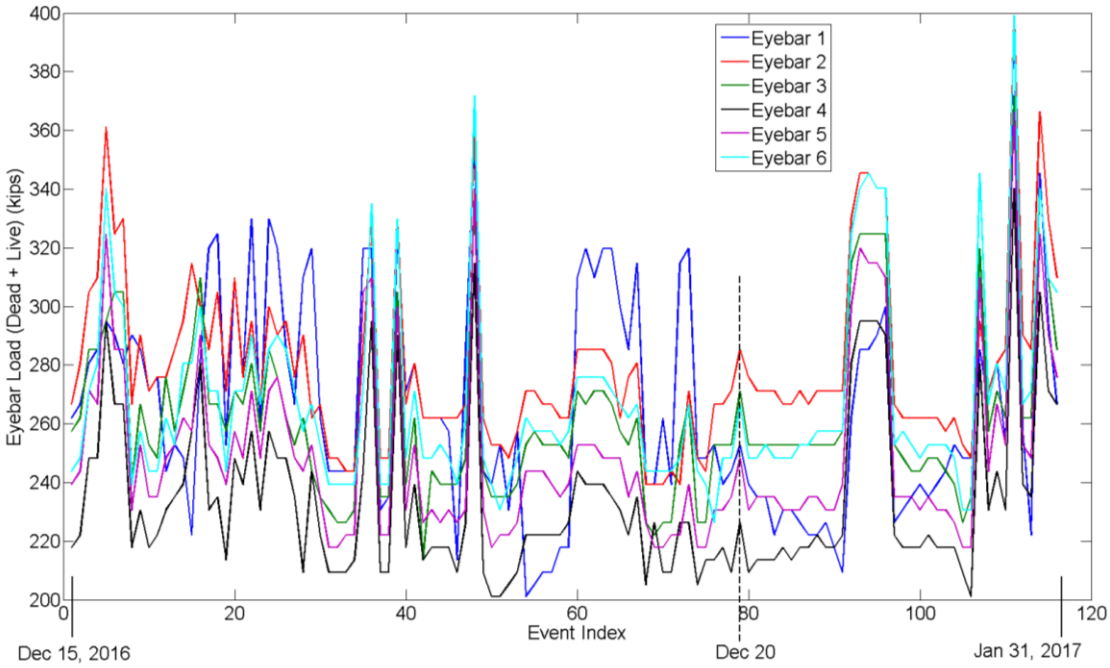

Figure 3.19 Load distribution for eyebar links on north MS0 – US0 from December 15, 2016 to January 31, 2017.

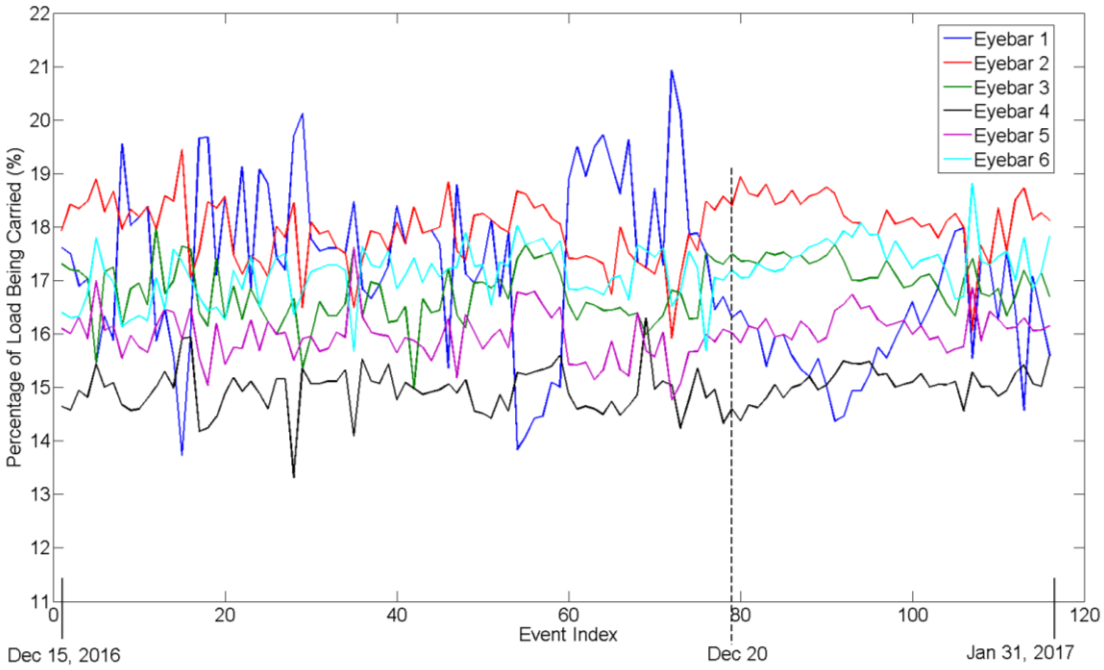

Figure 3.20 Ratio of load being carried by each eyebar link on north MS0 – US0 from December 15, 2016 to January 31, 2017.

carries for each train-crossing event. The ratio that each eyebar carries remains relatively close to one another for all of the monitored events and there are no eyebars that show a trend towards carrying an excessive percentage of the load. However, the load distribution between eyebars varies between different events; therefore, the percent of load being carried for each event is accumulated in a separate histogram for each individual eyebar and fit to a Gaussian curve. In this manner, the percent of the load each eyebar is carrying for the majority of train events can be determined. The Gaussian fits to each histogram are plotted together in Figure 3.21. It can be seen that the load distribution falls between 14% and 19% for all eyebars. Eyebar 1 shows that it varies the most between separate train events. Nonetheless, its distribution does not vary very far from the ideal 16.67%.

To determine if this range of load ratios should raise concern, the fatigue accumulation for the eyebars is examined. Fatigue accumulation is largely controlled by

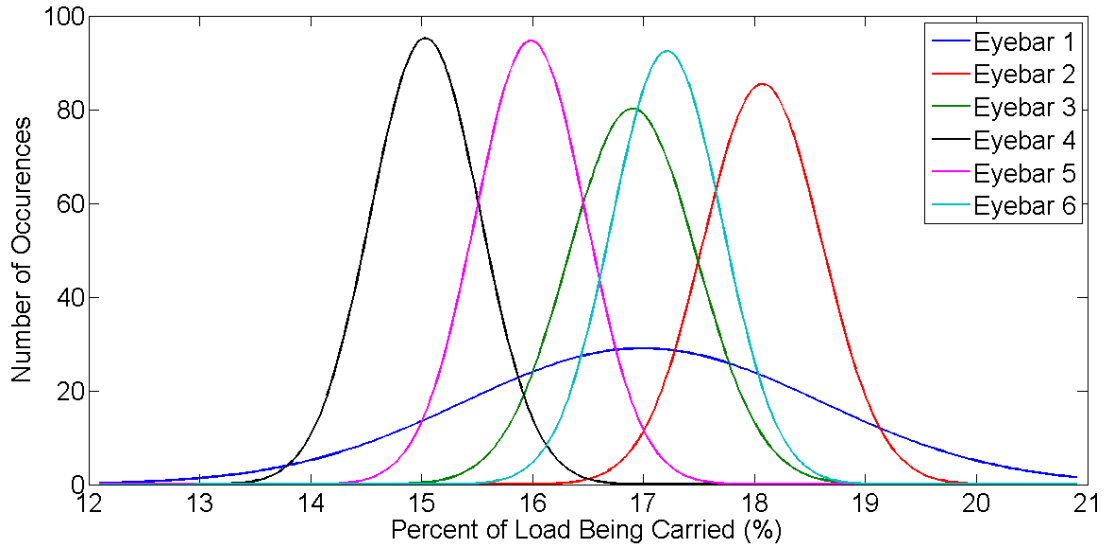

Figure 3.21 Gaussian distribution of histograms for the percent of load being carried by each eyebar link on north MS0 – US0 from December 15, 2016 to January 31, 2017.

live load. For this study it is assumed that the load distribution of dead load is the same as the distribution of live load. Therefore, the dead load in a given eyebar can be calculated as the total dead load (1332 kips (5925 kN)) times the load distribution ratio, R_i, and the live load calculated as $L_{Li} = N_i - D_L$. In order to calculate the consumed fatigue, Miner's Rule (Miner, 1945) can be followed in the same way as in Chapter 2:

$$C_i = \sum_{j=1}^{k} \frac{n_{F_{ij}}}{N_{F_{ij}}}, \tag{3.10}$$

where, i indicates the eyebar, j indicates the stress (load) range, C_i is the fraction of the consumed fatigue, $n_{F_{ij}}$ is the number of cycles accumulated at stress $S_{F_{ij}}$ (where $S_{F_{ij}} = \frac{L_{Lij}}{A_g}$), and $N_{F_{ij}}$ is the number of cycles a specimen can withstand at the given stress range ($S_{F_{ij}}$). AASHTO (2012) provides S-N curves for bridge elements, these same curves have

been adopted by AREMA (2016). The S-N curves have an exponential relationship (log-log linear slope) between stress range and number of cycles that follows:

$$N_{F_{ij}} = K S_{F_{ij}}^{-m}, \tag{3.11}$$

where K shifts the curve up or down based on the category of the structural component and m is the log-log slope. The eyebar is classified as category E, which has a K value of 3 x 10^{11} and all categories have m equal to 3. The trigger threshold for the consumed fatigue for each eyebar relative to one another is set to send an alert when the rate of consumed fatigue increases by 50% from that which would be expected if the loading scenario were ideal with 16.67% of the load carried by each eyebar. Relating Equation 3.10 to 3.11 (with the help of the AASHTO, category E, S-N curve plotted in Figure 3.22) this threshold is determined by calculating the stress range that would cause $N_{F_{ij}}$ (abscissa in Figure 3.22) in Equation 3.11 to be reduced to 66.67% of its original value (recall from Equation 3.11 that $C_i \propto \frac{1}{N_{F_{ij}}}$; therefore, $1.5\ C_i = \frac{1}{0.6667\ N_{F_{ij}}}$). The values for the S-N curve equations show that a 14.47% increase in stress range, $S_{F_{ij}}$ (ordinate in Figure 3.22), which directly corresponds to axial load, results in a 33.33% reduction in fatigue life (corresponding to a 50% increase in the rate of fatigue accumulation). That is, for a given train load event, if the load were to change from being distributed evenly (16.67% each eyebar) to having one or more eyebars carrying 19.08% (1.1447 x 16.67%) of the load, the resulting change in stress would cause the member to fatigue at 1.5 times the rate that it normally would for the given load. Therefore, the analytical engine of the D2D framework is set to send an alert if the ratio of load distribution for any eyebar is greater than 19.08%. The threshold for triggering when the fatigue rate increases by 50% can be changed to a different factor

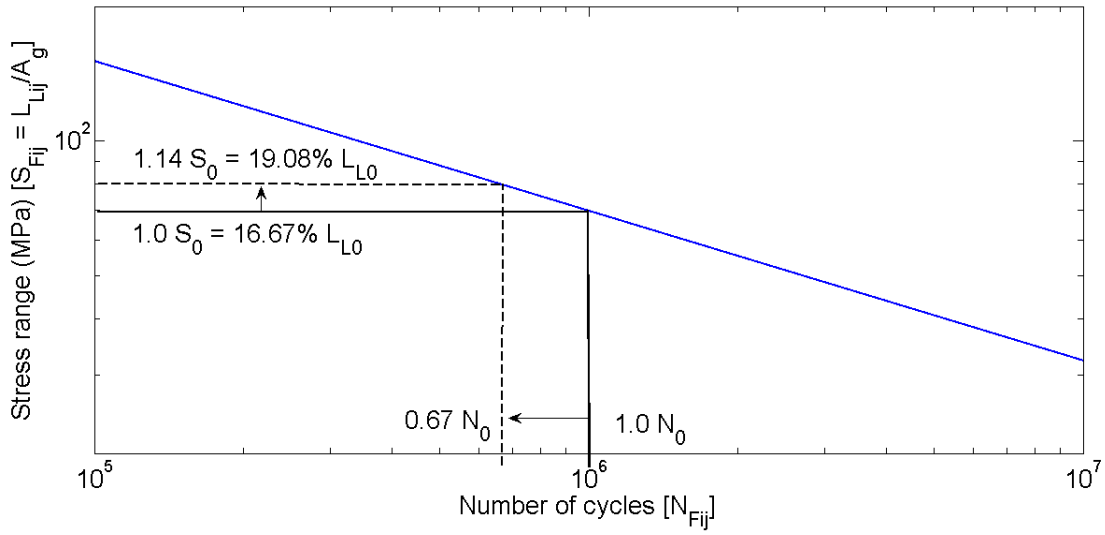

Figure 3.22 AASHTO, category E, S-N curve with illustrations to show 50% increase fatigue accumulation (33.3% reduction in number of cycles) (AASHTO 2012).

by the bridge owner. Also, when an alert is sent from either this trigger or for the trigger based on total load in an eyebar, both the ratio and overall load should be examined further. For example, the high ratio being carried by Eyebar 1 for event index 72 in Figure 3.20 does not correspond to a large overall load in Eyebar 1 as seen in Figure 3.19. Conversely, the large load experienced in event index 111 in Figure 3.19 does not correspond to large variance in load distribution as seen in Figure 3.20. Having both types of triggers allows for the bridge owner to know when further examination may be required as well as more thorough examination to be conducted without requiring a visit to the bridge site. Additionally, plots similar to Figure 3.19 and 3.20 can greatly enhance the frequency and efficacy of periodic inspections. Moreover, a plot similar to Figure 3.21 which depicts the histograms of the percent of load being carried for each eyebar can be automatically generated and if the peak of one eyebar begins to drift towards 19.08% further action can be taken. For example, every two or three months, or when a train event causes an alert to be sent, the bridge owner can look at two simple plots, without having to visit the bridge,

and recognize if one eyebar is trending towards carrying more of the load (using a plot similar to Figure 3.21), or if overall stresses are increasing (using a plot similar to Figure 3.19). Thus allowing for potential concerns to be addressed at a much earlier stage.

3.4 Chapter Summary

This monitoring project includes the development of an online database that can be seamlessly integrated with Union Pacific's current set of databases. This database will fuse visual inspections, structural and finite element (FE) analyses, and train load and sensing data in order to provide a comprehensive dashboard for use in decision-making. The contributions of the work presented in this dissertation are the development of a two-tiered alert system that incorporates the online database to enable an automated D2D framework. The first tier of the alert system triggers the wireless monitoring system (developed and described in this chapter) to wake-up from a low-power state and record measurements only for loading events in order to conserve energy. The second tier processes the data after it has been transmitted wirelessly to the basestation server then via the Internet to an on-campus server. This automated processing for the alert system targets two specific areas of concern to Union Pacific: first, it identifies overloading events caused by train, barge collision or seismic loads. This automated process sends an email alert to the bridge owner if certain strain thresholds are exceeded. Second, a critical eyebar component is monitored to determine load distribution between the parallel eyebar links and sends an alert if one or more eyebars exceeds a critical load amount or if the ratio of load distribution between the eyebars becomes abnormal (which causes accelerated fatigue). This alert system provides an insightful tool that not only automatically alerts bridge owners of areas

of concern that need further attention; it also provides a continuous set of data that the owner can use to inform decision-making when an alert does arise. The toolkit developed herein serves as a valuable asset to stakeholders and can be further developed to extend to additional components on the Harahan Bridge and beyond, to additional bridges.

CHAPTER 4

HEAT-TRANSFER BASED COMPUTED TOMOGRAPHY TECHNIQUES FOR DAMAGE DETECTION IN METALLIC STRUCTURES

The detection of damage in structures at its earliest stages has many economical and safety benefits. As previously presented, permanent monitoring systems using various forms of sensor networks and analysis methods are often employed to provide a more quantitative basis for asset decision-making. Local measurements can provide data specific to structural component behavior; for example, strain gages provide a measure of component strain (as is the case in the USCG RB-M vessel (*Chapter 2*)). While strain is a very valuable response parameter, it alone does not provide a direct measure of structural damage. A preferred approach is to utilize sensing methods that can provide greater spatial interrogation of the structure and that provide a more direct means of spatially depicting structural damage when it occurs. However, many of the available spatial sensing techniques can be costly and cannot be permanently deployed (e.g., IR camera thermography). For this reason, intricate analysis methods using permanently deployed sensors are being developed (e.g., ultrasonic piezoelectrics, sensing skins). An alternative approach is to leverage low-cost heaters and temperature sensors to develop an economical, permanently installable method of spatial damage detection using heat transfer. This

chapter presents an image reconstruction approach to local SHM similar to that of X-ray computed tomography (CT). However, the theories for X-ray CT must be adapted to properly represent heat transfer in structural components. The derivation of heat transfer computed tomography is discussed in this chapter including two methods for steering the effective heat front generated in a structural component. A high fidelity finite element method (FEM) model is used to verify the analytical derivation of individual steps within the method as well as to simulate the complete damage detection technique. Experimental results from both damaged and undamaged aluminum plate specimens are used to validate the FEM model and to justify theoretical assumptions. The simulation results are discussed along with possible improvements and modifications to the technique during future development.

4.1 Background

Permanently installed monitoring systems that have been developed for structures often consist of a network of single point sensors that measure global behavior (*e.g.*, accelerations) or highly localized behavior (*e.g.*, strain). As previously discussed, point measurements are often used as input to damage detection procedures that seek to identify damage existence, location, type and severity (Rytter 1993). As the field has learned, this is a very difficult inverse problem. In recognition of this fact, the field has begun to explore methods of more directly interrogating a structure spatially to identify damage. One popular approach to spatial interrogation of a structure for SHM is the use of ultrasonic guided waves (Cho and Lissenden 2012; Fei Yan et al. 2010; Giurgiutiu 2007; Rose 2004). Such methods are based on the use of piezoelectric elements (such as lead zirconate

titanate, or PZT) to launch elastic stress waves in a thin walled structure. These waves can propagate over long distances with damage introducing changes in the properties of structural wave propagation. Although ultrasonic techniques provide surface and subsurface damage detection across large distances, not all surfaces or material propagate sound well as others. Additionally, the refracted signals can make it difficult to detect anything beyond the first acoustic interference (Iyer et al. 2005). Another approach is to use structural sensing skins (Laflamme et al. 2012; Loh et al. 2009; Yao and Glisic 2015) which are conductive skins embedded in or coated on a structure; these skins' electrical properties change with underlying damage. This method typically uses electrical impedance tomography (EIT) techniques to reconstruct a spatial mapping of the conductivity of the embedded sensing skin based on boundary voltage or current measurements (Brown 2009). This diffusive (current flow is diffusive) method overcomes some of the limitations of the refractive (ultrasonic) method. However, it adds a level of complexity as the highly sophisticated skin (which is typically developed inside a laboratory) must either be integrated during construction or somehow embedded/coated in the field. There exists yet another method to spatially interrogate a structural component which utilizes the physics of heat transfer (diffusive), known as thermography (Roemer et al. 2013). This method employs the use of a laser, heat lamps or some form of heating a specimen and an infrared (IR) camera to record a structure's temperature response to the induced heat. The temperature recordings acquired by the IR camera are used to infer the damage state of the specimen either on or below the surface. Variations of this method are effective and accurate; however, they lack deployment robustness and are high cost (Maldague 2002; Schlichting et al. 2012). Therefore, in order for thermography-based

damage detection to be used in continuous monitoring, a permanently deployed and low-cost method needs to be developed. This dissertation has as its objective the development of such a local damage detection method.

This thesis explores a novel means of thermography as a permanent, cost effective and local sensing method for damage detection. Unlike traditional thermography that require expensive heat sources and cameras, the approach advocated herein is based on the use of low-cost resistive elements as controllable, discrete heat sources. These heat sources can transmit heat through a structural component via thermal conduction. Temperature sensors can also be used to observe structural temperature which will rise when heat transfers through a structure. A perimeter of heaters and temperature sensors is proposed to serve as a boundary for the introduction and observation of heat transfer within a defined interrogation zone. The location of structural damage (*e.g.*, fatigue cracks) can be identified by applying computational reconstructive techniques to the data obtained from the discrete heater-sensor setup on the boundary. There are sophisticated inversion techniques used to solve this boundary value problem that require the use of an iterative finite element method (FEM) model (Alifanov 1994). However, this thesis explores techniques that do not require model updating, thus increasing feasibility of an autonomous monitoring scheme. The method discussed in this chapter uses a computed tomography (CT) approach similar to X-ray CT scanning. In particular, it applies the Fourier interpolation (FI) and filtered backprojection (FBP) approaches which both utilize the Central Section Theorem in different manners (Aston 2008). Due to the permanent nature of the new method's installation, the heating-sensing elements cannot be rotated like the

X-ray transmitter-detector used in classical CT thus necessitating the development of a method to control (or "steer") the heat front across a structural component.

This chapter presents CT theory as applied to heat transfer in metallic structure. It also highlights an experimental setup used to test preliminary concepts and develop a high fidelity FEM model. The FEM model is used to generate synthetic datasets (with an undamaged case and multiple cases with varying damage states) to refine the method. Finally, the chapter presents the results of the proposed thermal CT algorithm applied to these datasets. The subsequent chapter, *Chapter 5*, presents complete thermal CT experimental results obtained autonomously using a wireless impedance analyzer developed therein.

4.2 Applying Computed Tomography Theory and Heat Transfer in Structures

The proposed technique for image reconstruction was derived from the fundamental principles guiding X-ray CT scans (Aston 2008). Conceptually, a CT scan is computed by taking multiple X-ray scans at given rotations around an object being imaged. The tube (transmitter)-detector coupled array physically rotates or spins around the object providing multiple pathways for the X-ray to propagate through the body being imaged. Based on the density of areas within the object, the X-ray intensity is attenuated at different levels. This results in a signal of the projection of the image with attributes only in the axis perpendicular to the projection (*i.e.*, no depth detail). Assumptions are often made that the X-rays are projected in a parallel plane without distortion along their path of propagation (Chen et al. 2005). This is in contrast to heat which propagates radially from a source and can diffuse laterally around a structural anomaly such as a crack.

Let it be assumed that an array of 32 heaters and 32 sensors is deployed to create a rectangular boundary on a structural component. The determination of the exact number of heater-sensor pairs and boundary around which they are located for a specific application is a function of cost (which obviously increases linearly as more heaters and sensors are used) and desired damage detection resolution. The 32 heater/32 temperature sensor set-up shown in Figure 4.1 illustrates the CT based technique with a circular anomaly arbitrarily placed within the body of interest to demonstrate the shadowing effect of each projection. Note, the convention of the projection angle, θ, which represents the angle of the plane of the heat wave propagating through the structure, or angle that the transducer arrays for an X-ray apparatus would be positioned at. The projection is actually travelling perpendicular to the projection angle. The lack of depth detail from a single projection can be observed in Figure 4.1 by examining the $\theta = 0°$ projection case and noting that if the location of the anomaly were to move up or down, the attributes depicted in the $\theta = 0°$ projection would be the same. Two methodologies to rotate the projected heat fronts are explained in more detail in the *Methods to Steer Heat Propagation* section of this chapter. For the derivation of the CT theory in this section it suffices to know that the heat front is being propagated across the specimen following a sequence of rotation angles.

The first procedure in reconstructing a CT image is assembling a *sinogram*. The sinogram is used to mathematically, as well as graphically, organize the temperature contrast data collected at every rotation angle. Figure 4.1 illustrates that as the heat propagation front reaches the anomaly, the heat transfer is impeded causing the front to develop a profile of damage as can be seen in the heat front on the other side of the anomaly. This profile is reflected in the measured temperature response. The contrast profile for the

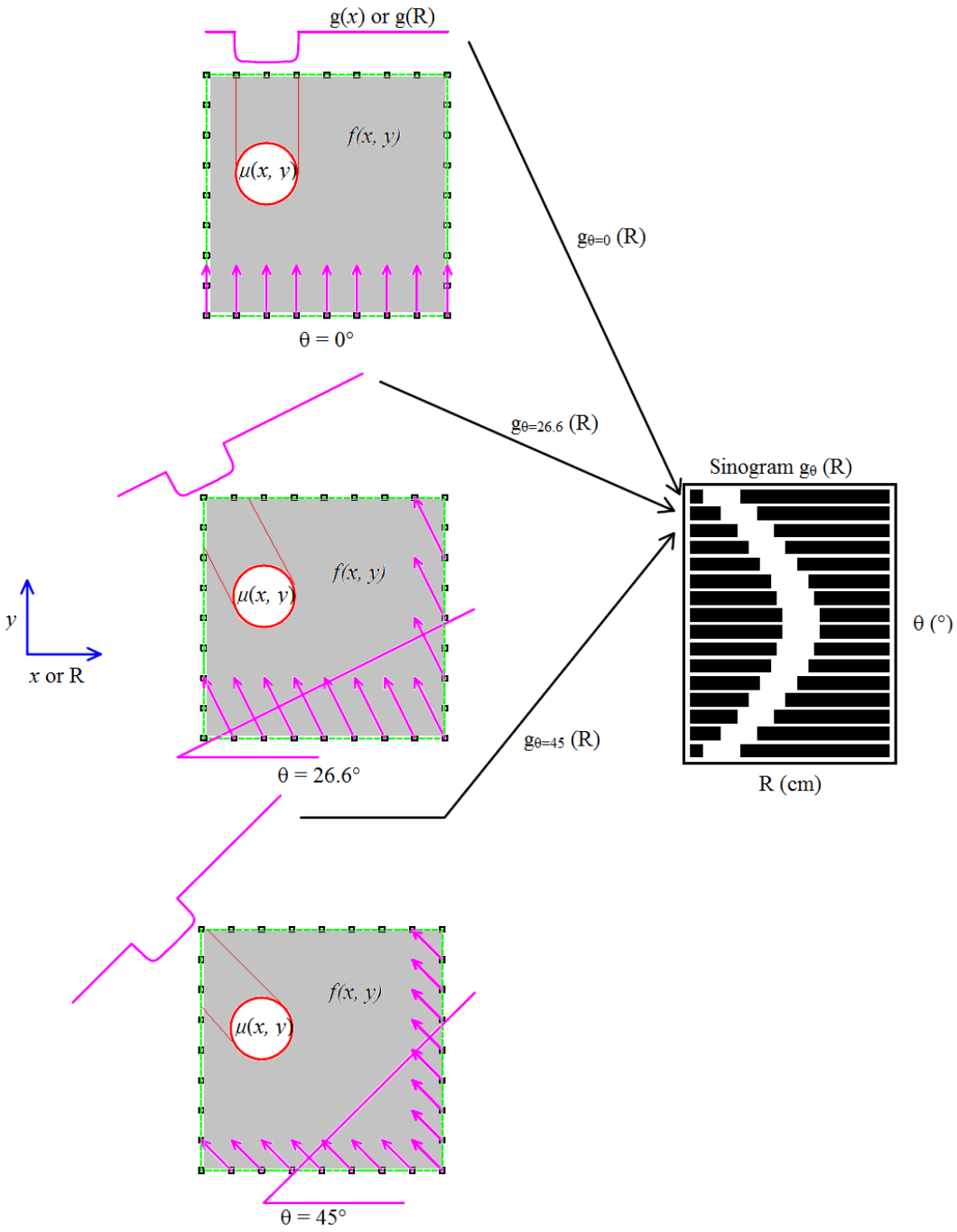

Figure 4.1 On the left, examples of rotating the heat propagation front by changing the heaters turned on and sensors being used to measure. Projection shadowing also shown for a circular anomaly in the specimen. The temperature contrast profile $g_\theta(R)$ represents the line integral of the impedance between each heater–sensor span. The right side illustrates the construction of a sinogram; each $g_\theta(R)$ is plotted in its corresponding "angle slot" going down the θ axis. As the projection rotates, the anomaly appears to shift based on its relative position to the new projection angle.

first rotation angle (θ = 0° in this example) is stored in the first row of the example sinogram shown on the right side of Figure 4.1. At every rotation angle, the temperature contrast profile is inserted into the corresponding row of the sinogram. To understand the mathematical importance of the sinogram, the methodology behind determining the temperature contrast profile for each row must first be understood.

Similar to IR thermography techniques, a temperature contrast must be determined which is relative to the undamaged state. This is done for each pixel in IR thermography but for the proposed CT approach it is collected in a profile spanning the lateral dimension of the heat front plane; temperature contrast along the front are then assembled in the sinogram. The temperature contrast is determined by comparing the temperature response of the structural component in a known (*i.e.*, undamaged) state to the temperature response of the component in an unknown (*i.e.*, damaged or undamaged) state. The change in temperature response is a function of the distance of the anomaly across which the heat propagation must travel (*e.g.*, anomaly width). This is assumed to have an exponentially decaying relationship,

$$T_d(x, t_1) = T_0(x, t_1)\, e^{-\int \mu(x,y)dy}, \tag{4.1}$$

where T_0 is the sensor temperature measurement at a given time, t_1, (relative to heater start time) for the undamaged specimen, T_d is the sensor temperature measurement at the same time for the unknown (damaged or undamaged) specimen, μ is a property of damage intensity (in this study μ is simply a relative comparison of undamaged versus damaged locations that is related to conductivity but doesn't have an absolute conductivity value), and x and y refer to the coordinates of the body being evaluated. Note, a rotating coordinate system is defined subsequently; however, this rotating system maps back to the original x

and y coordinates. The time, t_1, is determined separately for each sensor response and projection angle. The method used to calculate t_1 is different depending on the respective heat propagation steering method being used and will be discussed in more detail when those methods are introduced. Note, Equation (4.1) is for the case of $\theta = 0°$ where heat propagates along the y axis, additional angles are accounted for in the following equations. $T_d(x)$ is reduced proportionally to the integral of the damage across the projection path. Thus, if there is no damage, $\mu(x, y) = 0$ then clearly $T_d(x) = T_0(x)$. Note that the desired image is a spatial map of damage intensities; therefore $f(x, y)$ represents the entire imaged area of which the localized damage defined by $\mu(x, y)$ is included as a subspace. In order to give the image relative contrast to the undamaged state, a new function, g, is defined as:

$$g(x) = \ln\left(\frac{T_0(x,t_1)}{T_d(x,t_1)}\right) = \int \mu(x,y)dy = \int f(x,y)dy. \tag{4.2}$$

Equation (4.2) can also be written using the Dirac delta function

$$g(R) = \iint f(x,y)\delta(x-R)dxdy = \int f(R,y)dy, \tag{4.3}$$

where, $x = R$ defines the x location, or position perpendicular to the propagation direction, of a projection line along which the integration (over y) occurs as the delta function is non-zero at $x = R$.

Recall, temperature responses to multiple projection angles are required. Therefore, (4.3) can be applied to different projection angles with R representing the direction along the heat front plane and y representing the line over which the projection is being integrated. This can be viewed as if the original x and y coordinate system were rotating to ensure the heat wave propagates along y. This gives $g_\theta(R)$ as a profile of the damage collected at the projection angle, θ. This can be generalized as:

$$g_\theta(R) = \iint f(x,y)\delta(xcos\theta + ysin\theta - R)dxdy. \quad (4.4)$$

The collection of $g_\theta\ (R)$ projections can be organized to form the *Radon transform*, or sinogram, of the desired image *f*(*x*,*y*) as shown in Figure 4.1, with the abscissa representing *R*, the ordinate representing the angle, θ, at which the heat projection occurred, and the magnitude of the projection profiles, $g_\theta\ (R)$, being represented by pixel color. Recall from Figure 4.1 that for different rotations there are variations in the number of heater-sensor spans and their spacing. Therefore, 1D interpolation (along R) is implemented in order to have a discretized sinogram with consistent dimensions for each row.

There are various approaches to using the data contained in the sinogram to reconstruct the image of the structural component and any anomalies (in the *x*, *y* domain). Two common reconstruction techniques are direct Fourier interpolation (FI) and filtered back projection (FBP). However, in order to reconstruct the image into something with spatial significance, the *Central Section Theorem* (also termed the *Projection Theorem*) must be utilized (Aston 2008).

Theorem: The 1D Fourier transform (FT) of a projection $g_\theta(R)$ is the 2D FT of $f(R, \theta)$ evaluated at angle θ (Aston 2008).

Proof: (Xu 2013) Applying the definition of the Fourier transform to Equation (4.4)

$$G_\theta(\rho) = FT_{1D(R)}\{g_\theta(R)\} = \iiint f(x,y)\delta(xcos\theta + ysin\theta - R)\, e^{(-i2\pi\rho R)}dxdydR, \quad (4.5)$$

where $G_\theta(\rho)$ is the 1D FT of $g_\theta\ (R)$ and ρ is the abstract representation of *R* in the Fourier domain, which is also known as the "*k*-space." Substituting $x\,cos\theta + y\,sin\theta = R$ in order for the delta function to have a value of 1,

$$G_\theta(\rho) = \iint f(x,y)e^{-i2\pi\rho(x\cos\theta + y\sin\theta)}dxdy. \quad (4.6)$$

and then multiplying through by ρ

$$G_\theta(\rho) = \iint f(x,y)e^{-i2\pi(\rho\cos\theta\, x + \rho\sin\theta\, y)}dxdy. \quad (4.7)$$

Observe the 2D FT of the image, $f(x, y)$,

$$F(u,v) = \iint f(x,y)e^{-i2\pi(ux+vy)}dxdy, \quad (4.8)$$

where (u, v) is the Fourier representations of the coordinates (x, y) in *k*-space. Note that (u, v) correspond to $(\rho\cos\theta, \rho\sin\theta)$ in polar coordinates. Therefore,

$$G_\theta(\rho) = F(u,v)|_{u=\rho\cos\theta, y=\rho\sin\theta} \quad (4.9)$$

$$G_\theta(\rho) = F(\rho,\theta). \quad (4.10)$$

4.2.1 Direct Fourier Interpolation

Direct Fourier interpolation (FI), which as its name suggests, directly applies the Central Section Theorem to the sinogram data. This method reconstructs the 2D image $f(x, y)$ from the sinogram compilation of $g_\theta(R)$ by first applying the 1D FT sequentially to each $g_\theta(R)$ projection profile (*i.e.*, to each row of the sinogram):

$$FT_{1D(R)}\{g_\theta(R)\} = G_\theta(\rho) = F(\rho,\theta). \quad (4.11)$$

$F(\rho, \theta)$ is then mapped from polar to rectangular coordinates $F_\theta(u, v)$ using 2D interpolation. The final $F(u, v)$ is a summation of the $F_\theta(u, v)$ from all of the projection angles. Finally, the inverse 2D FT of the final $F(u, v)$ is taken to obtain the reconstructed image,

$$f(x,y) = FT_{2D}^{-1}\{F(u,v)\}. \quad (4.12)$$

4.2.2 Filtered Backprojection

To explain the theory behind *filtered backprojection (FBP)* it is worth first explaining backprojection without filtering. Backprojection is done by taking the projection (stored in the sinogram) and projecting it back across the entire parallel heater–sensor path (or plane). Referring to Figure 4.1, it would be like extending the shadow measured by a given temperature profile from one boundary to the other as portrayed in Figure 4.2. Doing this for all angles essentially stacks a number of images on top of each other increasing the contrast where the anomaly is located as is shown in Figure 4.2. Each backprojection, $b_\theta(x, y)$, for a given angle can be represented mathematically as

$$b_\theta(x,y) = \int g_\theta(R)\delta(xcos\theta + ysin\theta - R)dR, \tag{4.13}$$

which causes all (x, y) coordinates through which a given $g_\theta\ (R)$ projection passes through to take value of $g_\theta\,(R)$. Aggregating this procedure over all angles gives the backprojected image, f_b:

$$f_b(x,y) = \int b_\theta(x,y)d\theta = \iint g_\theta(R)\delta(xcos\theta + ysin\theta - R)dRd\theta. \tag{4.14}$$

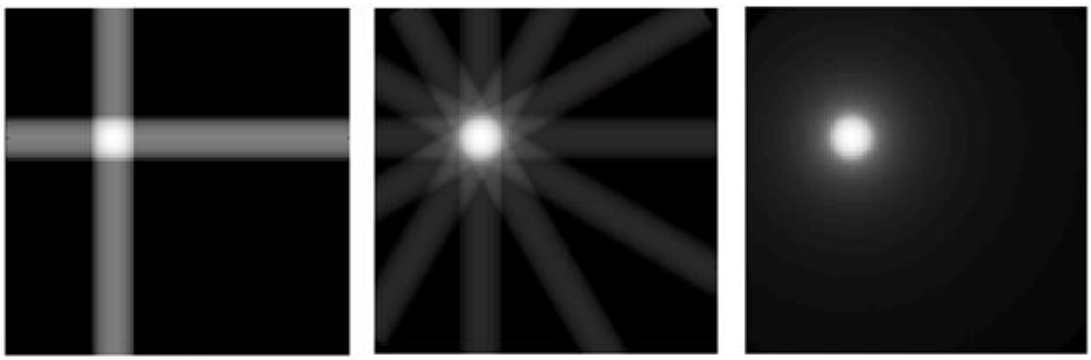

(a) (b) (c)

Figure 4.2 Illustration of backprojection technique and how additional rotation angles improve the damage detection accuracy: (a) 2 projections; (b) 6 projections; (c) many (204) projections.

Notice, the rings, or blurring, for the image in Figure 4.2c propagating out from what the actual anomaly would be. This is caused by the system's point spread function (PSF) and can be explained using the Central Section Theorem:

$$g_\theta(R) = FT^{-1}_{1D(\rho)}\{F(\rho,\theta)\} = \int F(\rho,\theta)e^{i2\pi\rho R}\, d\rho. \tag{4.15}$$

Substituting Equation (4.15) into (4.14) yields

$$f_b(x,y) = \iiint F(\rho,\theta)\, e^{i2\pi\rho R}\, \delta(x cos\theta + y sin\theta - R) dR d\theta d\rho. \tag{4.16}$$

Applying the properties of the delta function and substituting $x\ cos\theta + y\ sin\theta = R$

$$f_b(x,y) = \iint F(\rho,\theta)\ e^{i2\pi\rho(x cos\theta + y sin\theta)}\, d\theta d\rho, \tag{4.17}$$

which is nearly the 2D inverse FT of $F(\rho, \theta)$. All that is lacking is multiplying the integrand by ρ (*i.e.*, there needs to be $\rho\ d\rho\ d\theta$). Therefore, Equation (4.17) is multiplied by ρ/ρ

$$f_b(x,y) = \iint (F(\rho,\theta)/\rho)\, e^{i2\pi\rho(x cos\theta + y sin\theta)}\, \rho d\theta d\rho \tag{4.18}$$

$$f_b(x,y) = FT^{-1}_{2D}\left\{\frac{F(\rho,\theta)}{\rho}\right\} = f(x,y) ** FT^{-1}_{2D}\left\{\frac{1}{\rho}\right\} = f(x,y) ** \frac{1}{r}, \tag{4.19}$$

where, r is the sensor spacing (or interpolation point if a finer output grid than the sensor grid is being used) along R and ** denotes 2D convolution. Equation (4.19) states that the backprojected image is equal to the desired image convolved with $1/r$. Therefore, in order to reconstruct an accurate image, the backprojected image needs to be convolved with r. However, this can be carried out more efficiently in the Fourier domain. Thus, the steps to reconstruct the desired image are to calculate f_b from all of the backprojections as in Equation (4.14), then carry out the forward 2D FT on f_b to get $F(\rho, \theta)/\rho$ (apply 2D FT to both sides of (419)). Next, filter with ρ (multiply $F(\rho, \theta)/\rho$ by ρ) to get $F(\rho, \theta)$ and map to $F(u, v)$. Lastly, carry out the inverse 2D FT to get the desired image $f(x, y)$.

This same methodology can be used in FBP except the filter can be applied first to $g_\theta\ (R)$ to get $g'_\theta(R)$ then the backprojection is performed similarly as in Equation (4.14) except with the filtered $g'_\theta(R)$ (Xu 2013):

$$g'_\theta(R) = FT_{1D}^{-1}\{\rho\ FT\{g_\theta\ (R)\}\} \tag{4.20}$$

$$f(x,y) = \iint g'_\theta(R)\delta(xcos\theta + ysin\theta - R)dRd\theta. \tag{4.21}$$

Using FBP reduces the computational costs associated with backprojection. Backprojection-then-filter (BPF) requires a backprojection, 2D FT, multiplication by a filter, 2D interpolation and a 2D inverse FT, whereas Filter-then-backprojection, or filtered backprojection (FBP), requires only a 1D FT, multiplication by a filter, 1D inverse FT and backprojection. Keep in mind a 2D Fourier operations are more costly, in a computational sense, than 1D. While attaining these large computational advantages, FBP still produces the same reconstructed image as BPF.

Theorem. FBP image is equal to the BPF image.

Proof. The proof follows the procedure from (Xu 2013). Combining Equation (4.20) and (4.21)

$$f(x,y) = \iint FT_{1D}^{-1}\{\rho\ FT_{1D}\{g_\theta(R)\}\}\ \delta(xcos\theta + ysin\theta - R)dRd\theta. \tag{4.22}$$

Applying the Central Section Theorem

$$f(x,y) = \iint FT_{1D}^{-1}\{\rho\ F(\rho,\theta)\}\ \delta(xcos\theta + ysin\theta - R)dRd\theta. \tag{4.23}$$

Calculating 1D inverse FT

$$f(x,y) = \iiint\ \rho F(\rho,\theta)\exp(i2\pi\rho R)\ \delta(xcos\theta + ysin\theta - R)d\rho\ dR\ d\theta. \tag{4.24}$$

Substituting $x\ cos\theta + y\ sin\theta = R$ and executing delta function

$$f(x,y) = \iint\ F(\rho,\theta)e^{i2\pi\rho(xcos\theta+ysin\theta)}\rho\ d\rho\ d\theta. \tag{4.25}$$

Equation (4.25) is in the form of a 2D inverse FT

$$f(x,y) = FT_{2D}^{-1}\{F(\rho,\theta) = f(x,y), \tag{4.26}$$

4.2.3 Justification of Heat Transfer Application

In order to legitimately apply the CT framework to heat transfer, two assumptions are examined. The first being the relationship between the crack width and temperature response. The second being the parallel X-ray propagation versus heat's radial propagation and lateral diffusion around cracks. First, the temperature response is assumed to have an exponential decay relationship with the crack width (see Equation (4.1)). This is explored by instrumenting small aluminum dog bone specimens (6 inches (15.24 cm) x ¾ inches (1.91 cm) x ⅛ inch (0.318 cm) notched for stress concentration at mid-length) with a heater and sensor oppositely located on either side of the center span notches where cracking is engineered to occur (Figure 4.3). The instrumented specimens are placed in a load frame and the temperature response is recorded while the heater is actuated for the pre-load/undamaged state. After which, a cyclical load is applied until fatigue cracking begins; at which point another temperature response to heat actuation is recorded. Finally, after complete cracking occurs the temperature response to the heater being activated is recorded. The response to varying damage states, defined as crack width, is shown in Figure 4.4. These results show that there is indeed an exponential decay relationship. Thus allowing for the heat transfer CT theory to remain as previously proposed. However, due to the small sample size successfully collected for Figure 4.4, the effectiveness of the filtering properties that rely on this exponential decay relationship is examined closely in the reconstructed image results. As further validation, Figure 4.5 shows IR images of 3 damage states. Note, the responses plotted in Figure 4.4 and used to make the comparison

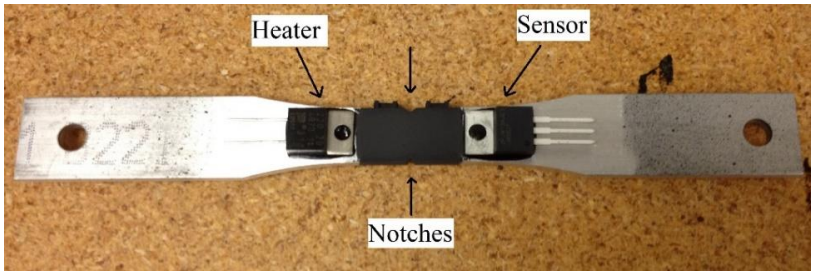

Figure 4.3 Aluminum dog bone specimens used to test temperature response's relationship to crack width. Specimens' temperature responses are recorded before and after fatigue cracking due to cyclic loading.

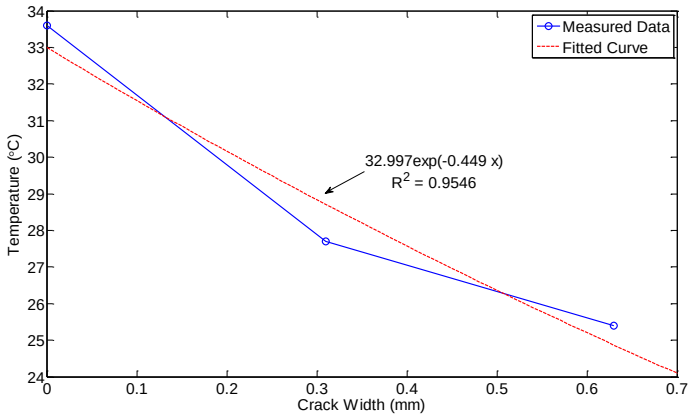

Figure 4.4 Temperature response recorded by solid state temperature sensor installed on specimen after 1 minute of heating.

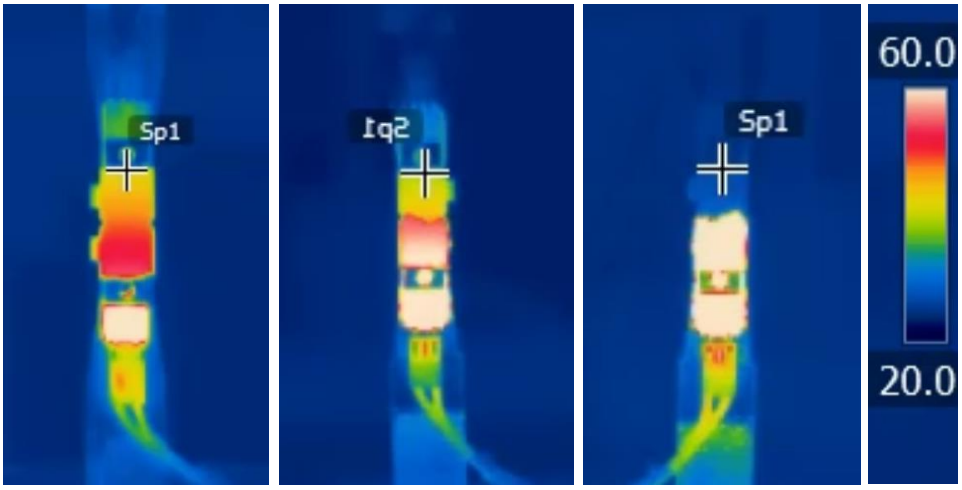

(a) (b) (c) (d)

Figure 4.5 IR images of specimens with varying damage states after 1 minute of heating: (a) is with no damage; (b) is with a crack across the specimen but no separation; (c) is of a crack with 0.31 mm gap; (d) shows the scaling in °C. Note, IR camera data is simply used as a qualitative validation and not used for the damage detection algorithm.

are those recorded using the installed IC temperature sensor, the IR camera is simply used as qualitative validation.

The next assumption tested is if the contrast in a temperature profile could be projected straight back across the image. This is tested by running a number of FEM simulations in ABAQUS (DS 2014) that include conduction, convection and radiation heat transfer physics to precisely simulate the temperature response. The simulations are of an aluminum (marine grade alloy 5086) plate with infinite dimensions in *x* and *y* (in order to eliminate the effects from the plate edge boundaries on heat transfer), and ¼ inch (6.4 mm) thickness. This is the same thickness and alloy type used in experiments that are presented subsequently. The simulations also include a heater and sensor with variable spacing from one another. The heater-sensor spacing varies from 0.79 to 26.77 inches (2 to 68 cm) in increments of 0.39 inches (1 cm), sensor-damage spacing varying from 0 to 25.98 inches (0 to 66 cm) in increments of 0.39 inches (1 cm) and damage crack length varying from 0.148 to 9.301 inches (0.375 to 23.625 cm) in increments of 0.148 inches (0.375 cm) (Figure 4.6). The data from the simulation results are organized into heater-sensor spacings and for each of these a plot is generated depicting what size and location of damage could have caused a given temperature contrast. Note, for visual comparison the temperature contrasts, dT_{norm}, are labeled in the classical form of:

$$dT_{norm} = \frac{T_0(t_1) - T_d(t_1)}{T_0(t_1)}, \tag{4.27}$$

where, t_1, is at some defined time. A plot depicting the size and distance from the sensor to a crack that could cause a specified temperature contrast is plotted for the heater-sensor spacing of 18.9 inches (48 cm) and is shown in Figure 4.7. Note, this is done for all possible heater-sensor spacings.

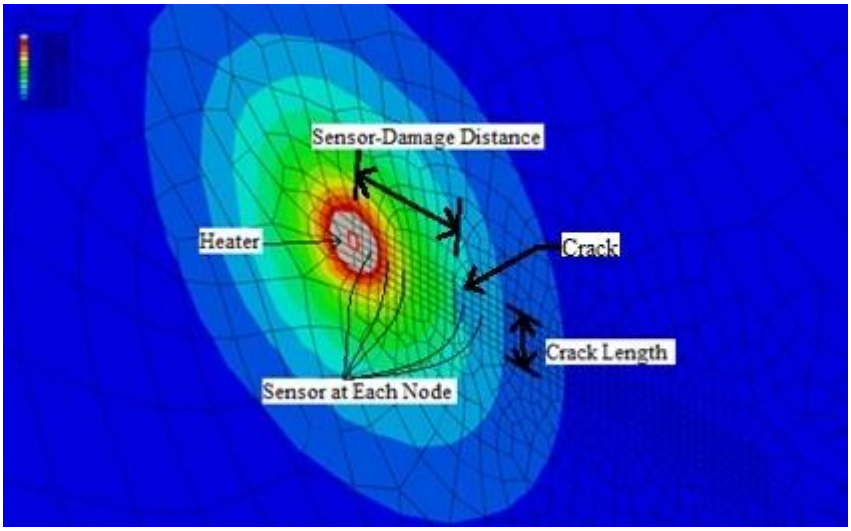

Figure 4.6 Isometric illustration of the FEM model and the parameters that were varied in order to carry out the study of the damage parameters' effect on temperature contrast.

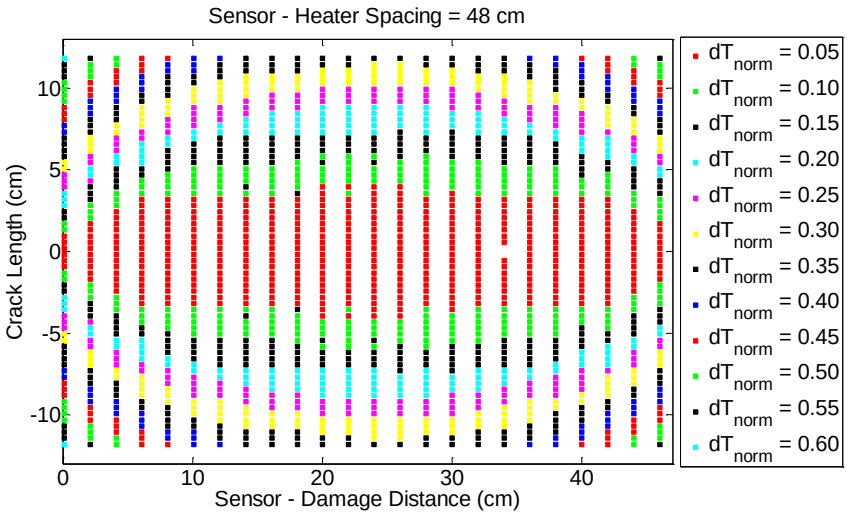

Figure 4.7 Simulation results for heater-sensor spacing of 18.9 inches (48 cm) showing the collection of damage parameters that could cause a given temperature contrast to occur.

The data from these simulations serves as a library to access during reconstruction. For each parallel projection of a given rotation angle (keep in mind there are multiple projections per rotation, refer to Figure 4.1) a geometry of possible crack parameters is queried using the heater-sensor spacing and the measured temperature contrast. This

geometry is then projected onto the reconstructed image at the correct rotation angle and longitudinal and lateral spacing. The calculated geometry for every parallel projection of each rotation is stacked onto the image, imitating the backprojection process, an illustration of this approach is shown in Figure 4.8. This has the potential to improve reconstruction accuracy because standard backprojection theory assumes that the only possible damage/anomaly scenarios to cause damage are perfectly rectangular backprojections (Aston 2008), which is not the case for heat transfer. The image is then filtered using FBP techniques which is permissible because the contrast is defined in the correct manner. However, these results showed no improvement from the traditional FBP method (which will be presented subsequently). This can be explained by examining the plots for all of the heater-sensor spacings, which are very similar to the plot in Figure 4.7. It can be seen that the geometry is nearly a rectangle like what is backprojected in the traditional technique that assumes parallel backprojections. The only major difference being the slight tapering near the heater and sensor on either side. Nevertheless, the thermal CT

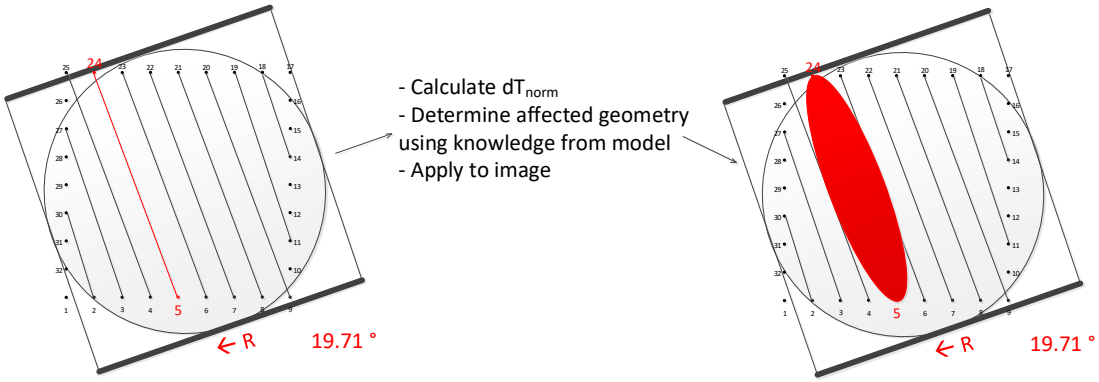

Figure 4.8 Illustration of geometric projection. Using the example of heater 5 and sensor 24, after the temperature contrast (between the damaged and undamaged temperature response) is calculated, rather than backproject a perfectly parallel rectangle (as is shown in Figure 4.2) the geometry of potential crack location and sizes that could cause such a temperature contrast is projected on the reconstructed image. This is done for every heater-sensor combination for each resepctive rotation angle and the images stacked on each other similar to that shown in Figure 4.2c.

reconstructed techniques derived herein are carried out using both the library of geometric backprojections and the traditional parallel backprojections (as will be shown subsequently) resulting in reconstructed images that are essentially identical. Therefore, attempting to include geometries of damage parameters (rather than the assumption of parallel heat propagation) only adds to the complexity of the technique and does not provide any improvements to the reconstructed image. Thus, the parallel projection assumption is used for the proposed thermal CT technique.

In theory, only 180° of rotation are required to obtain projections sufficient to reconstruct the entire image of a structural component. Nevertheless, the entire 360° of rotation are performed in order to make up for the radial propagation of heat diffusing around anomalies or damage in a structural component. That is, heat begins to return back to the area located behind the damage the further the distance from the damage on the opposite side of the heat source as will be illustrated in the experimental results following this section. If the damage is just a small distance in front of the heater, then the temperature sensor on the opposite perimeter of the structural component being interrogated does not experience an appreciable difference in temperature response. This is due to the heat diffusing around the damage with the damage's influence on the heat propagation decreasing the further the heat front moves away from the damage. Alternatively, if the damage is close to the temperature sensor then the damage's effect (or shadow) on the temperature caused by the heat front is preserved. Therefore, if damage goes undetected, or its temperature response is not affected greatly due to lateral diffusion during one projection, a projection coming from the opposite side (180° offset) will detect the damage, or be affected less by the lateral diffusion.

4.3 Experimental Setup

Two experimental structural components (one undamaged and one damaged) are used to develop the point-based low-cost heating-sensing approach, test preliminary concepts and calibrate a high fidelity finite element model. The testing specimens are ¼ inches (6.4 mm) thick aluminum (marine grade alloy 5086) plate elements that are 2 feet (61 cm) wide and 4 feet 1 inch (124.5 cm) long. The specimens are instrumented with 32 temperature sensors collocated with 32 heaters (the mid-points of the heater and temperature sensors are 0.39 inches (1 cm) apart from each other) as seen in Figure 4.9. One specimen is left undamaged and the other has a 4.29 inch (10.89 cm) long, 0.079 inch (2 mm) thick 45° angle (rotation measured from long edge of plate) crack induced near a welded stiffener as this is a location of potential fatigue cracking in ship hull structures. The area of the sensor setup is smaller than the plate specimen and is 18.9 inches by 18.9 inches (48 cm by 48 cm) in area. Along the perimeter of this square interrogation zone,

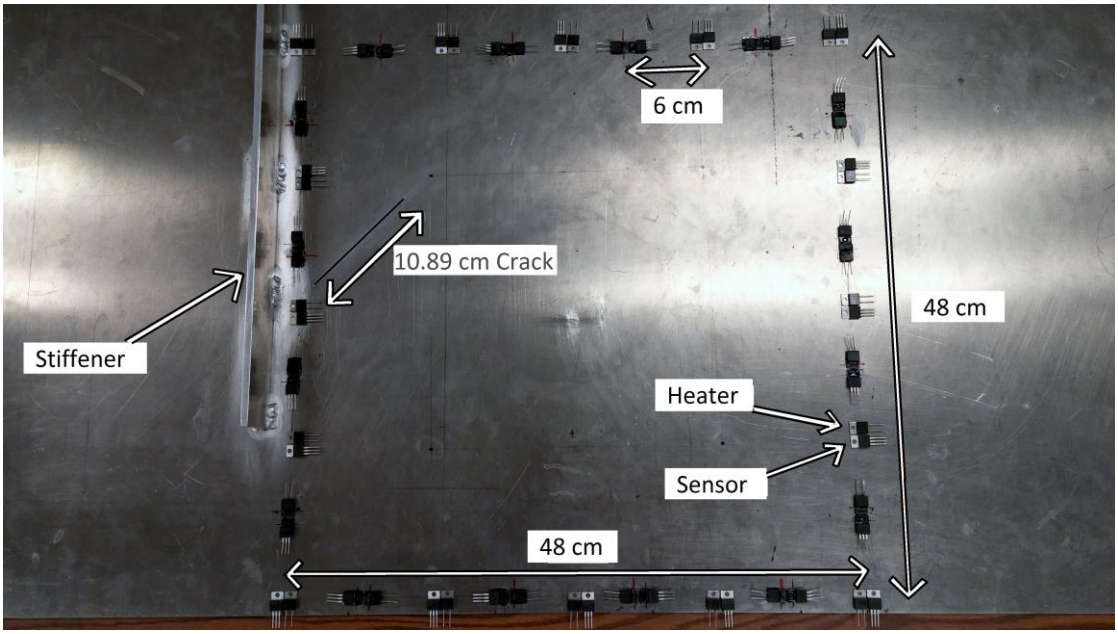

Figure 4.9 Experimental setup of damaged aluminum specimen.

the temperature sensors are located equidistant from one another; this leads to a 2.36 inches (6 cm) spacing between sensors.

The temperature sensors are solid state integrated circuits (Texas Instruments LM5DT) that linearize the response of the internal thermistor; these sensors have a -55℃ to 150℃ operating range with an accuracy of 0.25℃ when operating near room temperature and a sensitivity (or precision) of 10 mV/℃ (TI 2000). When using the 16-bit ADC on the *Narada* sensing unit and applying unity gain to the filtering board, the resolution of the data collected is 0.0076℃. The heaters are resistors with a specified resistance of 5.6 Ω, power rating of 20 W and with an exposed metal element (Bourns PWR220T-20-5R60F) for heat dissipation (Bourns 2011). The temperature sensor voltage output is first filtered and then recorded by the one of four analog-to-digital converter (ADC) channels on the *Narada* wireless sensing node. This setup necessitates the use of 8 *Narada* nodes (8 x 4 = 32 channels). The heater(s) to be activated are connected to a power supply and are triggered by a *Narada* digital-to-analog converter (DAC) channel. Depending on the heat steering approach, as will be explained subsequently, different heaters are turned on at different times for multiple data collection segments. Note that the *Narada* DAC does not drive the heater output but triggers the heater to begin receiving power from the attached power supply, thus ensuring time synchronization between heaters and sensors.

Basic heat transfer dictates that in a homogeneous material, two points equidistant from a heat source will have the same temperature response. However, introducing an anomaly or crack between the heat source and one of these points (essentially shielding that point) causes its temperature to increase at a slower rate than that of the other point. In other words, a crack between the heater and sensor causes a sensor's temperature

response to be lessened. This chapter has already shown this phenomenon in Figures 4.4 and 4.5; similarly, the full-scale experiment shows this same phenomenon as seen in Figures 4.10 and 4.11. Figure 4.10 shows the time-series temperature response of four sensors during one of the experimental tests in which the bottom heater at the mid-point left-to-right (heater 13) is activated and producing 14.5 W of heat energy (9 V, 1.61 A, 5.6 Ω) for a duration of 2000 seconds (33 minutes 20 seconds). It can be seen that not only does sensor 4 have a lower temperature response than does sensor 22 (which is equidistant to the heater) but sensor 5 has a greater temperature rise than does its equidistant counterpart (sensor 21) because the heat shielded or "trapped" on the heater side of the crack increases the heat supplied to sensor 5. The heat transfer being affected by the crack in the damaged specimen is shown using an IR image in Figure 4.11. Note, that the IR camera is used only to fine tune the FEM model and garner insight into heat transfer physics in structural components and is not used in the thermal CT damage detection approach.

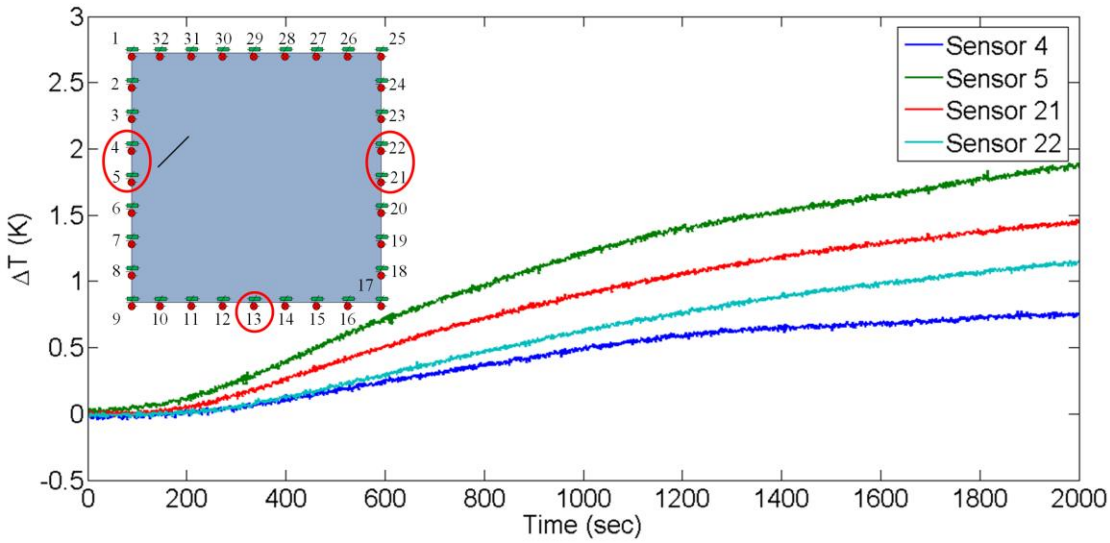

Figure 4.10 Temperature response of four temperature sensors (sensors 4, 5, 21 and 22) to heater 13 being activated at 14.5 W for 2000 seconds with a crack near sensors 4 and 5.

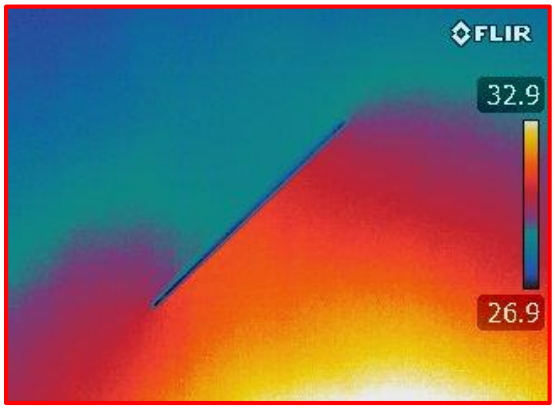

Figure 4.11 IR image of heat transfer affected by crack in damaged structural component (Note, the IR camera is not used for the thermal CT algorithm, just to visualize concepts).

The experimental setup's ability to successfully supply heat and record temperature responses with enough sensitivity to observe the effects of damage validates the utilization of the proposed permanently installable point-based heater-sensor setup for use in thermal CT image reconstruction (damage detection). The data from the experimental tests also serves the purpose of calibrating a high fidelity FEM model created in ABAQUS. The strategy adopted in this study for damage detection is based on conductivity with crack damage assumed to alter the heat conductivity of the plate in the vicinity of the damage. Although heat conduction is the key damage-sensitive feature, the role of the other model parameters (*i.e.*, convection, radiation, surface-to-surface conduction between plate and sensor as well as between plate and heater) must be investigated and included in the model in order to understand the sensitivity of the specimen and instrumentation being used as well as increase the accuracy of the model. For instance, Figure 4.10 shows that once the heat front reaches the sensors (or location on the structural component) the initial rise in temperature occurs at a greater rate as time continues. In fact, the temperature rise begins to saturate (as can be seen in Figure 4.10) and eventually reaches steady-state when the

heat input via conduction is equal to the heat loss via convection and radiation. If conduction alone were considered, the structural component would continue increasing in temperature infinitely. Additionally, the complex boundary conditions of the plate, such as the stiffener on one side of the sensor perimeter and the other sides of the sensor perimeter all being located at different distances from the plate boundary, need to be accurately modeled. The temperature response of both the damaged and undamaged specimens to various heat inputs are used to calibrate the FEM model.

After the FEM model is calibrated, it is used to simulate datasets to be used in the proposed reconstruction techniques. Synthetic datasets are used in this chapter to investigate multiple sensor setups, heating sequences and damage events. Because the FEM model is very accurate, many heat steering approaches (two of which will be discussed in the following section) can be tested, and many damage scenarios to test the resolution of the proposed reconstruction techniques can be tested at a much quicker rate (the FEM model can simulate 30 minute heating and 30 minute cooling in a matter of seconds). Therefore, time consuming experimental work is saved until a final and accurate method is determined (the complete experimental work for the said method being presented in the following chapter).

4.4 Methods to Steer Heat Propagation

4.4.1 Phased Array Steering

One method to overcome the obstacle of stationary heaters and sensors is to use a phased array actuation. Phased array refers to an array, or set, of transducers (or a single transducer with multiple elements) that are not all actuated at the same time but have a

phase, or time-step, between their actuation start times, or for AC signals, the peak of the excitation wave signal. This type of approach is used to control the location at which physical phenomena being propagated (*e.g.*, an ultrasonic mechanical wave) from multiple actuators are constructively added (the focal point) or deconstructively added (all other points). In essence, the wave front can be steered. This has been a method of practice for ultrasonics (Drinkwater and Wilcox 2006), electrooptical (McManamon et al. 2009) and radio frequency (communication not sensing) (Mailoux 2005) techniques. A key difference between these methods and the heat transfer method derived in this chapter is that the temperature response to heat from one heater cannot simply be superimposed with the temperature response of another heater(s). Therefore, exact steering is not possible; nevertheless, an approximate propagation front at a given angle can be achieved, as will be described.

Data collection begins by projecting a heat front from one side of the boundary to the other by turning on a set of heaters each actuated at given time delays. The temperature response is then recorded at a select set of sensors on the opposite side directly across from the active heaters resulting in an effective projection angle. For example, beginning with a projection angle, $\theta = 0°$, as shown in the upper left corner of Figure 4.1, all 8 of the heaters on the bottom edge are turned on simultaneously and the response measured at the 8 sensors on the top edge. After these data have been collected and the specimen cools, the array of activated heaters is shifted in order to have a projection angle of 26.6°, also shown in Figure 4.1. For this scenario the heaters have a time delay in order to achieve the desired angle. That is, heaters with a shorter distance to travel are actuated later than those with a greater distance to travel. The heaters are turned off and the specimen once again cools; this

continues until θ has been rotated the full 360° with temperatures recorded for each rotation. For this method, a total of 16 propagation angles are utilized. Because heat is a diffusive process any more than 16 propagation angles results in insufficient distinction between angles and does not increase the resolution of the reconstruction algorithm. This is a function of the interrogation area (18.9 inches by 18.9 inches (48 cm by 48 cm)) and that only 32 heater-sensor pairs are used. The exact time delays required to achieve the desired propagation angle are determined iteratively with the FEM model. Notice, the heat does not propagate in a constant rigid angle, but rather has a radial propagation from each heater. At a given point in time the combination of all heat sources (and corresponding temperature rise) result in effective propagation angle. To illustrate, Figure 4.12 shows an IR image of a heat front as it propagates at a 45° angle.

The temperature data from more than just a single time stamp is required to construct the temperature contrast profile. Meaning, the time, t_1, used in Equations (4.1) and (4.2), is different for each heater-sensor pair of a given projection angle. This can be seen conceptually by examining the heat front in Figure 4.12. The change in temperature to 30℃ has not yet reached the sensors in the far, top right, corner; whereas it has already passed the sensors located at the top left and bottom right of the array. Therefore, a time

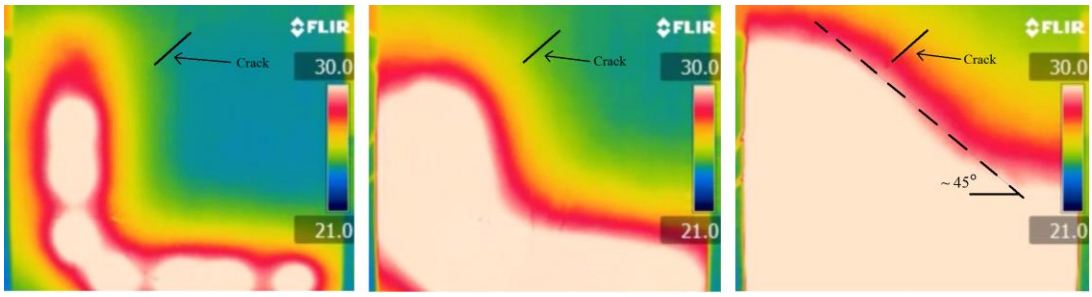

Figure 4.12 IR image of heat propagation being steered at 45°, units are °C. Note, IR information not used for damage detection algorithm. Images are snapshots in time from earliest to latest, left to right.

delay must be applied in the post-processing of the data in order to compare the temperature response at times when the temperature is the same across all sensors for the undamaged specimen. The combination of the heater activation and sensor read-out delays mitigates the effect of the slight curvature seen in the heat front. Due to the complex nature of the boundaries (*e.g.*, a stiffener on one side of the interrogation zone) of the specimen and the fact that superposition doesn't hold true with multiple heat sources, the FEM model is used to determine the exact time delays for the heater activation and sensor read-out to achieve the desired heat propagation angles.

4.4.2 Sequential Single Source

In order to have better control of the rotation angles this method uses only a single heat source at a time. This may reduce the complexity associated with the phased array approach. This increased control helps better maintain the thermal CT theoretical framework as well as allow for additional rotation angles, which adds to image reconstruction resolution. The procedure is to actuate a single heater and record the temperature response at every sensor location. After the structure cools, the next heater is then actuated and the temperature response recorded at every sensor location once again; this carries on until data has been collected for all individual heaters. After all of the data is collected it is then post-processed in order to be organized correctly into the sinogram. As the heat propagates radially from a single heater, the path between a given heater and sensor can be analyzed as a 1D problem. Therefore, each heater has a number of pairings, each acting as a 1D problem. Note, a large damage event would indeed effect multiple 1D paths but doesn't change the framework of the problem as it would simply cause a backprojection of damage across multiple paths. The data is organized by setting forth a

virtual apparatus that rotates around a virtual circle as shown in each of the 9 images comprising Figure 4.13. This virtual apparatus is indeed larger than the 18.9 inch x 18.9 inch (48 cm x 48 cm) instrumented area due to the fact that as the rotation angle increases from 0°, the lateral dimension increases. For instance, the 45° angle has data reaching from the 2-32 heater-sensor path to the 16-18 path, thus spanning 23.6 inches (60 cm); therefore, the apparatus has a virtual radius of 23.6 inches (60 cm). The response at each sensor for

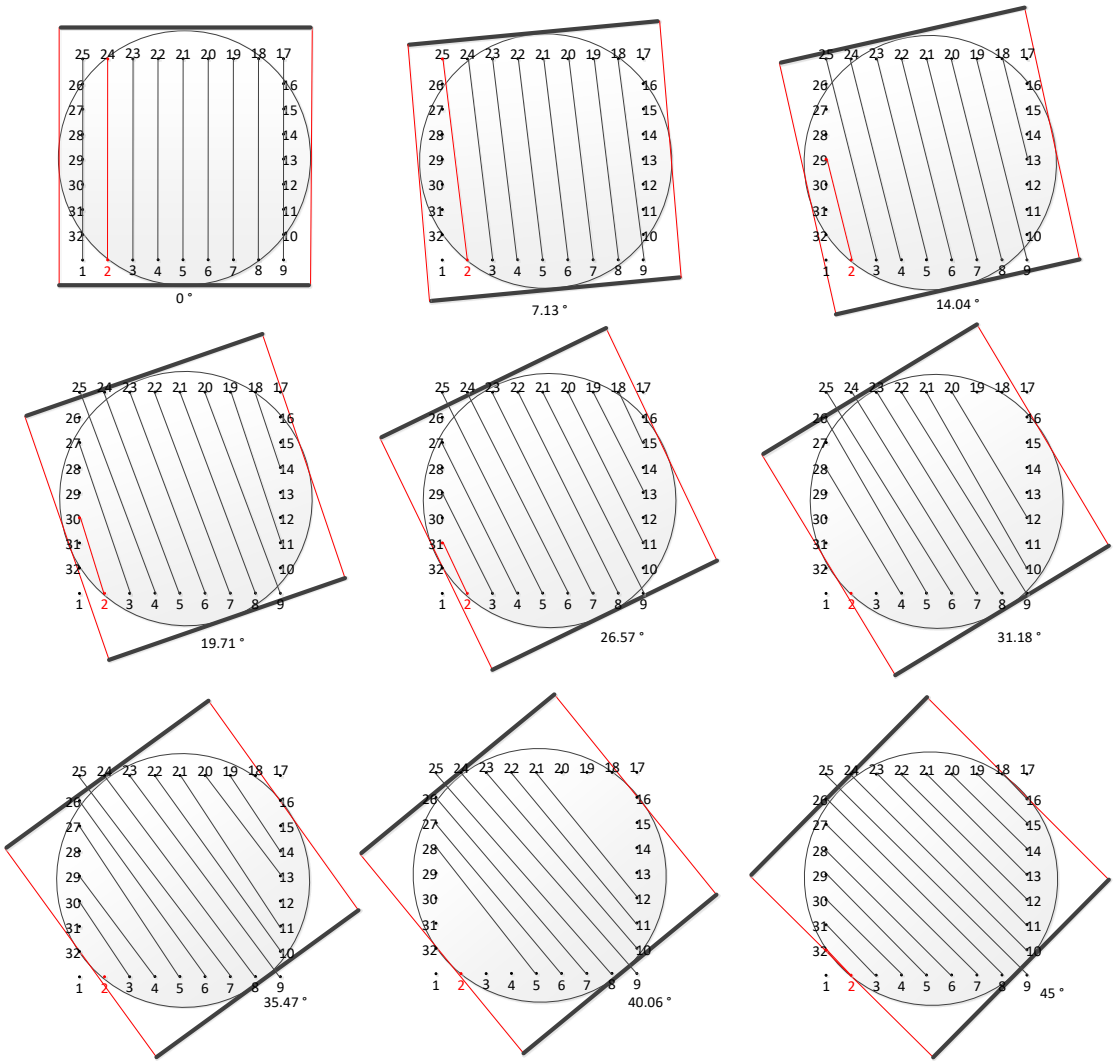

Figure 4.13 Illustration of 9 heat propagation angles using the sequential single source steering method, the thick solid black parallel lines represent the "virtual" apparatus.

the given heater is organized by the angle (finely discretized) between the heater-sensor and the lateral location that the heater-sensor path would project to on the virtual apparatus. Figure 4.13 highlights heater 2 for the 9 angles shown. For instance, the response of sensor 24 to heater 2 belongs to the 0° rotation angle row of the sinogram and the response of sensor 25 to heater 2 belongs to the 7.13° row of the sinogram. Notice, for some angles such as 31.18° and 40.06° the corner of the specimen lacks a heater-sensor path. However, due to the greater accuracy of the shorter paths when the corners are interrogated and because much of the image from the virtual apparatus is cropped back to 18.9 inch x 18.9 inch (48 cm x 48 cm), the overall image quality remains consistent at the corners. The total number of rotation angles for this method is 64 when using 32 heater-sensor locations equally distributed around a square boundary. The time, t_1, at which to calculate temperature contrast in Equation (4.1) is taken as the time at which the contrast is greatest for a given heater-sensor pair. In other words, the maximum temperature contrast for each heater-sensor pair is used. The determination of t_1 is highlighted in Figure 4.14.

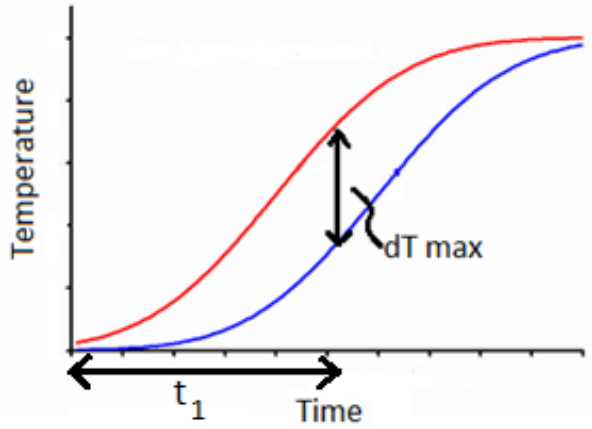

Figure 4.14 Illustration of the determination of temperature constrast (and time, t_1, at which to determine the temperature consrast).

4.4.3 Temperature Profile Assembly

For both the phased array and sequential single source the temperature sensor spacing along *R* (the *x*-axis of the rotated coordinate system, perpendicular to the direction of the heat front propagation, recall Equation (4.4) and Figure 4.1) is inconsistent between varying rotation angles. Therefore, after the temperature contrast profile for a given propagation angle is recorded (see Figure 4.1) using the exact temperature sensor locations, the profile is then interpolated in order to have data points at a precise and consistent spacing of 0.79 inches (2 cm) along the *R*-axis. That is, the sinogram abscissa has consistent spacing for each rotation angle. Doing so allows for the thermal CT theory (and mathematics) to be properly executed. This interpolation method does not, however, increase the point-based imaging method's ability to detect a small (relative to sensor spacing) anomaly or damage if it were to occur in close proximity to the sensor perimeter edges but between two of the sensors. This damage scenario's effect on the temperature profile would go undetected for certain propagation rotation angles with or without using the described interpolation method. Nevertheless, this is a shortcoming of all CT methods (including X-ray, the only difference is X-ray CT uses many more emitters and sensors which are more finely spaced) and is simply an input to the sensitivity function of the damage detection approach. More specifically, small damages near the perimeter of the sensor setup may not be detected as confidently as in the center of the interrogation zone. A simple method to overcome this would be to increase the number of heater-sensor pairs while understanding the trade-off that doing so increases the installation cost of the sensing technique. As discussed earlier, the number of heater-sensor pairs and their spacing can be determined by balancing cost and desired resolution.

4.5 Results

Synthetic datasets are generated by simulating responses of the undamaged plate and the plate with a 4.29 inch (10.89 cm) long, 0.079 inch (2 mm) thick crack located within the sensor interrogation zone. Datasets for the undamaged and damaged plate are simulated for both the phased array and sequential single source steering methods. These datasets consist of temperature readings at the 32 sensor locations for the specified heating scenarios. Sinograms for each method are constructed as described above and are shown in Figure 4.15. The sinogram for the sequential single source steering method contains much more information because it is constructed using 64 rotation angles as compared to just 16 with the phased array method. The direct Fourier interpolation reconstruction technique is applied to the data contained in each respective sinogram, the results from this technique are displayed in Figure 4.16 with the location of the actual damage being superimposed on the image for comparison. Only the sequential single source shows reasonable results as the phased array has insufficient rotation angles to allow for the mapping from polar to Cartesian coordinates in the Fourier domain to be accurate. The slight inaccuracies included in the sequential source method are because Fourier interpolation is more useful in edge detection and the features of the crack are smaller than

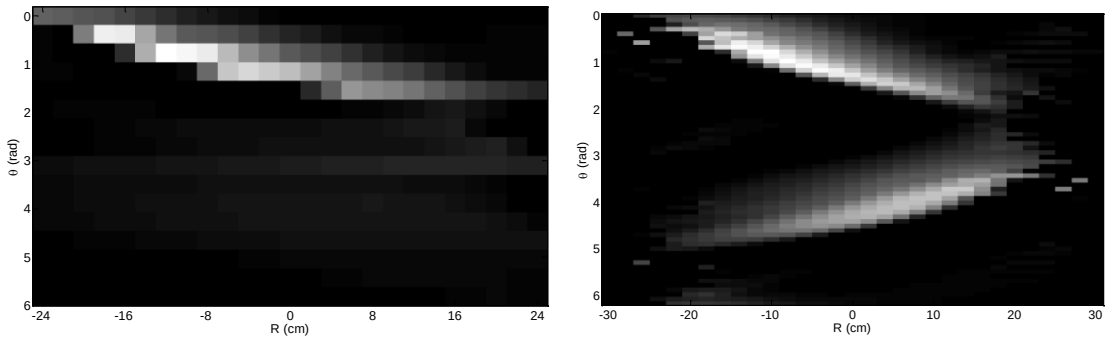

(a) (b)

Figure 4.15 Sinogram: (a) phased array steering; (b) sequential single source.

the current grid spacing/resolution. The reconstructed images for the backprojection (without filtering) method are shown in Figure 4.17. Note, the *x* and *y* limits for Figure 4.17b are -11.8 inches to +11.8 inches (-30 to +30 cm), whereas in Figure 4.17a they are -9.4 inches to +9.4 inches (-24 cm to 24 cm). This is to show the entire image attained from the virtual apparatus discussed earlier (Figure 4.13), including those locations beyond the boundary of the interrogation zone. The backprojected image for both methods are similar. This is because the damage is large enough that it can be identified even by a small amount of rotation angles. However, the filtered backprojected images show the benefit of additional rotation angles as can be seen in Figure 4.18; notice that the image for the sequential single source has been cropped back to the instrumented area of the specimen. The shadowing effect of the rotation angles can be seen in Figure 4.18a. Whereas, in Figure 4.18b the additional rotation angles help to eliminate the shadowing effects.

4.6 Chapter Summary

Damage detection techniques using heat transfer (thermal) computed tomography (CT) are applied to a novel point-based thermal measurement setup. The key attributes of this setup being its low-cost and ability to be permanently installed for monitoring applications while at the same time providing a two-dimensional (2D) spatial image of the state (or potential damage) of a structural component. Another advantage to this technique is its ability to reconstruct the 2D image without the use of iterative inverse solutions that require model updating (the FEM model used in this chapter is only used to develop the sensing and reconstruction approach but is not required for actual image reconstruction). The theory used to apply computed tomography reconstruction techniques to heat transfer

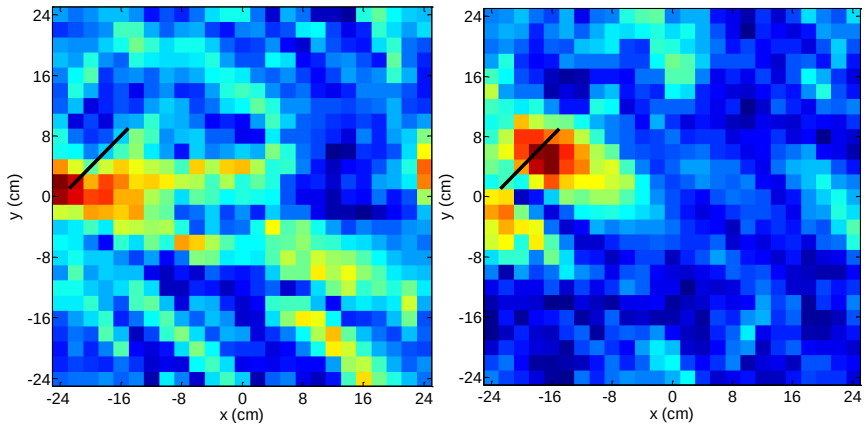

(a) (b)

Figure 4.16 Fourier interpolation (FI): (a) phased array steering; (b) sequential single source. Note, solid black line superimposed to represent crack location.

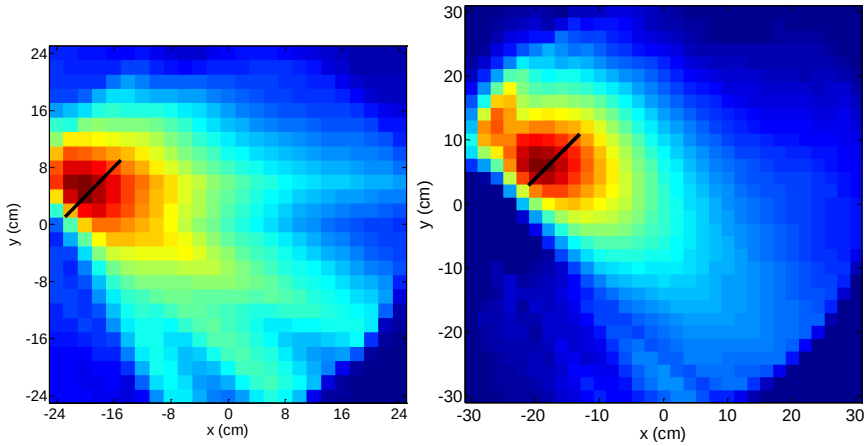

(a) (b)

Figure 4.17 Simple backprojection: (a) phased array steering; (b) sequential single source, uncropped (recall circular image resultant of virtual apparatus). Note, solid black line superimposed to represent crack location.

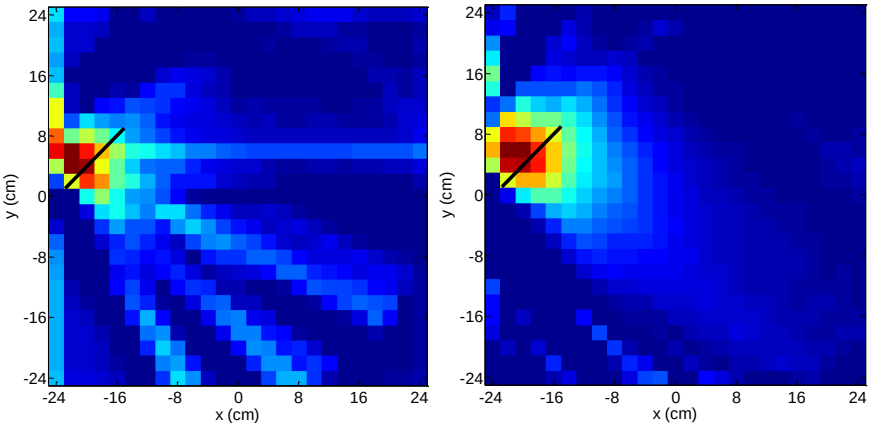

(a) (b)

Figure 4.18 Filtered backprojection: (a) phased array steering; (b) sequential single source, cropped. Note, solid black line superimposed to represent crack location.

is discussed. An experimental setup is used to justify the application of thermal CT theory to the image reconstruction technique, explore preliminary concepts and installation procedures, and to calibrate an FEM model. Two methods for steering a propagating heat front across a structural component using the stationary heater-sensor setup are derived; namely phased array steering and sequential single source. Both of these methods are used to assemble respective sinograms based on simulated results of an unknown (damaged) specimen compared to a known (undamaged) specimen. These sinograms are used to reconstruct images using Fourier interpolation (FI), backprojection and filtered backprojection (FBP). The filtered backprojection exhibits the best results, which provide very good resolution considering the area being monitored (18.9 inches x 18.9 inches (48 cm x 48 cm)) and the fact that only 32 heater-sensor locations are used. Among the 2 steering methods, the sequential single source method yields better results because it provides more rotation angles than does the phased array method (64 rotation angles versus 16). In conclusion, the thermal CT, point-based method using filtered backprojection (FBP) with sequential single source heat propagation is proven through simulations to provide sufficient resolution for use in spatial imaging/damage detection. The next chapter develops a multi-channel wireless device that among other capabilities, enables the autonomous heat actuation and data collection of complete thermal CT experiments. One such experiment is presented in *Chapter 5*.

Future work may include examining the possibility of beginning the heater actuation of one heater before the specimen has entirely cooled down from the previous heater in order to reduce the total time required for each data collection sequence. If the same sequence is followed every time the specimen is interrogated, accurate image

reconstruction with a shorter time-span for each test may be possible. However, a potential complication to this is the larger amount of energy required to raise the temperature of the specimen further above room temperature. As the difference between the temperature of the structural component and the ambient temperature becomes greater, convection and radiation have a larger effect and may cool the component at the same rate the added heat is attempting to raise the temperature. Recall in Figure 4.10 that the temperature of the structural component begins to saturate and after a given amount of time would reach a steady-state equilibrium where the heat provided through conduction is equal to the heat that escapes through convection and radiation. Another area for future work is including the effect of a changing ambient temperature outside of the controlled laboratory environment. This, once again, would have an effect on the convection and radiation response of the component being monitored. A proposed approach that could be examined is collecting the baseline (known/undamaged) image, or dataset, at multiple ambient temperatures. Then when the unknown dataset is collected, the ambient temperature at that time is used to determine which baseline dataset to use in calculating temperature contrast between the data from the unknown and known damage states. Lastly, different geometries for the heater-sensor perimeter can be explored. A circular perimeter would provide a completely uniform virtual apparatus and allow for a straightforward determination of projection angles.

CHAPTER 5

DEVELOPMENT OF A MULTI-PURPOSE WIRELSS IMPEDANCE ANALYZER

The preceding chapters have been predicated on the benefits of an effective structural health monitoring (SHM) system. To be effective, such a system should provide both global and local data about a structure that can be used to quantitatively drive the decision-making process. Additionally, the efficacy (or ability for the benefits to outweigh the costs) increases with the implementation of a wireless SHM system as opposed to a wired system. *Chapters 2* and *3* present field deployments of wireless SHM systems that supply data-driven analytical frameworks using both global and local information about the respective structures on which they are installed. Nevertheless, the need to obtain more localized and spatial data about a structure is highlighted and a solution developed in *Chapter 4*. However, the proposed spatial sensing solution (as well as others being developed in the community) possesses the robustness to be implemented permanently in the field but lacks the ability to be interrogated wirelessly, or without the use of large non-mobile laboratory equipment. Therefore, this chapter presents the development of a wireless impedance analyzer capable of actuating and sensing multiple channels (both a 4-channel and 32-channel model are designed and presented) thus enabling the wireless implementation of multiple spatial sensing techniques. After a more detailed examination of the motivation behind such a device, the design specifications and characterization are

presented, followed by two implementation cases; specifically the wireless implementation of electrical impedance spectroscopy (EIS) and also the wireless implementation of the thermal computed tomography (CT) method presented in *Chapter 4*. Finally, a synopsis is present including recommendations for further development of the wireless impedance analyzer.

5.1 Motivation

Although global sensing techniques are very important in monitoring the health of a structure, local sensing techniques are much more likely to locate and quantify the damage; however, local sensing techniques are often expensive and time consuming (Chang et al. 2003). Furthermore, many of these local techniques, such as non-destructive evaluation (NDE) lack the ability to provide continuous holistic data required for effective structural health monitoring (SHM) and data-driven asset management (Lynch et al. 2016). The manual labor, or time consuming aspect required for each test, or assessment, is being mitigated through the development of automated spatial sensing techniques such as those discussed in *Chapter 4* (*e.g.*, ultrasonic guided waves (Cho and Lissenden 2012; Fei Yan et al. 2010), sensing skins (Laflamme et al. 2012; Loh et al. 2009), thermal computed tomography (CT) method proposed therein). Yet, many lack practical field-deployable actuation and DAQ capabilities. Attributes required for such a device are that it must be low-cost (so it is cost-effective to include in an SHM system) and robust. Furthermore, such a device provides much more value the more versatile its functionality is to various sensing approaches or application to differing structural domains. The development of wireless sensor technologies has allowed for the cost of SHM systems to decrease and the

feasibility of their application increase (Lynch and Loh 2006). Thus making it apparent that in order for new spatial sensing techniques to be implemented in SHM systems they too must function wirelessly. Spatial sensing techniques have been developed for wireless implementation in the medical field (Bera and Nagaraju 2012). However, the key driver behind these approaches is to increase patient safety and improve the isolation of the subject being imaged (reduce noise). Furthermore, they can still be very costly and require large non-robust DAQ systems that are in the room with the patient, just not directly connected to the patient. Industrial applications of spatial sensing techniques have begun to incorporate wireless functionality (Goh et al. 2013). However, many of these are for monitoring fluid within a pipe or vessel and still lack the remote and large scale nature of health monitoring applied to structures and infrastructure systems. Towards this end successful wireless ultrasonic damage detection techniques have been developed (with voltage regulated output to actuate piezoelectrics) (Zhao et al. 2007). Pyo et al. (2011) developed a 32 channel wireless impedance analyzer specifically for EIT application (current regulated output). More recently, Huang and Loh (2015) developed a portable EIT device yet it lacked wireless capabilities and had a relatively large form factor. Therefore, the wireless impedance analyzer developed in this chapter has three key motivational drivers that result in its unique attributes:

- Wireless actuating and sensing device to enable SHM application of the thermal CT method developed in *Chapter 4*
- Multi-functional (versatile) device with the potential to enable multiple spatial sensing approaches (voltage and current regulated sensing and output with impedance matching)

- Smaller form factor and more robust compared to medical and in-lab applications (both in terms of hardware and embedded software)

To achieve these attributes certain design specifications are followed and the device characterized. The new device is validated by using the 4-channel model to perform EIS and the 32-channel model to perform thermal CT on an experimental specimen (which further validates the new thermal CT method) and experimental validation of spatial EIT on a concrete specimen, followed by a discussion of key findings and future recommendations.

5.2 Wireless Impedance Analyzer Specifications

5.2.1 Design Requirements

Incorporating wireless capabilities into the thermal CT imaging technique as well as into other spatial imaging techniques is essential to them being implemented in the field. In addition to functioning wirelessly, the impedance analyzer requires two key functionalities: generating a controlled output signal across a select pair of electrodes, or output channels and measuring the response at the other electrodes. Furthermore, each electrode or channel must be capable of output and input.

For the case of thermal CT, the output channel must provide sufficient power (*i.e.*, large DC current) to the selected heater(s) while measuring temperature (recorded as voltage) at all temperature sensor locations around the perimeter of the structural component being monitored/imaged. The heat must then be removed for a specified cooling period then applied to a different heater(s) and the temperature responses recorded

again. Therefore, the key requirements (aside from wireless functionality) are a large DC current output over multiple addressable channels and ADC over multiple addressable channels.

For the device to be versatile and capable of driving other means of spatial imaging it must have additional attributes. The two prevalent NDE (and pushing towards SHM) techniques are ultrasonic guided waves and EIT. Ultrasonics use piezoelectric crystals, or crystal stacks, to introduce mechanical vibrations into a structure. The physics of piezoelectric material dictate that this displacement (and consequent force) are in response to an electric potential across the crystal. Furthermore, ultrasonic damage detection is typically performed in the 10s of kHz range or greater. Therefore, voltage controlled, AC output is necessary.

Electrical impedance spectroscopy (EIS) provides a detailed interrogation of a specimen's, or circuit's, impedance properties. This enables more intricate damage detection and sensing because rather than just measuring a change in resistance, the impedance (which is a combination of resistance, inductance and capacitance) of a specimen or structural component can be tracked. This is done by outputting a regulated AC current or voltage across a specimen and measuring the opposite electrical property (*i.e.*, output current, measure voltage or vice versa). It is more practical to output a regulated/known current (as one can control the impedance properties internal to the device that affect current) and measure voltage across the specimen (as this can be performed with a straight-forward ADC). Nevertheless, following this protocol does necessitate the implementation of impedance matching on the wireless device. Additionally, the AC output is taken through a frequency sweep because the interaction between current and

voltage is driven by impedance and frequency (this is explained in more detail in the subsequent EIS section). In order for EIS to expand to electrical impedance tomography (EIT), or spatial imaging, the same methodology is implored with the augmentation of additional output/input channels such that impedance measurements can be made around the perimeter of the component being monitored.

Therefore, the wireless impedance analyzer is designed with the necessary traits for thermal CT, ultrasonic guided waves, EIS and EIT in mind. Consequentially, the signal generation module of the wireless impedance analyzer is capable of outputting both voltage regulated and current regulated output. That is, regardless of the load the regulated electrical property maintains at its desired value/waveform. The voltage and current regulated output each have three selectable types of output signals: 1) AC of desired frequency and amplitude with a 1.65V mean; 2) AC of desired frequency and amplitude with a 0V mean; 3) DC signal of any desired voltage. Furthermore, the AC signal can be programmed to output any desired waveform (*e.g.*, sinusoidal, triangular, saw tooth, etc.) For the common sinusoidal waveform the target attainable output frequency is 10 kHz. The signal is sampled via the microcontroller ADC simultaneously with the signal output. The device circuit shifts and scales the signal to ensure the voltage being read by the ADC is within the proper bounds (*e.g.* a zero-mean signal must be shifted to a 0 – 3.3V signal). The sampled data is stored temporarily on the device then transmitted to a laptop PC (in-lab) or small single board computer (in-field). In order to enable true spatial sensing 32 electrodes, or probes, need to be attained (nevertheless, both a 4-channel and 32-channel device are designed). The output, input (sensing) and ground can be routed to any electrode, or channel, based on user input. The device is built on a printed circuit board

(PCB) to increase robustness, performance and uniformity between devices as well as decrease noise. Special care is taken throughout the design to optimize for power consumption so the permanent/long-term application in the field is more feasible. Furthermore, the PCB layout is such that analog signal and digital components are isolated from each other except for a single ground point (star ground point); also, the bottom side of the PCB has a grounding plate covering as much area as possible. Both of these precautions decrease the noise of the device.

5.2.2 Design Overview

The wireless impedance analyzer designed for spatial imaging follows the requirements outlined above and can be broken down into the following six components:

- Microprocessor (MCU) – for control and communication with all other analyzer components
- Wireless transceiver (radio) – for the transfer of data and commands to and from a basestation
- Memory – data collected is stored until a large packet of data is ready for transmission
- Analog-to-digital converter (ADC) – sensing interface that translates measured data to digital data
- Direct-to-analog converter (DAC) – output interface that translates digital data/commands to desired electrical output
- Multiplexer (MUX) – directs the output/input signals to 32 addressable electrodes

At the center of the wireless analyzer is the *Martlet* baseboard developed at the University of Michigan (Kane et al. 2014) and shown in Figure 5.1. This baseboard contains a 32-bit Texas Instruments (TI) dual-core microcontroller (TMS320F28069 (TI 2011)) that can run at a clock speed of up to 90 MHz and has 256 kB flash memory and 100 kB random access memory (RAM). This MCU has onboard 12-bit ADC with a sampling rate up to 3.46 MHz and capable of sampling 0 – 3.3V input range. It has 39 total general purpose input/output (GPIO) pins, although 20 are required for standard *Martlet* operation; after repurposing three GPIOs originally used for LED lights, there are 22 remaining GPIOs available for use on the wireless impedance analyzer peripheral. The baseboard also has an integrated wireless transceiver (TI CC2520 paired with CC2591 (TI 2007, 2008)) and a memory card slot to increase the storage up to 32 GB. The *Martlet* communicates wirelessly with a receiver board that is connected to a PC (either a laptop or low-power single board computer) that stores data from and sends commands to the *Martlet*.

The baseboard is able to connect to peripheral boards through attachments on both the top and bottom. A battery peripheral board with (5) AA batteries (6 - 7.5V total

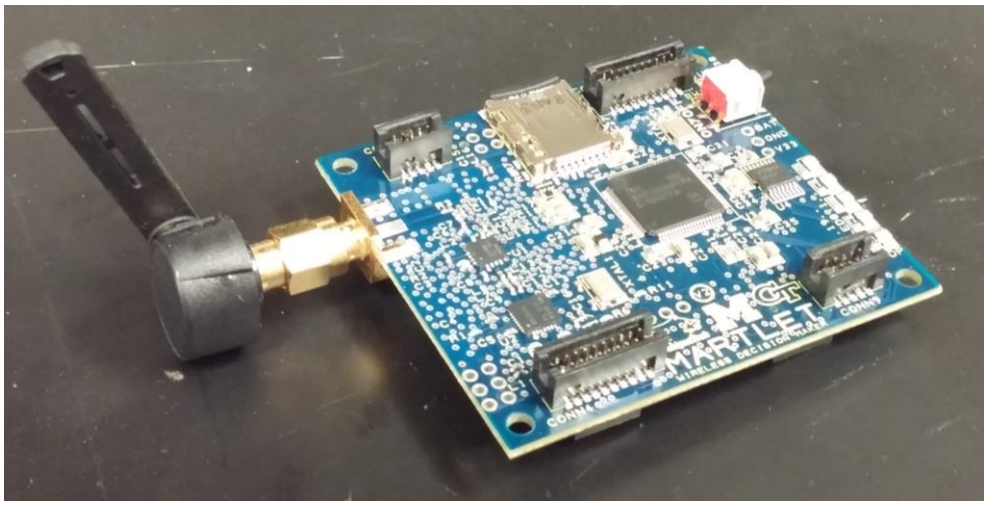

Figure 5.1 *Martlet* wireless platform baseboard.

potential regulated to the *Martlet*'s 3.3V operating power) connects to the bottom of the baseboard in order to power the *Martlet*. A peripheral board containing the DAC (including impedance matching and adjustable output types), ADC, and MUX connects to the top of the baseboard. Figure 5.2 depicts the 4-channel model with the complete assembly (battery pack, *Martlet*, and impedance analyzer) shown in Figure 5.3. The 32-channel model is shown in Figure 5.4 with the complete assembly shown in Figure 5.5. The battery pack attached to the bottom feeds power to all boards. However, the impedance analyzer circuit (top board) also employs two 9V batteries (regulated to +6V and -6V) to

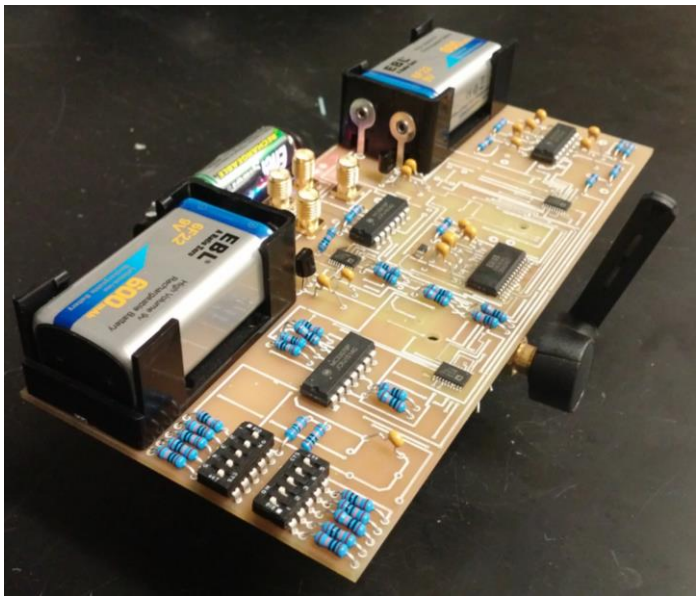

Figure 5.2 Wireless impedance analyzer 4-channel (EIS) model.

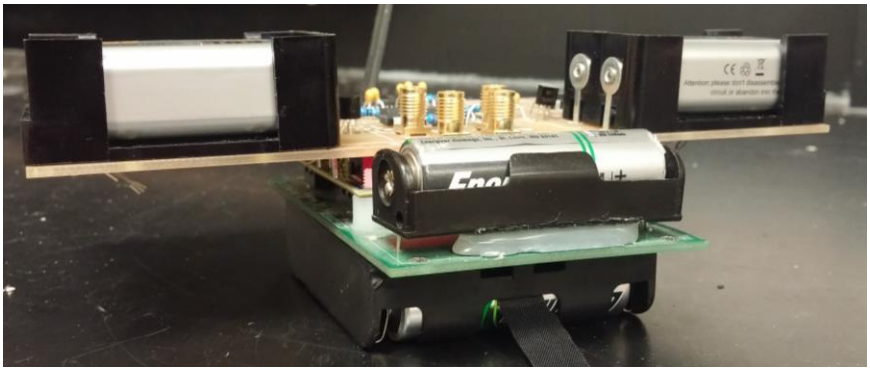

Figure 5.3 Complete assembly of battery pack, *Martlet* (motherboard with microprocessor), and 4-channel (EIS) wireless impedance analyzer.

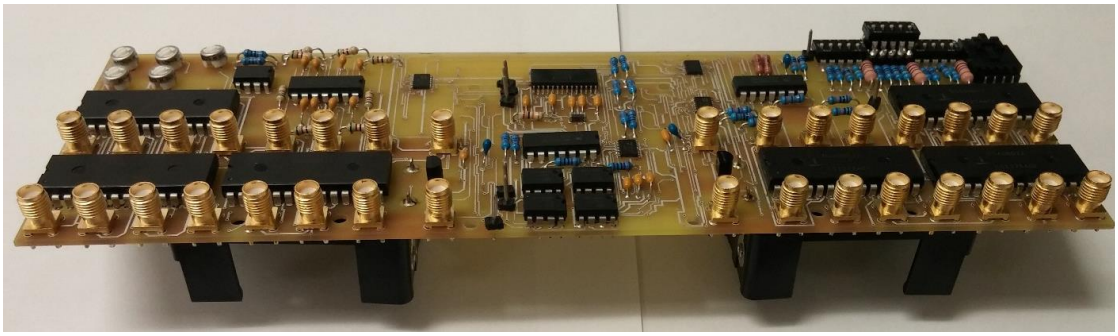

Figure 5.4 Wireless impedance analyzer 32-channel (EIT) model.

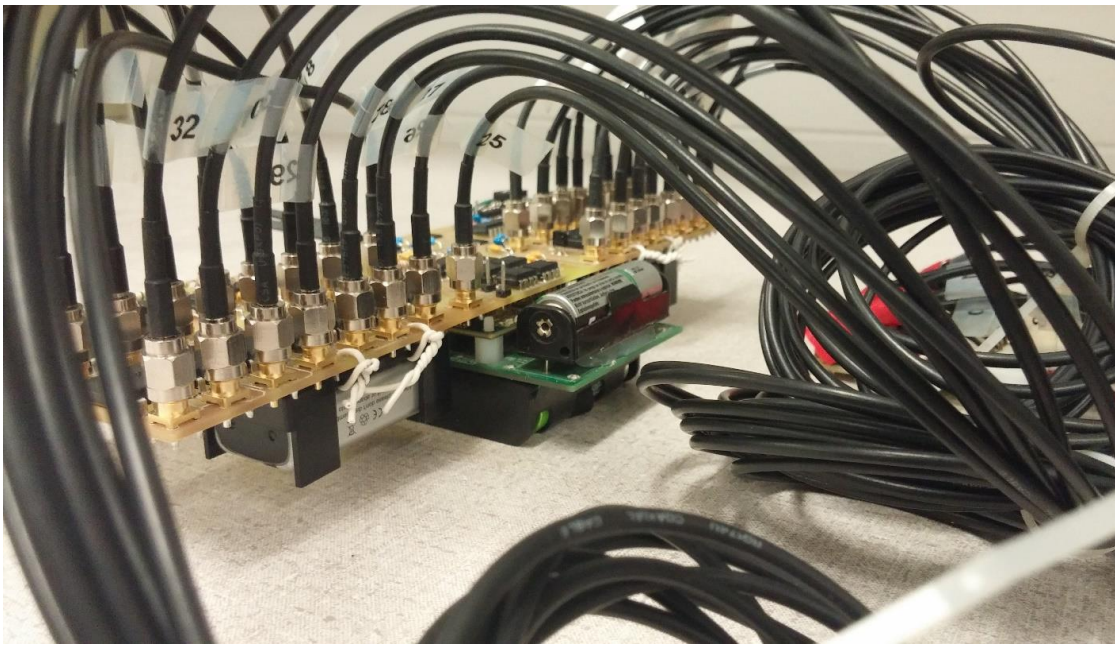

Figure 5.5 Complete assemby of battery pack, *Marlet* (motherboard with microprocessor) and 32-channel wireless impedance analyzer equipped with 9V wing batteries and attached to 32 electrode leads.

provide a greater magnitude potential as well as a negative potential to the op-amps required to achieve full-scale and zero-mean output.

Simplified block-diagram schematics of the wireless analyzer design that connects to the *Martlet* are shown in Figures 5.6 – 5.9. Note, Figures 5.6 and 5.7 are specifically of the 32-channel device, the only difference being that the 4-channel device uses GPIOs instead of manual switches (because the 32-channel model requires those GPIOs for channel selection). Initial prototypes use pulsed wave modulation (PWM) output from

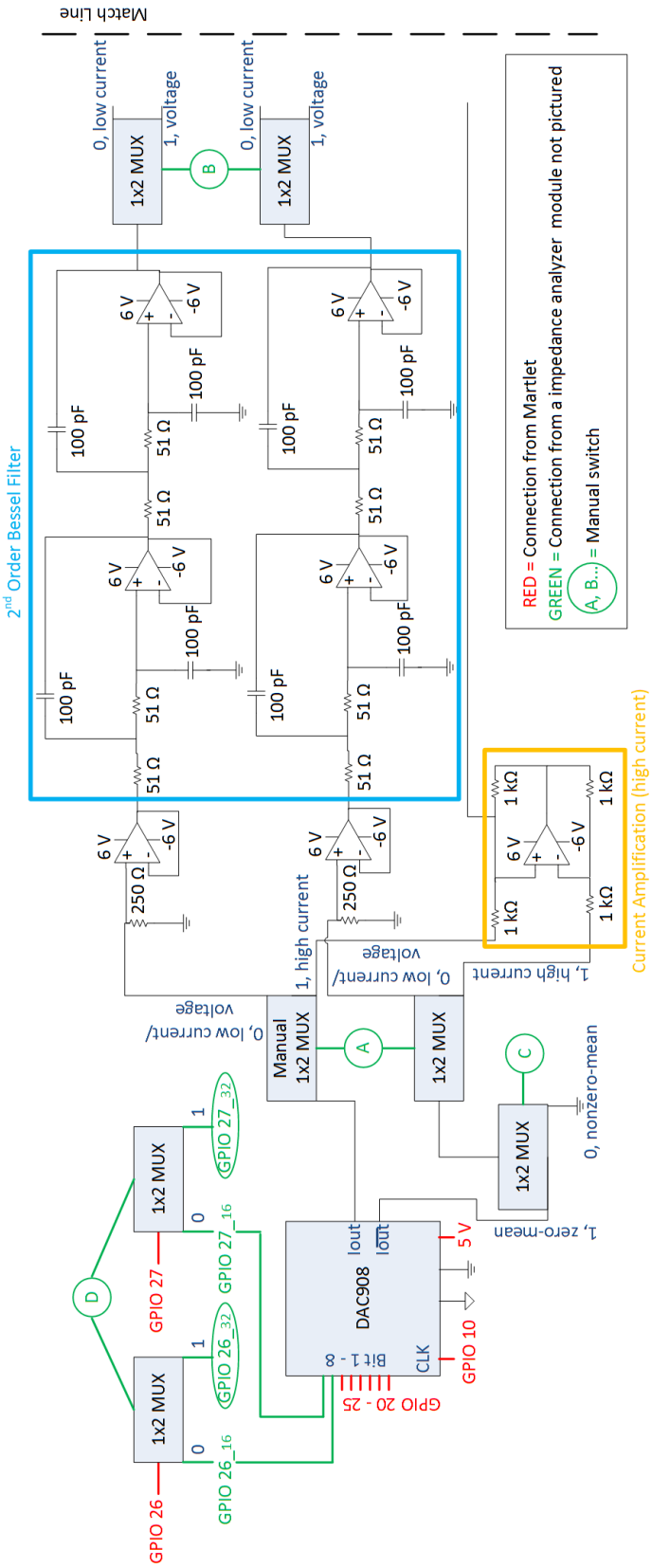

Figure 5.6 Design schematic wireless DAC part A.

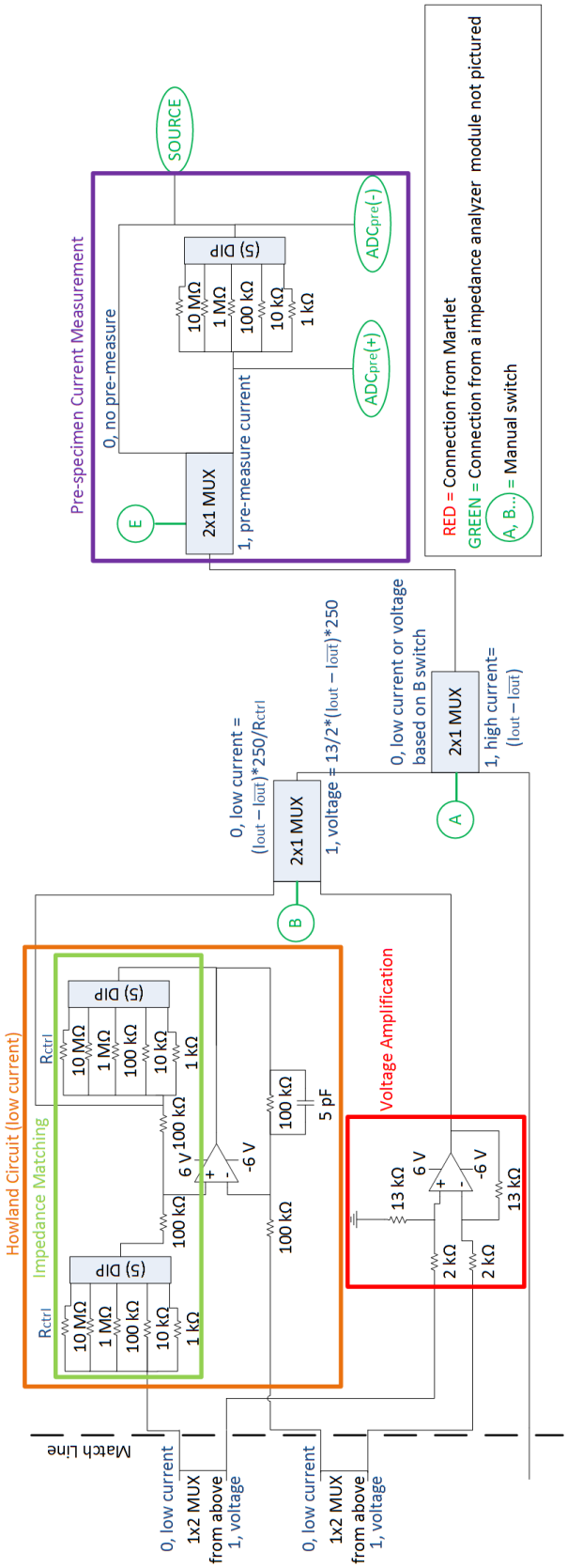

Figure 5.7 Design schematic wireless DAC part B.

the *Martlet* MCU; however, these devices result in high noise floors that cannot be overcome with passive filters (Alter 2008). At the higher frequencies required for completing electrical impedance spectroscopy (EIS) this noise level when using PWM DAC is too great to distinguish the magnitude and phase differences between the voltage and current. Therefore a dedicated DAC chip (DAC908 (Burr-Brown 2003)) is used. It is an 8-bit DAC with an update rate of 200 MSPS. This means that the limiting factor on the update rate of the wireless impedance analyzer is controlled by the microprocessor (TMS320F28069) clock speed of 90 MHz and overhead inherent to the *Martlet* platform. The only input this chip requires from the microprocessor is a CLK and 8 GPIOs; there is an optional power down pin-out that can be left open if the DAC is to be powered whenever the device is on. Another benefit to using the DAC chip is that the impedance analyzer circuit can easily be modified for use with another wireless platform by simply routing the GPIOs and CLK from the MCU to the DAC chip; the remainder of the circuit could remain as currently designed.

Depending on the reference resistor connected to the DAC the full-scale current output is between 2 mA and 20 mA. Note, high speed DACs (such as this one) supply current regulate output and not voltage. Using a reference resistor of 19.83 kΩ provides a full-scale output of 2 mA; therefore the current output varies between 0 and 2 mA depending on the 8-bit code input from the MCU. At a programmed frequency the MCU enters a coding interrupt which causes it to refer to a look-up table (which contains tabulated values for the desired waveform, *i.e.*, sinusoidal, triangle, etc.) and retrieve the value of the next output, it then rights an 8-bit word to the GPIOs connected to the DAC. The DAC reads this word every clock cycle (CLK from microprocessor PWM that is

connected to the DAC, not microprocessor clocking speed) and adjusts its output accordingly. Note, the MCU and DAC update frequency must be greater than the desired waveform frequency. For example, a 1 Hz, 256 point sinusoidal waveform requires an update frequency of 256 Hz. Another feature of this DAC is that it outputs a complementary current value at a second pin. That is, one pin outputs I_{OUT} and another pin outputs $I_{\overline{OUT}}$. When I_{OUT} is at full-scale, $I_{\overline{OUT}}$ is at 0 and when I_{OUT} is at 0, $I_{\overline{OUT}}$ is at full-scale as shown in the following equations:

$$I_{out} = I_{FS}\left(\frac{B_8}{255}\right), \tag{5.1}$$

$$I_{\overline{out}} = I_{FS}\left(\frac{255-B_8}{255}\right), \tag{5.2}$$

where, I_{FS} is the full-scale output and B_8 is the 8-bit binary input from the microprocessor. The complementary output enables a current swing of $(-)I_{FS}$ to $(+)I_{FS}$ with the use of differential amplifiers. Therefore, zero-mean outputs are achievable without any additional output circuitry.

The characteristics of the programmable output are selected using GPIOs from the MCU for the 4-channel model and manual switches for the 32-channel model (as the multiple multiplexers for the 32-channel model require the use of more GPIOs). Table 5.1 summarizes the selectable GPIO/switches used to control the device output. Referring to Figure 5.6, when switch A (GPIO 30 on the 4-channel model) is high/on the *high current* output is selected which differentially amplifies I_{OUT} and $I_{\overline{OUT}}$ to result in a current regulated output signal, I_{source}, of:

$$I_{source} = I_{out} - I_{\overline{out}}. \tag{5.3}$$

No filter is needed for this output type as it is expected to only be used to power heaters with a DC signal.

When switch A is low the *low current/voltage* output is selected. When connected to a 250 Ω resistor and op-amp, as shown in Figure 5.6, this produces a full-scale voltage output of 0.5V (which is the recommended maximum full-scale voltage from the DAC chip). This is clearly necessary for the voltage output but also to step down the current output while maintaining current regulation and adjusting its magnitude for impedance matching. After the current has been converted to voltage both the standard and complimentary outputs pass through a 2nd order low-pass Bessel filter. This is to remove high-frequency noise components while having a constant phase group delay (when output frequency is changed the phase delay inherent to the device remains the same) (Thomson 1949).

After the Bessel filter switch B (GPIO 31 on 4-channel model) is used to select whether the filtered signal will be voltage or current regulated. When switched to high, the *voltage* regulated output, V_{source}, is selected and the difference between the standard and complimentary signal is amplified by a gain of 6.5; the output signal follows:

Table 5.1 Device output GPIO/switch functions.

Manual switch (32-channel model)	**GPIO (4-channel model)**	**Switch off/low/0**	**Switch on/high/1**
A	30	low current or voltage	high current
B	31	low current	voltage
C	34	nonzero-mean	zero-mean (ADC shift)
D	-	16-channel MUX, 8-bit DAC	32-channel MUX, 6-bit DAC
E	-	pre-specimen measurement	bypass pre-specimen measurement

$$V_{source} = 6.5 * (I_{out} - I_{\overline{out}}) * 250. \quad (5.4)$$

When switch B is low, the *low current* regulated output is selected. For the output to once again be current regulated (maintain desired current output regardless of the load) a Howland circuit is required as shown in Figure 5.7. This particular Howland circuit is designed uniquely to adjust the control resistors, R_{ctrl}, to match the output impedance close to that of the impedance of the load, or specimen being interrogated; this greatly improves sensing resolution. Both resistor registers that comprise the Howland circuit as well as the pre-measure register must be adjusted to the same resistor value which must be in the same order of magnitude as the impedance of the specimen being monitored. The output from the Howland circuit (low current regulated) follows:

$$I_{source} = (I_{out} - I_{\overline{out}}) * \frac{250}{R_{ctrl}}. \quad (5.5)$$

Switch C (GPIO 34 on 4-channel model) selects whether a zero-mean signal (switch high) or a nonzero-mean signal is output (switch low). If a nonzero-mean signal is selected the complimentary output from the DAC, $I_{\overline{out}}$, is grounded (setting it to 0 in Equations 5.3 – 5.5). Switch C also determines whether or not the signal needs to be scaled down and shifted back to nonzero-mean before entering the ADC onboard the MCU (which has an input range of 0 – 3.3V) as shown in Figure 5.8. The ADC circuitry shown in Figure 5.8 uses instrumentation op-amps in order to more accurately measure the input as well as shift the signal if necessary.

Switch E allows for the pre-specimen measurement register to be bypassed (0 = perform pre-specimen measurement, 1 = by pre-specimen measurement), which is useful in high current applications (*e.g.*, thermal CT) in which this register would expend significant energy. Because there is a limited number of GPIO pins, switch D allows the

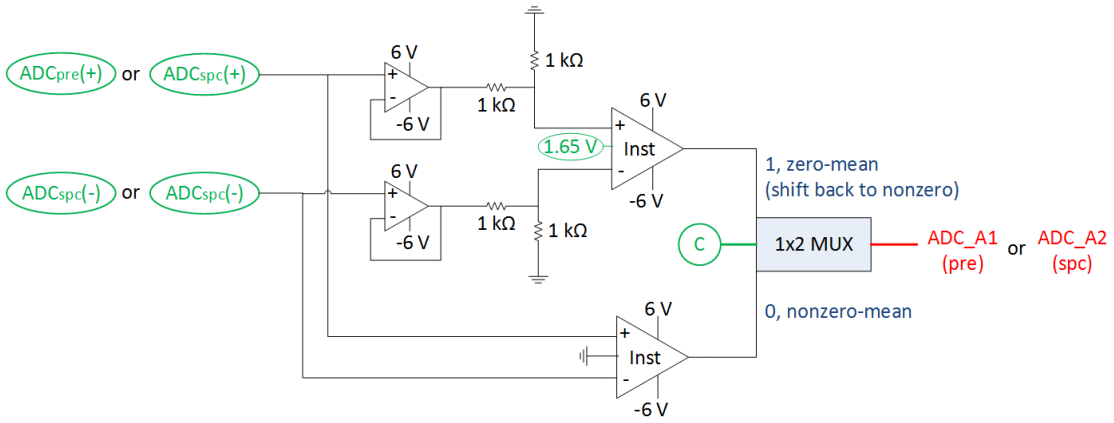

Figure 5.8 Design schematic ADC circuit.

user to select whether a 32-channel input/output with 6-bit DAC resolution is used (switch high) or a 16 channel input/output with 8-bit DAC resolution is used (switch low). Note, the 4-channel, EIS, model doesn't require switches D and E.

The schematic of the SMA electrode connections, or probes, for the 4-channel model used primarily for EIS is shown in Figure 5.9a. The output, or signal source attaches to one probe and is grounded (signal sink) with another probe. The remaining two probes are used to precisely measure the signal across the specimen; taking advantage of 4-terminal measurement procedures (Janesch 2013). The 32-channel model is required for EIT and thermal CT; the programmable multiplexers select which electrodes connecting to the specimen are used as the current source and sink (output) as well as which electrode is connected to the ADC for sampling (input), see Figure 5.9b. For this device the ADC is referenced to the sink/ground (which is justifiable because in 4-terminal sensing the sink and ADC reference are often attached to the same location). Therefore, every electrode can function as a source, sink or ADC. The embedded programming steps through pre-determined (based on the sensing method) sink-source combinations and for each combination it cycles through voltage measurements at each electrode.

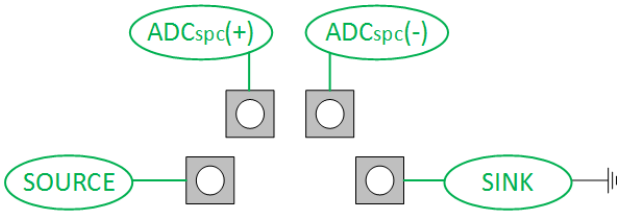

(a)

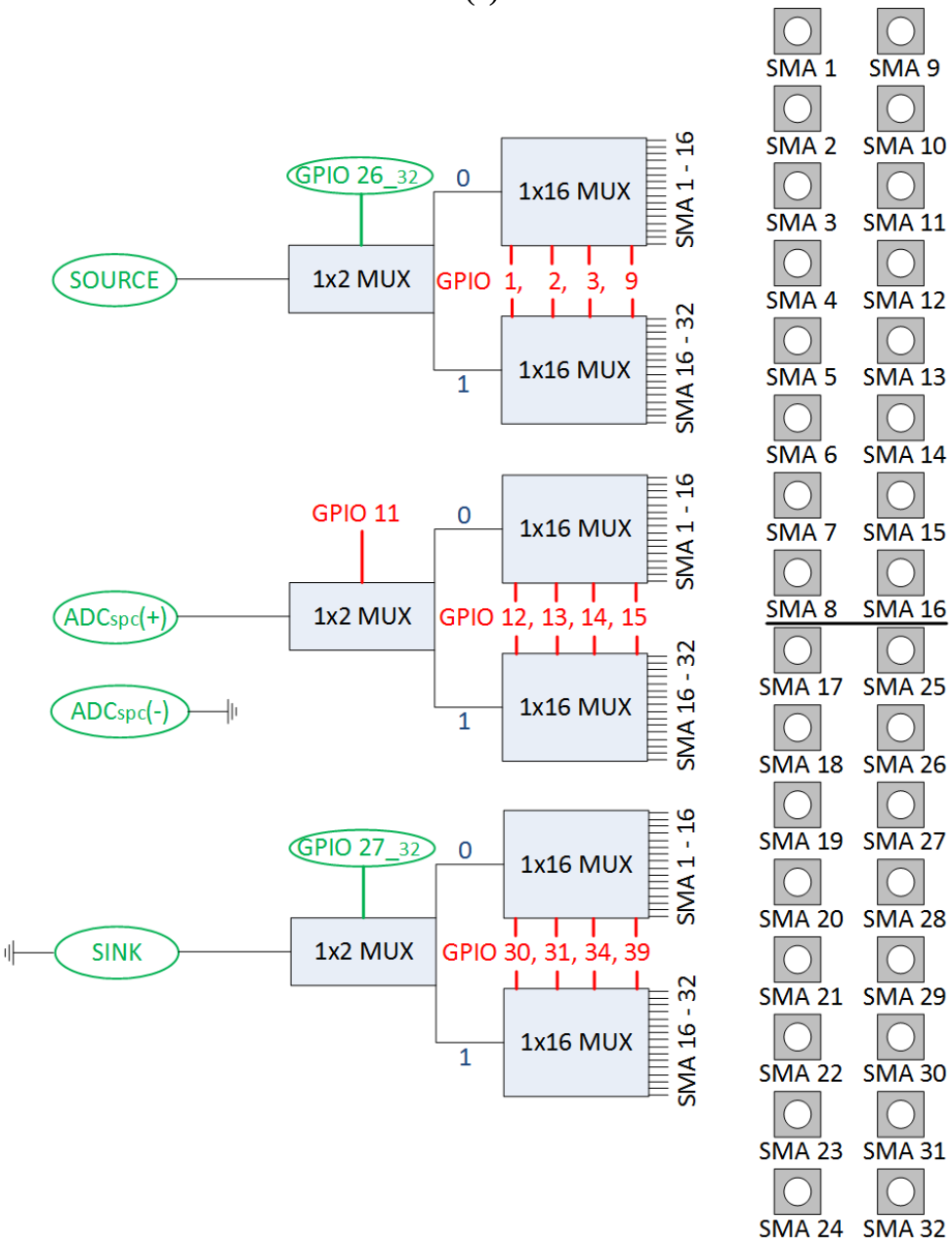

(b)

Figure 5.9 Design schematic electrodes: (a) 4-channel (EIS) model; (b) 32-channel model.

5.2.3 Device Characterization

Characterization tests are performed on the wireless impedance analyzer to verify its functionality. These are followed by two complete experimental validations (EIS and thermal CT) discussed in the following section. The items characterized in this section are:

- Read/write of microprocessor and memory
- Wireless communication
- ADC data collection
- DC signal generation
- Current regulated signal
- AC signal generation
- 32 channel MUX interface

Because the impedance analyzer is built upon the existing *Martlet* platform the first two items are achieved trivially; nonetheless they are crucial to a functioning device. First, the microcontroller read/write capabilities and execution of embedded code is tested using a debug module in Code Composer Studio 5.5.0 (TI 2014). Next, wireless communications are achieved while maintaining data integrity, thus verifying the key communication functionality making this technology field deployable. The remainder of the characterization and experimental tests are performed wirelessly. To test the ADC, a signal generator is connected to the ADC channels and the generator's output is successfully converted to a digital format and transferred wirelessly.

The DC output is tested for both voltage and current regulated. As the current regulated is more complex, and crucial to EIS, a test of the Howland circuit functionality is presented in Table 5.2. A desired current output is programmed and the source-sink

Table 5.2 Current regulated functionality of wireless device.

Load (Ω)	Programmed Current (μA)	Measured Current (μA)
83.3	2000	2040
125	2000	2000
250	2000	2000
1790	200	213
3870	200	214
9000	200	214
1790	130	124
3870	130	124
9000	130	124
15830	130	124

connected to varying loads. As can be seen, the desired current output is consistent and correct regardless of the load. The very slight discrepancies between theoretical (programmed) and measured current can be attributed to slight imperfections/nonuniformity between the resistors used in the Howland circuit. However, these imperfections manifest themselves in the same manner regardless of the load. For example, all 130 μA programmed outputs are consistent at 124 μA actual output. Consequentially they do not have an effect on device performance or data interrogation (the slight shift occurs the same for every load and is captured in the pre-specimen current measurement). The key validation is that the current can be regulated regardless of the load, or specimen, properties.

To test the AC output multiple waveform look-up tables are programmed into the MCU. These waveforms are tested at multiple output frequencies. Figure 5.10 shows the oscilloscope reading for both the DAC output and the ADC input (just before entering the ADC pin on the MCU) for a sinusoidal and triangular waveforms, both at 64 Hz. Notice, the output (shown in yellow) is zero-mean yet the input (shown in green) has been shifted

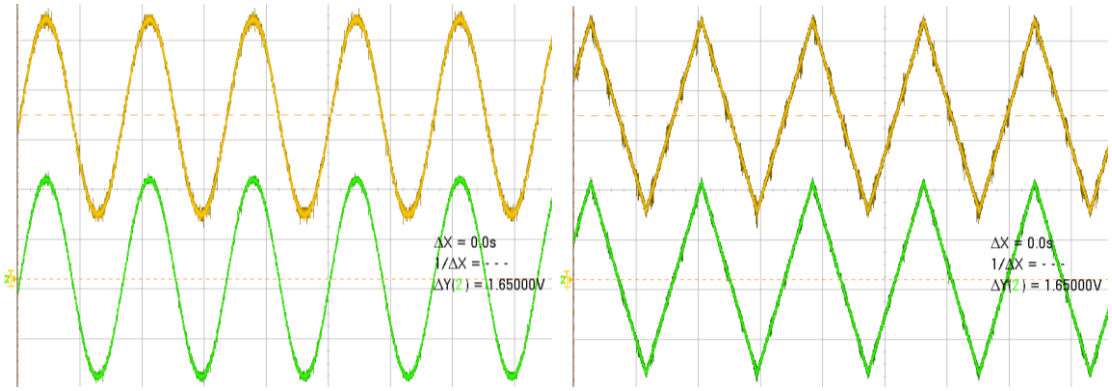

(a) (b)

Figure 5.10 Zero-mean DAC output (green) and shifted, 1.65 V mean, ADC input (yellow): (a) sinusoidal; (b) triangular.

to a 1.65V mean so the signal remains within the MCU ADC capabilities of 0 – 3.3V. Figure 5.11 shows the frequency sweep of a sinusoidal output from 2 Hz to 8192 Hz.

The functionality of the MUXs is tested manually by verifying that the specified impedance analyzer lead (source, sink or ADC) is connected to the desired/programmed electrode. In addition to these manual test an automated test is performed to verify the dynamic ability to switch MUX channels and still perform proper DAC/ADC functionality. This test follows the setup shown in Figure 5.12 and also serves as further validation of the ADC capabilities. A 3.23V DC output is applied to the far left of a series of resistors through channel 1 and grounded on the far right through channel 8. The ADC channel steps sequentially through channels 1 – 8 (remaining on channel 1 and 8 for twice the amount of time to test the versatility of the ADC sweep). Note, a single lead each for channels 1 and 8 acts as both an input and output. The measured response of the analyzer as the ADC cycles through the 8 channels is provided in Figure 5.13. As expected, the

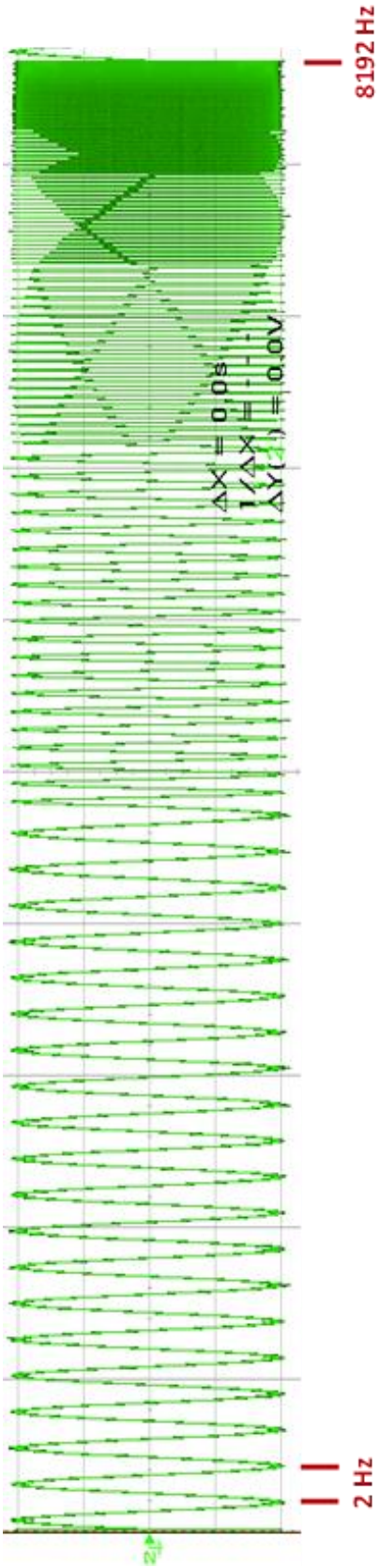

Figure 5.11 Frequency sweep of sinusoidal wireless impedance analyzer DAC output.

ADC readings (recorded on MCU and wirelessly transferred to the PC) step down in voltage as the measurement location moves closer to the sink (ground). Note, the final voltage measured at the channel also being used as the output sink is not 0V because of parasitic resistance within the analyzer circuitry. This same test is performed for channels 9 – 16, 17 – 24, and 25 – 32 and successfully validates the 32-channel MUX functionality. Therefore, the device is successfully validated to meet the required specifications, namely: wireless command and data collection, DC and AC output of any waveform (sinusoidal, triangular, square, zero-mean, nonzero-mean), voltage and current regulated output, and 32-channel functionality all located on a robust, small form factor PCB.

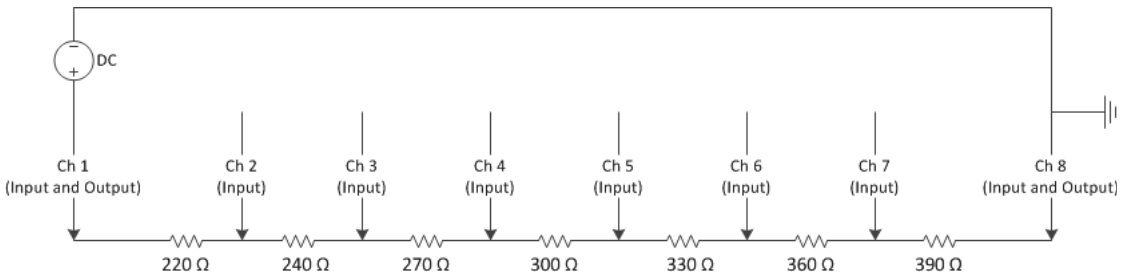

Figure 5.12 Test schematic ADC and MUX characterization.

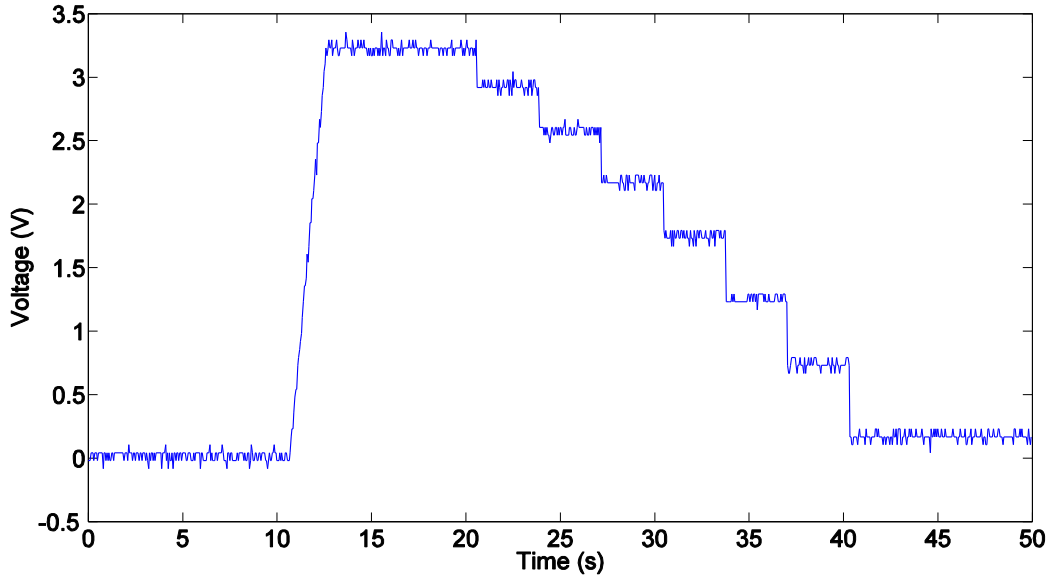

Figure 5.13 ADC measurement response as MUX steps through channels 1 – 8 as shown in Figure 5.12.

5.3 Electrical Impedance Spectroscopy (EIS)

Electrical impedance spectroscopy (EIS) requires the detection of current and voltage magnitude as well as the phase delay between the two at different frequencies. Therefore, the EIS device must be capable of injecting AC current regulated excitation; whereas, in some instances for EIT, DC voltage or current can be used for output. The 4-channel model (Figure 5.2 – 5.3, 5.6 – 5.8 and 5.9a) allows for the isolation and development of two of the largest obstacles for the wireless impedance analyzer; namely, an accurate AC output at an appreciable voltage/current from a MCU and current regulation on such a small wireless device. Furthermore, it avoids the added parasitics and complexity of multiple multiplexers required for a 32-channel model. Thus allowing for a more precise measurement of impedance properties (*i.e.*, precise magnitude and phase comparisons of current and voltage). Referring to Figure 9a, the source/injection and sink/ground electrodes attach to either side of a specimen. The positive ADC input electrode attaches to the same side of the specimen as the source and the negative ADC input attaches to the same side as the sink. Thus, a (known) current is injected and a voltage measured across the specimen.

To perform an EIS measurement a frequency sweep of sinusoidal current regulated output is executed, similar to that in Figure 5.11. By doing so the impedance, *Z* (which has resistance, *R*, inductance, *L*, and capacitance *C* components) of a specimen or circuit can be analyzed. The impedance of a specimen is determined by its voltage and current response as shown in Equation 5.6:

$$Z(t) = \frac{V(t)}{I(t)} \tag{5.6}$$

The time response of voltage and current can be represented as:

$$V(t) = V_0 sin(\omega t), \tag{5.7}$$

$$I(t) = I_0 sin(\omega t + \phi), \tag{5.8}$$

where V_0 is the peak voltage value, I_0 is the peak current value, ω is the excitation frequency and ϕ phase delay between voltage and current. Combining Equations 5.6 – 5.8 yields:

$$Z(t) = \frac{V_0 sin(\omega t)}{I_0 sin(\omega t+\phi)}. \tag{5.9}$$

Following Euler's relationship ($e^{j\phi} = cos\phi + jsin\phi$), Equation 5.9 can be rewritten as:

$$Z(\omega) = \frac{V_0 e^{j\omega t}}{I_0 e^{j\omega t-\phi}}, \tag{5.10}$$

By defining $Z_0 = \frac{V_0}{I_0}$, Equation 5.10 can reduces to:

$$Z(\omega) = Z_0 e^{j\phi}, \tag{5.11}$$

with the phase delay, ϕ, and magnitude of impedance, Z_0, both being a function of the excitation frequency, ω. All of the necessary values to solve Equation 5.9 or 5.11 are known or can be measured using the wireless impedance analyzer. That is, the excitation frequency magnitude of the current is known, the magnitude of the voltage is measured and the delay between the two is measured. One method to display and analyze impedance data is to calculate a Nyquist plot. This is done by plotting the real portion of impedance on the abscissa and the imaginary portion on the ordinate. This can be done by taking the magnitude, Z_0, for a given excitation frequency as the distance of the data point from the origin and the phase, ϕ, as the angle measured from the abscissa and magnitude line. For instance, a 0° phase would result in the data point being plotted directly on the abscissa at the calculated magnitude, and a phase of 90° would result in the data point being plotted directly on the ordinate. This is repeated for every excitation frequency employed.

To test the EIS capabilities of the wireless device a circuit with known impedance properties is used. The circuit is a parallel RC circuit with R = 1.98 kΩ and C = 01 µF, as shown in Figure 5.14. The impedance, Z, of a resistor is:

$$Z(\omega) = R, \tag{5.12}$$

The impedance of a capacitor is:

$$Z(\omega) = \frac{1}{j\omega C}, \tag{5.13}$$

The impedance of an inductor (not used in this particular experiment but presented for completeness) is:

$$Z(\omega) = j\omega L. \tag{5.14}$$

Adding impedance of R and C in parallel gives:

$$Z(\omega) = \left(\frac{1}{R} + j\omega C\right)^{-1}. \tag{5.15}$$

The theoretical Nyquist curve is plotted for the experimental RC circuit using Equation 5.15 and is shown in Figure 5.15 with square line markers. The wireless impedance analyzer excites the RC circuit with sinusoidal frequencies up to 8192 Hz and the response is measured with a 40 kHz sampling rate. Because the sampling rate only allows for the collection of four points per wave period (at the higher frequencies), multiple wave periods are collected in order to accurately determine the phase and peak values. This

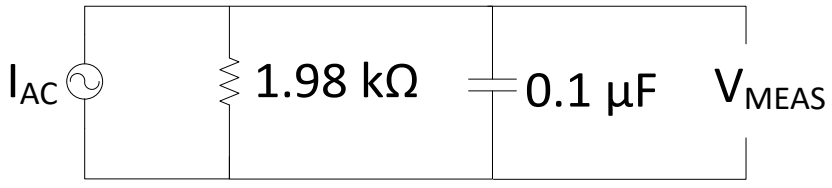

Figure 5.14 Test schematic for parallel RC circuit EIS experiment.

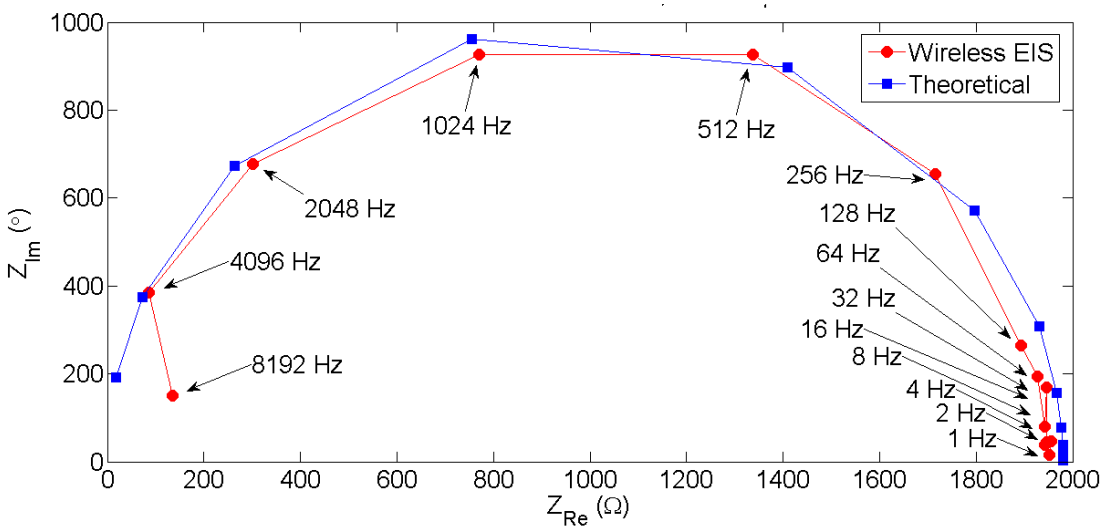

Figure 5.15 Theoretical and experimental Nyquist curve for parallel RC circuit; R = 1980Ω, C = 0.1 μF.

results in an experimental Nyquist curve shown by the line with circle markers in Figure 5.15. As expected the real portion of impedance decreases as frequency increases. The strong agreement between theoretical and the wirelessly measured experiment validate the EIS functionality of the 4-channel model of the device.

5.4 Electrical Impedance Tomography (EIT)

The 32-channel model is used to perform wireless EIT measurements on a sample of nano-engineered concrete. The concrete specimen and EIT algorithm are provided by Gupta et al. (2016) and are not part of the work in this dissertation. However, they provide a valuable opportunity to highlight the capabilities of the wireless device that *is* developed in this dissertation. The small form factor wireless impedance analyzer is used to automatically wirelessly interrogate the concrete specimen and the data used to reconstruct an image of the damage state of the specimen.

The specimen is a 5 inch x 5 inch (12.8 cm x 12.8 cm) and 0.35 inch (9 mm) thick concrete made with nano-engineered cement as shown in Figure 5.16. There are 32 copper mesh electrodes located around the perimeter (8 on each side). Each electrode is 0.24 inches (6 mm) wide and spaced evenly with a 0.24 inches (6 mm) space from the edge of one electrode to the edge of the next electrode. The corners of the sensing perimeter do not contain electrodes; thus, the total sensing perimeter is 4 inch x 4 inch (10.2 cm x 10.2 cm). The wireless impedance analyzer injects (source) and grounds (sink) current at given electrode combination and records the voltage response at all other electrodes. The injection-ground combination is altered following the sequence outlined by Gupta et al. (2016) and the voltage response recorded for every injection-ground combination. The interrogation time per sequence is 64 seconds and 6 sequences are executed in order to increase resolution; therefore, the total interrogation time is 384 seconds, or roughly 6 ½ minutes.

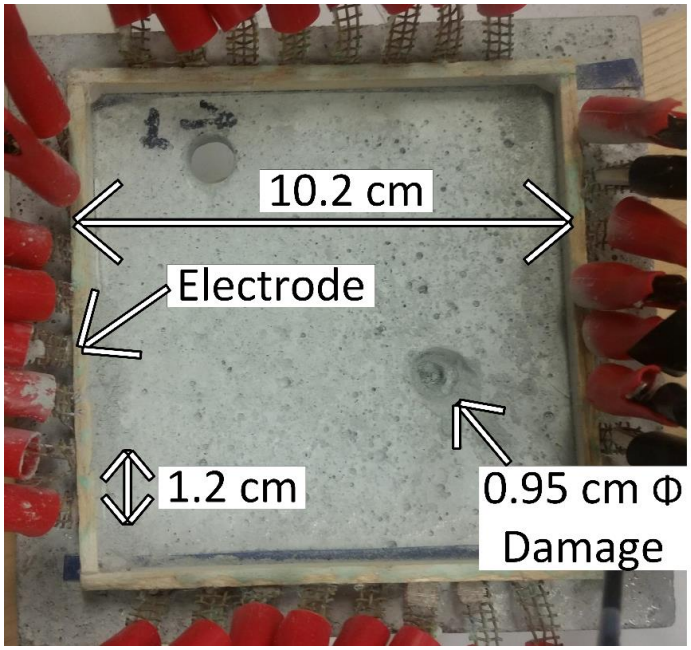

Figure 5.16 Nano-engineered concrete experimental setup for wireless EIT.

Referring to Figure 5.16, the original, baseline, image is collected after the hole in the top left corner existed. That is, the damage in the top left already existed before any data is collected. After the baseline image is collected, a 3/8 inch (0.95 cm) diameter hole is drilled in the bottom right corner of the specimen. Therefore, the damaged scenario reconstructed with the EIT algorithm is the change in the conductivity mapping from the concrete specimen with one hole, to the concrete specimen with two holes. Figure 5.17 presents the reconstructed image that clearly identifies the existence of new damage in the bottom right corner. The successful execution of wireless EIT on an experimental sample further validates the multi-functional capabilities of the wireless impedance analyzer.

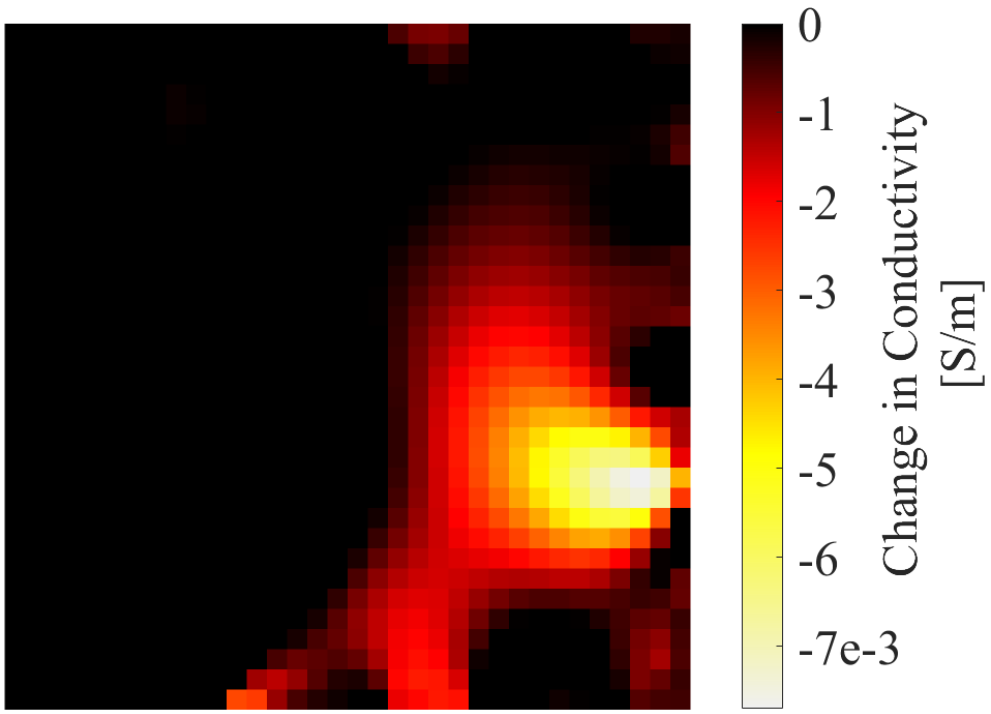

Figure 5.17 EIT reconstructed image of damaged nano-engineered concrete specimen (Gupta et al. 2016).

5.5 Thermal Computed Tomography

The 32-channel model of the wireless impedance analyzer (Figures 5.4 – 5.8 and 5.9b), and the thermal computed tomography (CT) method developed in the previous chapter are validated through the experiment described in this section. The experiment is setup to automatically detect damage induced in an aluminum specimen using data from heaters and temperature sensors located around the perimeter of the specimen that are actuated and sampled, respectively, using the wireless impedance analyzer. After the sensors are installed a set of data is collected of the undamaged specimen to give a baseline. Then a damage is induced and another set of data collected. The set of data from the specimen in its undamaged state and in its damaged state are used as input to the thermal CT spatial imaging algorithm. This approach allows for the detection of damage using a low-cost, robust wireless sensor setup and does not require the use of models or model updating.

A 15.9 inch x 12 inch x 0.031 inch (40.5 cm x 30.6 cm x 0.079 cm) aluminum alloy 6061 plate is used for the experiment (as aluminum is a common structural material that is susceptible to fatigue and damage in naval vessels) and is shown in Figures 5.18 and 5.19 (Figure 5.18 is of the entire plate in the undamaged state and Figure 5.19 is a close-up of the sensor perimeter of the plate in the damaged state). There are 16 heater-sensor pairs installed with a square perimeter of 4.72 inches x 4.72 inches (12 cm x 12 cm). Therefore, the spacing between each pair is 1.18 inches (3 cm). The perimeter is centered within the aluminum plate. As can be seen in Figure 5.19, the heaters are located on the inner edge of the perimeter and the sensors on the outer edge. Unlike EIT and ultrasonics, a single electrode cannot be used as an actuating and sensing channel because the heaters and

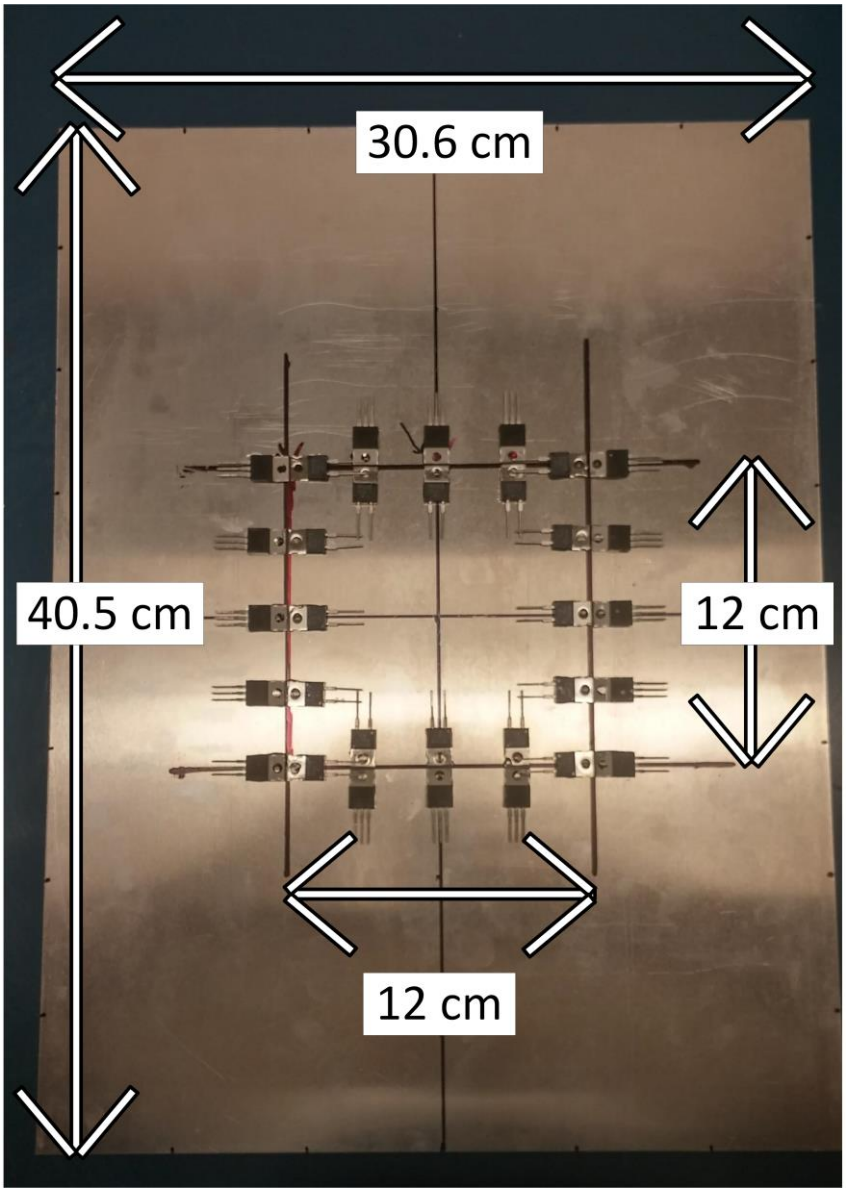

Figure 5.18 Experimental setup for wireless thermal CT; image of entire plate in an undamaged state with heaters and sensors installed.

sensors at each location are individual components using separate transduction mechanisms. Therefore, the 16 heater-sensor pairs require the use of all 32 channels of the wireless impedance analyzer. After measurements are collected for the undamaged specimen (as will be described subsequently), damage is induced in the form of a ¾ inch

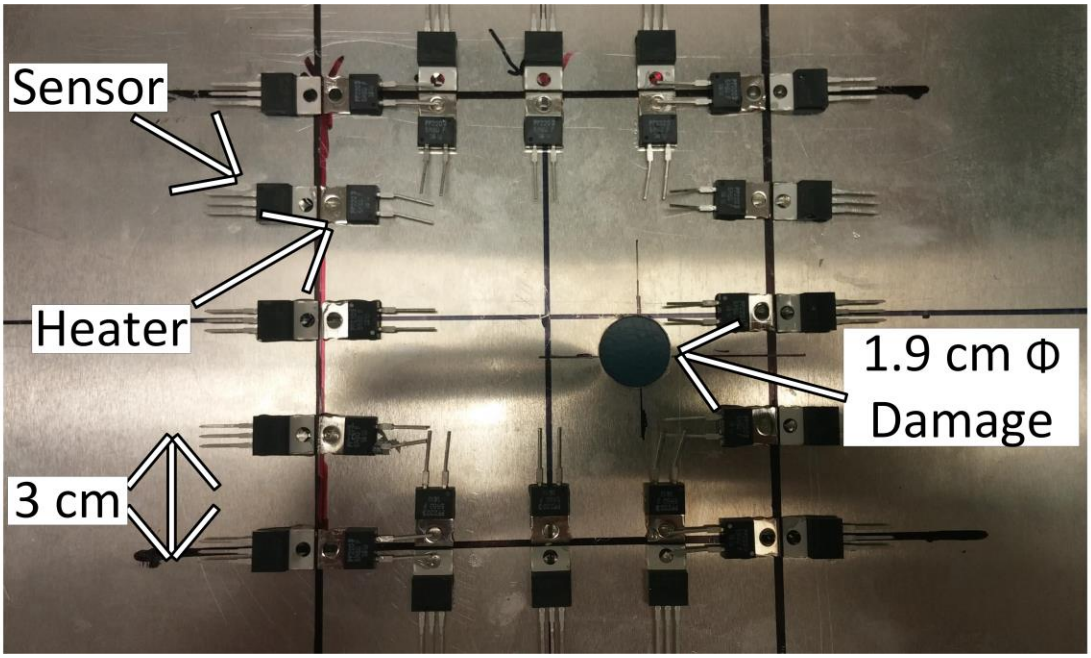

Figure 5.19 Experimental setup for wireless thermal CT; image of the sensing perimeter of the plate in a damaged state with heaters and sensors installed.

(1.9 cm) diameter hole in the plate located 0.98 inches (2.5 cm) horizontally to the right of center and 0.39 inches (1 cm) vertically below center as shown in Figure 5.19.

The same component types are used as in the preliminary experiments in *Chapter 4*. That is, the heaters are resistors with a specified resistance of 5.6 Ω, power rating of 20 W and with an exposed metal element (Bourns PWR220T-20-5R60F) for heat dissipation (Bourns 2011). The temperature sensors are solid state integrated circuits (Texas Instruments LM5DT) that linearize the response of the internal thermistor; these sensors have a -55℃ to 150℃ operating range with an accuracy of 0.25 ℃ when operating near room temperature and a sensitivity (or precision) of 10 mV/℃ (TI 2000). An op-amp circuit is added to the heaters and sensors, respectively, in order to improve the performance of the wireless thermal CT. Therefore, the sensor setup includes the wireless device with each channel connecting to an op-amp (which op-amp determined by whether the channel is to

be used as a heater or sensor) which is connected to a transducer (heater or sensor) that is permanently attached to the plate. The circuit shown in Figure 5.20a (with the TCA0372 op-amp (OS 2013)) is used to increase the supplied current to 1 A in order to provide more power to the heater; the power supplied for this experiment is 5.6 W. Note, this op-amp can also be attached to additional batteries to allow more prolonged field application (*i.e.*, the power required for heating would be separate from that to power the wireless device if larger amounts or more frequent applications of heat are desired). Because the thermal CT sensing approach does not increase the temperature of the specimen significantly above the ambient temperature, the temperature sensors readings are always in the 0.2 – 0.4 V range (recall sensor specification of 10 mV/℃, for example, 22℃ has a 0.22 V output). Therefore, in order to increase temperature sensing resolution and use the full spectrum of the 0 – 3.3 V ADC, the circuitry shown in Figure 20b (with the MC33078 op-amp (OS 2011)) is used to amplify the signal by a gain of 7.3. Therefore, the final temperature resolution, T_{res}, is 0.01℃:

$$T_{res} = \frac{V_{ADC_{FS}}}{B_{res}} * \frac{1}{T_{sens}G} = \frac{3.3V}{2^{12}-1} * \frac{1}{\frac{0.01\,V}{^{\circ}C} * 7.3}, \tag{5.16}$$

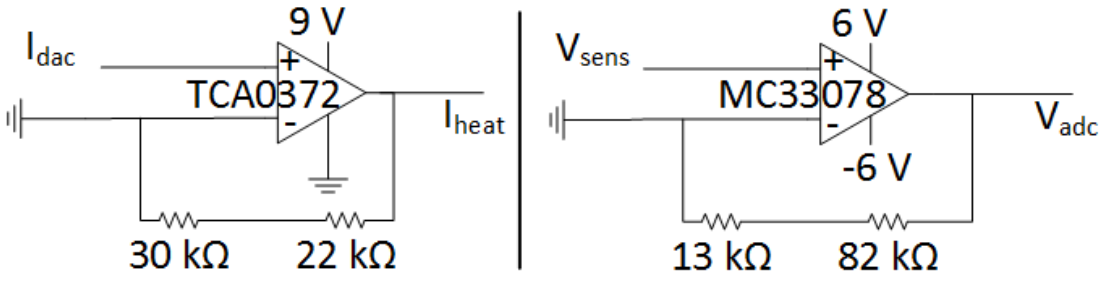

(a) (b)

Figure 5.20 Op-amp circuits used for thermal CT: (a) sensing op-amp; (b) heating op-amp.

where, $V_{ADC_{FS}}$ is the ADC full range, B_{res} is the ADC bit resolution, T_{sens} is the temperature sensor sensitivity and *G* is the gain of the op-amp. Figure 5.21 displays the entire test setup including the wireless impedance analyzer, heater and sensor op-amps, aluminum plate and electrodes attached to the heaters and sensors on the plate.

The sequential single source, backprojection approach is used because the best thermal CT results in *Chapter 4* are obtained using this method. An automated output sequences and data collection is embedded in the MCU software. A single heater at a time is activated with 5.6 W power for 600 seconds (10 minutes) then allowed to cool for the same amount of time before the next heater is activated. Preliminary tests verify that this

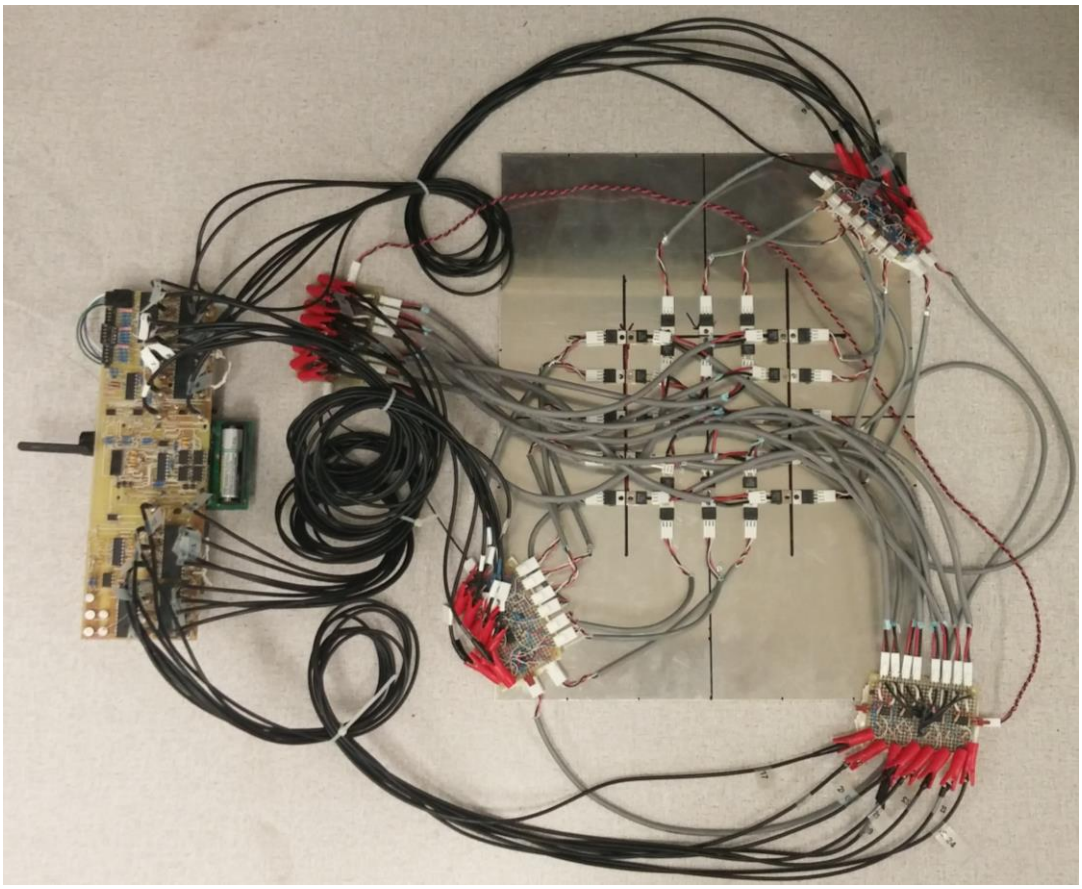

Figure 5.21 Complete experimental setup; including the wireless impedance analyzer, the heater and sensor op-amps, the instrumented aluminum plate and the electrodes attached to the heaters and sensors on the plate.

is sufficient cooling time for the plate to return to room temperature. During heater activation, the temperature response at each of the 16 sensors is recorded at 1 Hz (as heat transfer has a small time constant). Therefore, as the DAC output steps through each of the 16 heater channels, a voltage (corresponding to temperature) time-series for each of the 16 channels is recorded; resulting in 256 sets of data. This is first set of data is collected before any damage is induced. After the first set of data is recorded the ¾ inch (1.9 cm) diameter damage described above is introduced and a second set of data, following the same protocol as the first, is collected.

Select temperature time-series from the undamaged state of the plate are shown in Figure 5.22. Note, the decrease in the temperature response as the heater-sensor distance increases. The sequential single source, backprojection thermal CT algorithm described in *Chapter 4* is used to process the data and results in the reconstructed images shown in Figure 5.23. Figure 5.23a shows accurate damage detection using the backprojection (BP) method (with the actual damage superimposed on the image) that is improved when using

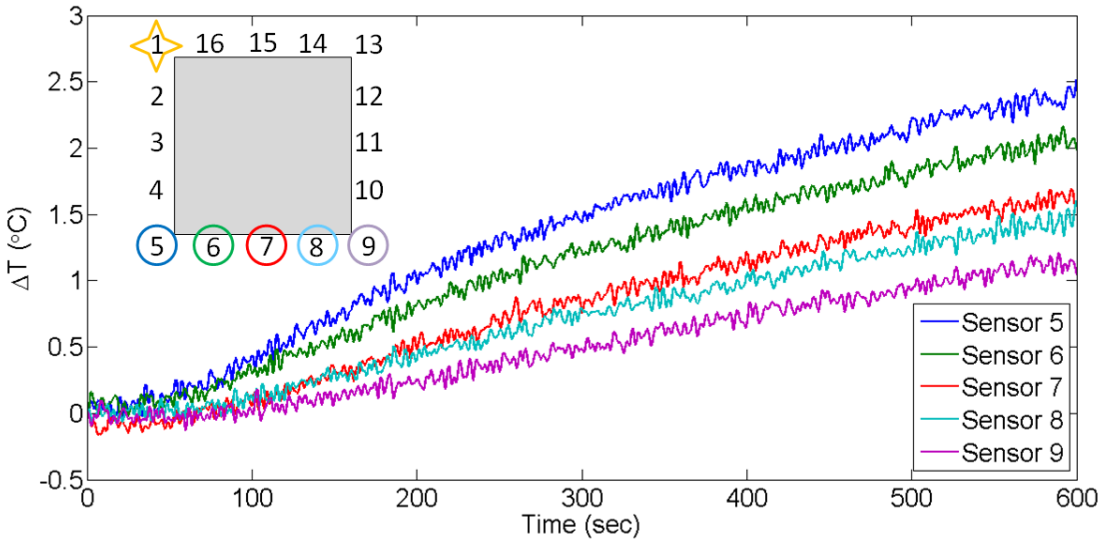

Figure 5.22 Time-series temperature response to heater 1 being activated on the plate in the undamaged state.

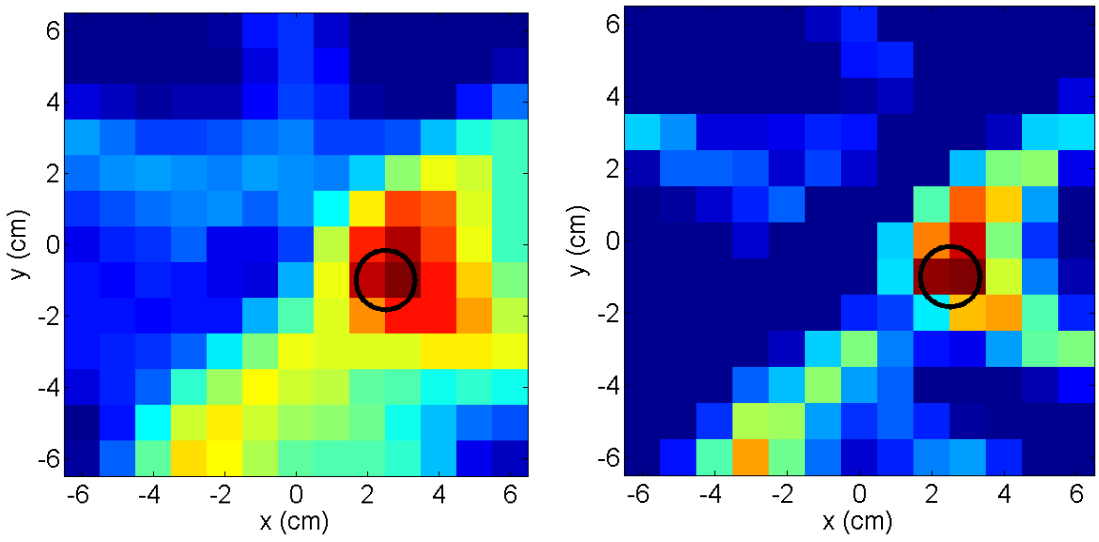

(a) (b)

Figure 5.23 Thermal CT reconstructed images with location of circular damage superimposed: (a) simple backprojection (BP); (b) filtered backprojection (FBP).

the filtered backprojection (FBP) approach shown in Figure 5.23b (pixels in figure are 0.39 inch x 0.39 inch (1 cm x 1 cm). The slight discrepancies between the actual damage and the reconstructed image can be attributed to the relatively large sensor spacing (1.18 inch (3 cm)) and small number of sensors (16) compared to the large area (22.3 in^2 (144 cm^2)) and small damage size (¾ inch (1.9 cm) diameter). The accurate experimental results fully validate the thermal CT method developed in *Chapter 4* as well as provide another validation case for the 32-channel wireless impedance analyzer.

5.6 Chapter Summary

Two models (4-channel and 32-channel) of a wireless impedance analyzer device capable of driving multiple spatial sensing techniques (*e.g.*, thermal CT, EIT, ultrasonics) are developed. This device is robust for permanent/long-term application and the wireless component allows potential application at a low-cost. The design successfully meets the

requirements to provide a largely versatile regulated output (AC up to 10 kHz, DC, current or voltage regulated, zero-mean or 1.65V mean, programmable waveform) and ADC sampling capabilities that can be routed through up to 32 input/output channels. The individual attributes are validated through device characterization. Furthermore, the 4-channel model designed specifically for EIS applications is validated to perform an experimental EIS interrogation accurately. The 32-channel model is used to perform both thermal CT and EIT spatial sensing experiments in an automated fashion. The accurate results not only validate the device's ability to enable wireless spatial sensing techniques, it also experimentally validates the thermal CT method developed in *Chapter 4*. Therefore, not only can this device be used to incorporate wireless thermal CT into an SHM system, it has the potential to enable multiple spatial sensing techniques on an SHM system.

Future iterations of the device can reduce its footprint by switching all through-hole and SOIC surface mount components to smaller form factor TSSOP surface mount components (using components with the same specifications, just a different size and mounting type). Furthermore, lower resistance 16 x 1 MUX chips are possible with TSSOP type devices, lowering this resistance will decrease parasitic resistance. Also, the DAC and ADC output/input frequencies can be improved with an improved MCU. Off-the-shelf MCU technology is constantly improving and the wireless analyzer is designed such that a new MCU can be used by simply routing a CLK and 8 GPIOs to the DAC and 15 GPIOs to the MUXs. The key controlling factor would be the hypothetical new MCU's ability (or speed) to look-up the new value in the waveform table and update the value of the GPIO pins while performing an ADC measurement. The MCU on the *Martlet* performs calculations at 90 MHz but because of *Martlet* overhead and the fact that the MCU requires

multiple cycles to service each interrupt (*i.e.*, ADC, look-up new waveform value, write GPIO to DAC, write GPIO to MUX to select channels) the effective DAC update frequency is 1 MHz. Therefore, if a new MCU can update the DAC output at greater than 1 MHz after accounting for overhead, ADC sampling, MUX switching and wireless communication, then it could be an effective upgrade. Another improvement that could be made is the expansion from 32 channels to 64 or more by adding MUXs if additional GPIO pins are available on a new MCU.

CHAPTER 6

CONCLUSION

6.1 Summary

The overarching goal of this dissertation is to fully marry the non-destructive evaluation (NDE), structural health monitoring (SHM) and data-to-decision (D2D) technologies for the purpose of providing a comprehensive D2D framework for asset management. While each technology has matured individually, an infrastructure management strategy can only be improved if the three are fused, thus enabling actionable insight and quantified data that informs decisions of critical importance. This is demonstrated in this thesis through the utilization of both global and local sensing approaches as well as the development of a D2D framework for two field deployments. Furthermore, the monitoring systems are wireless to reduce their installation time and cost so their proliferation is more feasible. The monitoring systems for these deployments are each geared with the focus of obtaining data that informs pre-determined action items, or decisions, that are of interest to the asset owner. The ability of SHM systems to visualize damage and increase their impact on decision-making can be augmented improved spatial sensing techniques capable of field application. Towards this end, a novel spatial sensing technique capable of field deployment and an accompanying state-of-the-art multi-channel wireless impedance analyzer capable of driving this new imaging technique as well as other imaging techniques currently being developed in the community is developed. The

contributions explained in the dissertation combine to both increase the benefit and decrease the cost of SHM systems for civil and naval infrastructure assets. Thus, empowering SHM systems to better assist with the maintenance and improvement of the world's infrastructure systems.

6.1.1 Rapid-to-deploy Wireless Monitoring System for Naval Vessels

The system is realized by means of a wireless hull monitoring strategy. The analytical objective is met with the development of a novel framework to determine sea conditions, or environmental operating conditions (EOCs), using inertial measurements (global sensing), relate sea conditions to acceleration/force responses (global sensing) on the vessel via response amplitude operators (RAOs), and relate vessel accelerations to a measurement of damage (local sensing) using consumed fatigue operators (CFOs). The empirical nature of these operators derived from sensor measurements eliminates uncertainties in estimates of ship behavior often introduced through the use of wave tank and computer models. The importance decreasing uncertainties of ship behavior is highlighted by the inclusion of the effects of slamming wave events on consumed fatigue. The short-term monitoring system herein is unique in both its ability to be quickly implemented (installed in a matter of hours) and its application to a smaller, *Boat* classification, vessel (the smaller vessel length compared to wave length contributing to different hydrodynamic responses than with larger vessels). It also provides an innovative data-driven framework for the assessment of EOCs, RAOs and CFOs for use in life-cycle analyses.

This improved, and now data-driven, D2D is achieved using empirical RAO and CFO functions, as derived herein. This novel framework allows for these functions to be

obtained with higher fidelity, in a quicker time frame and at a lower cost than the typical wave tank, CFD, or FEM modelling approaches. Ship owners could use the method validated in this dissertation to improve design and plan for forces and fatigue experienced by vessels in their fleets in a cost effective manner. For example, a short-term deployment of the system could be carried out over a sufficient set of sea conditions. This would allow vessel specific RAO and component specific CFO functions to be determined. Then, maritime and weather data could be used to probabilistically determine the number of hours a vessel would operate in given sea conditions. These forecasted operating conditions would then be used as input to the empirical RAOs and CFOs. Which, in turn, would predict stress loading and fatigue behavior to be used as a powerful decision-making tool to more accurately and efficiently execute life-cycle management strategies.

6.1.2 Permanent Wireless Monitoring System for Railroad Bridge

The long-term wireless bridge monitoring system is designed targeting the ability to identify specific loading hazards and damage scenarios. It has been collecting data from February 2016 to the present date. Data are transmitted to an onsite basestation server that uses a cellular modem to transmit the data to the laboratory server for near real-time data processing and archival. The system is completely self-powered using solar panels at each wireless sensing node and a larger solar panel at the basestation, and a conservative power consumption strategy that utilizes a triggering scheme to collect data only during loading events.

A two-tier multi-hazard alert system is setup that at its first tier triggers data collection for train crossing, barge collision and seismic events (all three phenomena being observed via global sensing). After these data have been wirelessly transmitted, first to the

onsite server, then to the laboratory server, they are processed to determine if certain thresholds have been reached that require attention from a bridge owner or manager. If such thresholds are exceeded, the second tier of the alert system sends an email notification to the bridge manager who has access to review the data that triggered the event. In addition, data from a critical eyebar element on the bridge is also analyzed (local sensing) and the load distribution across each eyebar link is calculated in order to track the distribution and identify any uneven distribution at the earliest juncture in time and send a notification if changes occur. These data-driven notifications are state-of-the-art and significant in that they provide quantifiable, meaningful data that the bridge owner and manager can actually use to inform their decision-making process. Moreover, this is achieved through the use of a low-cost wireless monitoring system.

6.1.3 Thermal Computed Tomography

To extend the benefits offered by local sensing further, a novel damage detection technique is developed that derives a thermal computed tomography (CT) approach applied to a point-based thermal heating and measurement setup. This method is developed for two-dimensional (2D) mapping of structural conditions. Innovative approaches are implemented to properly represent heat transfer and carry out the interrogation process with a limited number (32) of immobile heater-sensor point locations permanently installed around the perimeter of the specimen. The major advantage to the new technique is that it is capable of SHM application because of its low-cost and robust setup that enables permanent installation.

Two methods for steering a heat front across a specimen using the stationary heater-sensor setup are derived; phased array steering and sequential single source. Both of these

methods are used to assemble respective sinograms based on simulated results (including simulated discrete temperature readings around the perimeter) of two aluminum plate specimens; one being an unknown (damaged) specimen and the other being a known (undamaged) specimen. These sinograms are used to reconstruct images using Fourier interpolation (FI), backprojection and filtered backprojection (FBP), none of which require model updating/iterative solutions. All three reconstruction procedures show accurate results; however, the FBP shows the best results, which provide very good resolution considering the area being monitored 18.9 inches by 18.9 inches (48 cm by 48 cm) and the fact that only 32 heater-sensor locations are used. Among the two steering methods, the sequential single source method yields better results because it provides more rotation angles than does the phased array method (64 rotation angles versus 16). These results validate the technique as an effective method to continuously (or on-demand) visualize the state of a 2D area of a structure.

6.1.4 Multi-functional 32-channel Wireless Impedance Analyzer

This state-of-the-art device is developed to enable the thermal spatial imaging technique to be wireless and thus feasible for SHM applications. Furthermore, its multi-functional capability can be used to enable other spatial imaging techniques (*e.g.*, ultrasonic guided waves, EIT) for integration to SHM techniques. The following distinguishing characteristics of the device are attained: fully wireless (communication and power), 32 addressable channels (each capable of injection/output source, sink and sensing), option of either current or voltage controlled DC or AC output, programmable output waveform at zero-mean or nonzero-mean, high DAC and ADC sampling rates (>10 kHz), and adjustable output impedance to match that of the specimen being interrogated. These specifications

along with its small form factor give this device the potential to easily be integrated into current or future SHM systems.

One of the capabilities that is highlighted is the accurate electrical impedance spectroscopy (EIS) four-probe interrogation of an RC circuit. This measurement is more than just a DC resistance, but a complex (*i.e.*, real and imaginary) impedance measurement obtained by sweeping through excitation frequencies with a precisely regulated current output while the corresponding voltage response is recorded. This allows for smart materials embedded with sensing skins or fibers to be properly interrogated, which currently, typically must be done with large cumbersome equipment. Similarly, the capability of the device to complete electrical impedance tomography (EIT) spatial imaging is demonstrated. This requires an output to be cycled sequentially to multiple (32 in this case) electrodes. While a given electrode is being excited, the voltage response at the remaining nodes is recorded. These voltage measurements are successfully used to reconstruct the 2D image of electrical conductivity of nano-engineered concrete specimen and visualize damage. Furthermore, this device highlights the automated, wireless completion of the experimental validation of the thermal CT approach (developed in *Chapter 4*) which shows accurate results in reconstructing a spatial image and detecting the induced damage. The accurate results obtained from this experiment fulfill the objective of creating a new, wireless, permanently installable spatial imaging technique. This new technique and device can add to the local sensing capabilities of an SHM system by providing a more thorough (*i.e.*, spatial) view of the state of areas of interest on the structure.

6.2 Future Work

6.2.1 Specific Areas for Continuation of Research

For the wireless hull monitoring method to be fully implemented a dataset containing a larger envelope of sea conditions would need to be collect. Nonetheless, the study in this dissertation serves as a proof-of-concept that such an endeavor would yield impactful results. It would be beneficial to improve the accuracy of wave height and heading calculations by including a wave radar detector, or as a second option, a gyroscope at the center-of-gravity. Furthermore, future deployments could include additional strain gages or other fatigue monitoring techniques to gain component specific fatigue information at more locations and to better localize fatigue behavior. All of these proposed augmentations to the monitoring system could be easily integrated into the current architecture (both sensor hardware and analytical framework) used in the work discussed in *Chapter 2*. Nevertheless, even without these additional sensors the validated monitoring system and D2D can be extended to other vessels and EOCs to improve design and life-cycle approaches by providing a data-driven decision support system. The wireless bridge monitoring system also proves to provide valuable D2D capabilities. Because it is a long-term installation it will continue to operate. The current alerts will remain functional and can be further refined based on the bridge manager's request. Furthermore, the current monitoring system could be expanded to include more components of the Harahan Bridge or to include additional bridges within the rail network.

The wireless thermal CT approach is proven both through simulation and experimentation. Nevertheless, its value can be further increased by: characterizing the effects of damage severity, location and orientation with greater detail; exploring different

heater-sensor perimeter geometries (a circular perimeter could provide straightforward determination of projection angles); calibrating a sensing approach that begins heating one heater before the preceding heater has cooled down (in order to complete specimen interrogation more quickly) and, developing strategies to further increase temperature sensitivity and thus require less heat (power) output. Although, the wireless impedance analyzer achieves digital-to-analog conversion (DAC) and analog-to-digital conversion (ADC) frequencies of 10 kHz, this can be further improved, by using a faster microprocessor (as off-the-shelf microprocessors are developed with continually improving clocking frequency), thus enabling interrogation of even larger impedance values. Furthermore, the device can be extended to more than 32 channels if a microprocessor is used that has more general purpose input output (GPIO) pins available.

6.2.2 Broader Impact

The two successful field deployments of comprehensive wireless monitoring systems and D2D frameworks for asset management show strong proof that it would be worthwhile to employ similar approaches to other infrastructure assets. That is, for a given structure, identify critical decisions to be targeted in the design of a sensing and analysis strategy. These decisions, or action items, must: first, stand to offer added value to the asset owner when navigated optimally; and second, sensor measurements must indeed be capable of informing targeted decisions. The sensing strategy can be most effective when it considers global and local (with both point-based and spatial) sensing techniques.

Not only can the wireless thermal CT method be refined towards field application; but the wireless impedance analyzer should be utilized to convert other spatial and intricate NDE techniques to be capable of wireless field application. This device alone does not

automatically make any technique wireless but it highlights the ability for more involved sensing approaches to become wireless and field applicable. With these traits, already powerful interrogation techniques can become even more valuable. That is NDE techniques can be installed in the field and this can be achieved at a lower cost. Simultaneously decreasing cost and increasing benefit (or level to which data can inform decision-making). Thus, furnishing society with an enhanced means of maintaining and improving critical infrastructure.

REFERENCES

Abdel-Ghaffar, A., and Scalan, R. (1985). “Ambient vibration studies of Golden Gate.” *Journal of Engineering Mechanics*, 111(4), 463–482.

Akgül, F., and Frangopol, D. M. (2004). “Bridge rating and reliability correlation: comprehensive study for different bridge types.” *Journal of Structural Engineering*, 130, 1063–1074.

Aktan, A. E., Catbas, F. N., Grimmelsman, K.A., and Tsikos, C. J. (2000). “Issues in infrastructure health monitoring for management.” *Journal of Engineering Mechanics*, 126(7), 711–724.

Alampalli, S., and Ettouney, M. (2010). “Automated decision-making tool for bridge managers.” *Structural Materials Technology*.

Alifanov, O. M. (1994). *Inverse heat transfer problems*. International series in heat and mass transfer, Springer-Verlag.

Alter, D. M. (2008). *Using PWM output as a digital-to-analog converter on TMS320F280x digital signal ontroller.* Texas Instruments - Application Report.

American Association of State Highway and Transportation Officials [AASHTO]. (2012). *LRFD bridge design specifications*. Washington D.C.

American Bureau of Shipping [ABS], A. B. of S. (2003). *Technical Analyses Related to the PRESTIGE Casualty on 13 November 2002*.

American Railway Engineering and Maintenance-of-way Association [AREMA]. (2016). *Manual for Railway Engineering.*

American Society of Civil Engineers [ASCE]. (2013). *Report Card for America’s Infrastructure*.

Anastasopoulos, A., Kourousis, D., Botten, S., and Wang, G. (2009). “Acoustic emission monitoring for detecting structural defects in vessels and offshore structures.” *Ships and Offshore Structures*, 4(4), 363–372.

Andersen, E. Y., and Pedersen, L. (1994). “Structural health monitoring of the great belt east bridge.” *Strait Crossings*, 94, 189–195.

ArcGIS. (2016). “Ocean Basemap.” <https://www.arcgis.com/home/item.html?id=5ae9e138a17842688b0b79283a4353f6> (Aug. 15, 2016).

Aston, R. (2008). *Medical imaging equipment theory*. ABC Engineering Research, Pennsylvania.

Barrish, Jr., R. A. (2000). “Instrumented monitoring of the Commodore Barry Bridge.” *Proceedings of SPIE*, 3995, 112–126.

Beck, J. L., and Katafygiotis, L. S. (1998). “Updating Models and Their Uncertainties. I: Bayesian Statistical Framework.” *Journal of Engineering Mechanics*, 124(4), 455–461.

Bennett, R., Hayes-Gill, B., Crowe, J. A., Armitage, R., Rodgers, D., and Hendroff, A. (1999). “Wireless monitoring of highways.” *Smart Systems for Bridges, Structures, and Highways*, Newport Beach, CA, 173–182.

Bera, T. K., and Nagaraju, J. (2012). “Surface electrode switching of a 16-electrode wireless EIT system using RF-based digital data transmission scheme with 8 channel encoder/decoder ICs.” *Measurement: Journal of the International Measurement Confederation*, Elsevier Ltd, 45(3), 541–555.

Bertram, V. (2000). *Practical Ship Hydrodynamics*. *Practical Ship Hydrodynamics*,

Butterworth-Heinemann, Oxford.

Blevins, R. D. (2016). “Natural Frequency of Beams.” *Formulas for Dynamics, Acoustics and Vibration*, John Wiley & Sons Ltd., Somerset, 134–202.

Bourns. (2011). *PWR220T-20 Series Power Resistor*. Technical Datasheet.

Bouzid, O. M., Tian, G. Y., Cumanan, K., and Moore, D. (2014). “Structural Health Monitoring of Wind Turbine Blades : Acoustic Source Localization Using Wireless Sensor Networks.” *Journal of Sensors*, 2015, 11.

Brady, T. F., Bachman, R. J., Donnelly, M. J., and Griggs, D. B. (2004). *HSV-2 Swift Instrumentation and Technical Trials Plan*. Carderock, MD.

Brown, B. H. (2009). “Electrical impedance tomography (EIT): a review.” *Journal of Medical Engineering & Technology*, 27(3), 97–108.

Brownjohn, J. M. W. (2007). “Structural health monitoring of civil infrastructure.” *Philosophical Transactions. Series A, Mathematical, Physical, and Engineering Sciences*, 365(1851), 589–622.

Brownjohn, J. M. W., Bocciolone, M., Curami, A., Falco, M., and Zasso, A. (1994). “Humber bridge full-scale measurement campaigns 1990-1991.” *Journal of Wind Engineering and Industrial Aerodynamics*, 52(C), 185–218.

Burr-Brown (2003). *8-bit 165 MSPS digital-to-analog converter*. Texas Instruments - Datasheet.

Byers, W. G. (1999). “Railroad lifelines in earthquakes.” *1999 5th U.S. Conference on Lifeline Earthquake Engineering: Optimization Post-Earthquake Lifeline System Reliability*, ASCE, 776–785.

Canadian Infrastructure Report Card [CIRC]. (2016). *Canadian Infrastructure Report*

Card: Informing the Future.

Carder, D. S. (1937). "Observed vibrations of bridges ." *Bulletin of the Seismological Society of America*, 27(4), 267–303.

Catbas, F. N., Susoy, M., and Frangopol, D. M. (2008). "Structural health monitoring and reliability estimation: Long span truss bridge application with environmental monitoring data." *Engineering Structures*, 30(9), 2347–2359.

Chang, P. C., Flatau, A., and Liu, S. C. (2003). "Review Paper: Health Monitoring of Civil Infrastructure." *Structural Health Monitoring*, 2(3), 257–267.

Chen, G.-H., Leng, S., and Mistretta, C. a. (2005). "A novel extension of the parallel-beam projection-slice theorem to divergent fan-beam and cone-beam projections." *Medical physics*, 32, 654–665.

Cheung, M. S., Tadros, G. S., Brown, T., Dilger, W. H., Ghali, A., and Lau, D. T. (1997). "Field monitoring and research on performance of the Confederation Bridge." *Canadian Journal of Civil Engineering*, 24(6), 951–962.

Chintalapudi, K., Fu, T., Paek, J., Kothari, N., Rangwala, S., Caffrey, J., Govindan, R., Johnson, E., and Masri, S. (2006). "Monitoring civil structures with a wireless sensor network." *IEEE Internet Computing*, 10(2), 26–34.

Cho, H., and Lissenden, C. J. (2012). "Structural health monitoring of fatigue crack growth in plate structures with ultrasonic guided waves." *Structural Health Monitoring*, 11(4), 393–404.

Collette, M., and Incecik, A. (2006). "An approach for reliability-based fatigue design of welded joints on aluminunn high-speed vessels." *Journal of Ship Research*, 50(1), 85–98.

Seakeeping Committe (2007). *Final report and recommendations to the 25th ITTC*.

Cross, E. J., Koo, K. Y., Brownjohn, J. M. W., and Worden, K. (2013). "Long-term monitoring and data analysis of the Tamar Bridge." *Mechanical Systems and Signal Processing*, Elsevier, 35(1–2), 16–34.

CSiBridge. (2013). <https://wiki.csiamerica.com/display/CSiBridge/Home> (Jan. 1, 2016).

Cusano, G., Monti, S., and Velasco, A. (2003). "Full scale and model test investigation o f slamming effects on fast monohull vessels." *Hydroelasticity in Marine Technology*, 163–174.

Dassault Systèmes [DS]. (2014). "Abaqus 6.14." <http://abaqus.software.polimi.it/v6.14/index.html> (Jul. 21, 2016).

Davis, M. R., Watson, N. L., and Holloway, D. S. (2005). "Measurement of response amplitude operators for an 86 m high-speed catamaran." *Journal of Ship Research*, 49(2), 121–143.

Debord, F. (2013). "Meeting Notes: RB-M Prototype Hull Monitoring."

Dickey, R. L., Delong, R. C., and Gregov, Z. (1976). "A Hull Monitoring Sytem for Safe and Economic Operations." *2nd Ship Operation Automation Symposium*, 465 471.

Dong, J., Lowenhar, E., Godinez, V., and Carlos, M. (2015). "State-of-the-art wireless acoustic emission system for structural health monitoring." *Advances in Acoustic Emission Technology: Proceedings of the World Conference on Acoustic Emission--2013*, G. Shen, Z. Wu, and J. Zhang, eds., Springer New York, New York, NY, 15–22.

Drinkwater, B. W., and Wilcox, P. D. (2006). "Ultrasonic arrays for non-destructive

evaluation: a review." *NDT and E International*, 39(7), 525–541.

Ettouney, M. M., and Alampalli, S. (2016). "Introduction." *Infrastructure Health in Civil Engineering: Theory and Components*, 1–40.

Farrar, C. R., and Lieven, A. J. (2007). "Damage prognosis: the future of structural health monitoring." *Philosophical Transactions of the Royal Society A*, 365(1851), 623–632.

Farrar, C. R., and Worden, K. (2007). "An introduction to structural health monitoring." *Philosophical Transactions. Series A, Mathematical, Physical, and Engineering Sciences*, 365(1851), 303–315.

Fei Yan, Royer, R. L., and Rose, J. L. (2010). "Ultrasonic guided wave imaging techniques in structural health monitoring." *Journal of Intelligent Material Systems and Structures*, 21(3), 377–384.

Friswell, M. I. (2007). "Damage identification using inverse methods." *Philosophical Transactions of the Royal Society of London A: Mathematical, Physical and Engineering Sciences*, 365(1851), 393–410.

Fu, T. C., Fullerton, A. M., and Minnick, L. M. (2007). "Charachterization of Sea Fighter, FSF-1, wave slam events." *9th International Conference on Numerical Ship Hydrodynamics*, Ann Arbor, MI.

Galbreath, J. H., Townsend, C. P., Mundell, S. W., Hamel, M. J., Esser, B., Huston, D., and Arms, S. W. (2003). "Civil structure strain monitoring with power-efficient, high-speed wireless sensor networks." *Proceedings of the 4th International Workshop on Structural Health Monitoring*, Stanford, CA, 1215–1222.

Gangone, M. V, Whelan, M. J., and Janoyan, K. D. (2011). "Wireless monitoring of a multispan bridge superstructure for diagnostic load testing and system identification."

Computer-Aided Civil and Infrastructure Engineering, 26(7), 560–579.

Garrison, T. S., and Ellis, R. (2014). "Waves." *Oceanography: an Invitation to Marine Science*, Cenage Learning/Nelson Education, 282–313.

Ghosn, M. (2010). "Reliability based structural system performance indicators for highway bridges." *in proceedings of Structures Congress 2010*, 2781–2792.

Giurgiutiu, V. (2007). *Structural health monitoring: with piezoelectric wafer active sensors*. Academic Press.

Glaser, S. D. (2004). "Some real-world applications of wireless sensor nodes." *Proceedings of SPIE - The International Society for Optical Engineering*, 5391, 344–355.

Goh, C. L., Ayob, Nor Muzakir, N., Rahim, R. A., Rahim, H. A., Pusppanathan, M. J., Rahiman, M. H. F. R., Ling, L. P., and Zakaria, Z. (2013). "Study on wireless sensor based industrial tomography systems." *Sensors and Transducers*, 154(7), 71–81.

Gorry, G. A., and Scott Morton, M. S. (1971). "A framework for management information systems." Cambridge, MIT.

Gostautas, R. S., and Tamutus, T. A. (2015). "SHM of the eyebars of the old San Francisco Oakland Bay Bridge." *Structural Health Monitoring 2015*.

Gupta, S., Gonzalez, J. G., and Loh, K. H. (2016) "Self-sensing concrete enabled by nano-engineered cement aggregate interfaces." *Structural Health Monitoring* (1475-9217), 1 - 15.

Hay, T. R., Royer, R. L., Gao, H., Zhao, X., and Rose, J. L. (2006). "A comparison of embedded sensor Lamb wave ultrasonic tomography approaches for material loss detection." *Smart Materials and Structures*, 15, 946–951.

Hess, P. E. (2007). “Structural health monitoring for high-speed naval ships.” *6th International Workshop on Structural Health Monitoring*, Stanford, CA, 3–15.

Hibbeler, R. C. (2011). “Buckling of Columns.” *Mechanics of Materials*, Prentice Hall, Boston, 657–783.

Hitec Products Inc. [HPI]. (2017). *HBWF-35-125-6-GP-TR Datasheet.*

Huang, S.-K., and Loh, K. J. (2015). “Development of a portable electrical impedance tomography data acquisition system for near-real-time spatial sensing.” *SPIE - Sensors and Smart Structures Technologies for Civil, Mechanical, and Aerospace Systems*.

Imam, B., Righiniotis, T. D., Chryssanthopoulos, M. K., and Bell, B. (2006). “Analytical fatigue assessment of riveted rail bridges.” *Institution of Civil Engineers- Bridge Engineering*, Thomas Telford Ltd, 105–116.

Iyer, S. R., Sinha, S. K., and Schokker, A. J. (2005). “Ultrasonic C-Scan imaging of post-tensioned concrete bridge structures for detection of corrosion and voids.” *Computer-Aided Civil and Infrastructure Engineering*, 20(2), 79–94.

Jacobi, G., Thomas, G., Davis, M. R., and Davidson, G. (2014). “An insight into the slamming behaviour of large high-speed catamarans through full-scale measurements.” *Marine Science Technology*, 19, 15–32.

Janesch, J. (2013). “Two-wire vs. four-wire resistance measurements: which configuration makes sense for your application?” Keithley Instruments, Inc.

Jang, S., Jo, H., Cho, S., Mechitov, K., Rice, J. A., Sim, S., Jung, H., Yun, C., Spencer, B. F., and Agha, G. (2010). “Structural health monitoring of a cable-stayed bridge using smart sensor technology : deployment and evaluation.” *Smart Structures and Systems*,

6(5), 439–459.

Jeary, A. P., Chiu, G. C., and Wong, J. C. K. (2001). “Wholistic structural appraisal.” *8th International Conference and Structural Safety and Reliability: ICOSSAR*, Vol. 200.

Kane, M. B., Zhu, D., Hirose, M., Dong, X., Winter, B., Häckell, M., Lynch, J. P., Wang, Y., and Swartz, R. A. (2014). “Development of an Extensible Dual-Core Wireless Sensing Node for Cyber-Physical Systems.” *Proc. SPIE, Nondestructive Characterization for Composite Materials, Aerospace Engineering, Civil Infrastructure, and Homeland Security 2014*, SPIE - The International Society for Optical Engineering, San Diego, 19.

Kihl, D. P., Adler, N. E., and Devine, E. A. (2014). *Fatigue Test Results of Aluminum Components and Specimens Subjected to Constant and Random Amplitude Loadings*. West Bethesda, MD.

Kim, J., and Lynch, J. P. (2012). “Experimental analysis of vehiclebridge interaction using a wireless monitoring system and a two-stage system identification technique.” *Mechanical Systems and Signal Processing*, Elsevier, 28, 3–19.

Kim, J., Lynch, J. P., Lee, J.-J., and Lee, C.-G. (2011). “Truck-based mobile wireless sensor networks for the experimental observation of vehicle–bridge interaction.” *Smart Materials and Structures*, 20, 65009.

Kim, S., Pakzad, S., Culler, D., Demmel, J., Fenves, G., Glaser, S., and Turon, M. (2007). “Health monitoring of civil infrastructures using wireless sensor networks.” *Proceedings of the 6th international conference on Information processing in sensor networks*, ACM, Cambridge, Massachusetts, USA.

Ko, J. M., and Ni, Y. Q. (2005). “Technology Developments in Structural Health

Monitoring of Large-scale Bridges." *Engineering Structures*, 27(12), 1715–1725.

Kollár, L. (2003). *Structural stability in engineering practice*. CRC Press.

Kowalyshyn, D., and Metcalf, B. (2006). "A USCG systematic series of high speed planing hulls." *Trans SNAME*, (114), 268–309.

Kronenberg, P., Casanova, N., Inaudi, D., and Vurpillot, S. (1997). "Dam monitoring with fiber optics deformation sensors." *Smart Structures and Materials '97*, 3043, 2–11.

Kumarasena, T., Scanlan, R. H., and Morris, G. R. (1989). "Deer Isle Bridge: Field and computed vibration." *Journal of Structural Engineering*, 115(9), 2313–2328.

Kurata, M., Kim, J., Lynch, J. P., Linden, G. W. Van Der, Sedarat, H., Thometz, E., Hipley, P., and Sheng, L. H. (2012). "Internet-enabled wireless structural monitoring systems: development and permanent deployment at the New Carquinez suspension bridge." *Journal of Structural Engineering*, 139(10), 1668–1702.

Kwon, K., and Frangopol, D. M. (2012). "Fatigue life assessment and lifetime management of aluminum ships using life-cycle optimization." *Journal of Ship Research*, 56(2), 91–105.

Garza, J. M., Drew, D. R., and Chasey, A. D. (1998). "Simulating Highway Infrastructure Management Policies." *Journal of Management Engineering*, 14(October), 64–72.

Laflamme, S., Kollosche, M., and Connor, J. J. (2012). "Robust flexible capacitive surface sensor for structural health monitoring applications." *Journal of Engineering*, 139(7), 879–885.

Leander, J., Andersson, A., and Karoumi, R. (2010). "Monitoring and enhanced fatigue evaluation of a steel railway bridge." *Engineering Structures*, Elsevier Ltd, 32(3), 854–863.

Li, Q. S., Xiao, Y. Q., Fu, J. Y., and Li, Z. N. (2007). "Full-scale measurements of wind effects on the Jin Mao building." *Journal of Wind Engineering and Industrial Aerodynamics*, 95(6), 445–466.

Lichtenstein, A. G. (1993). "The Silver Bridge collapse recounted." *Journal of Performance of Constructed Facilities*, 7(4), 249–261.

Lin, X., and Yuan, F. G. (2001). "Damage Detection of a Plate Using Migration Technique." *Journal of Intelligent Materials Systems and Structures*, 12(7), 469–482.

Lind, S. J., Stansby, P. K., Rogers, B. D., and Lloyd, P. M. (2015). "Numerical predictions of water – air wave slam using incompressible – compressible smoothed particle hydrodynamics." *Applied Ocean Research*, Elsevier B.V., 49, 57–71.

Lladós, J. B., and Petit, B. (2013). "Possibilities and limits of environmental criminal protection." *Revista Para el Análsis del Derecho*.

Loh, K. J., Hou, T.-C., Lynch, J. P., and Kotov, N. A. (2009). "Carbon nanotube sensing skins for spatial strain and impact damage identification." *Journal of Nondestructive Evaluation*, 28(1), 9–25.

Lynch, J. P. (2005). "Design of a wireless active sensing unit for localized structural health monitoring." *Structural Control and Health Monitoring*, 12(3–4), 405–423.

Lynch, J. P., Farrar, C. R., and Michaels, J. E. (2016). "Structural health monitoring: Technological advances to practical implementations." *Proceedings of the IEEE*, 104(8), 1508–1512.

Lynch, J. P., and Loh, K. J. (2006). "A summary review of wireless sensors and sensor networks for structural health monitoring." *The Shock and Vibration Digest*, 38(2), 91–128.

Lynch, J. P., Sundararajan, A., Law, K. H., Kiremidjian, A. S., Carryer, E., Sohn, H., and Farrar, C. R. (2003). "Field Validation of a wireless structural monitoring system on the Alamosa Canyon Bridge." *Proceedings of SPIE*, 5057, 267–278.

Lynch, J. P., Wang, Y., Loh, K., Yi, J. H., and Yun, C.-B. B. (2006). "Performance monitoring of the Geumdang Bridge using a dense network of high-resolution wireless sensors." *Smart Materials and Structures*, 15(6), 1561–1575.

Machnitzki, T. R. (2010). "Harahan Bridge (Memphis, Tennessee) view from Martyrs Park."

Mailoux, R. J. (2005). *Phased array antenna handbook*. Artech House, Boston.

Maldague, X. (2002). "Introduction to NDT by active infrared thermography." *Materials Evaluation*, 60, 1060–1073.

Mangal, L., Idichandy, V. G., and Ganapathy, C. (2001). "Structural monitoring of offshore platforms using impulse and relaxation response." *Ocean Engineering*, 28(6), 689–705.

Maser, K., Egri, R., Lichtenstein, A., and Chase, S. (1996). "Field evaluation of a wireless global bridge evaluation and monitoring system (WGBEMS)." *Engineering Mechanics, ASCE*, 955–958.

McCulloch, D. S., and Bonilla, M. G. (1970). *Effects of the earthquake of March 27, 1964, on The Alaska Railroad*.

Mclamore, V. R., Hart, G. C., and Stubbs, I. R. (1971). "Ambient vibration of two suspension bridges." *Journal of the Structural Division*, 97, 2567–2581.

McManamon, P. F., Bos, P. J., Escuti, M. J., Heikenfeld, J., Serati, S., and Watson, E. A. (2009). "A review of phased array steering for narrow-band electrooptical systems."

Proceedings of the IEEE, 1078–1096.

Micro Measurements. (2016). “General Purpose Strain Gages - Rectangular Rosette.” *Technical Datasheet*

Meyer, J., Bischoff, R., Feltrin, G., and Motavalli, M. (2010). “Wireless sensor networks for long-term structural health monitoring.” *Smart Structures and Systems*, 6(3), 263 – 275.

Miner, M. A. (1945). “Cumulative fatigue damage.” *ASME Journal of Applied Mechanics*, 12(3), A159–A164.

Moore, M., Phares, B., Graybeal, B., Rolander, D., and Washer, G. (2001). *Reliability of Visual Inspection for Highway Bridges*. *Journal of Engineering Mechanics*, Federal Highway Administration, FHWA-RD-01-020.

Moteff, J., and Parfomak, P. (2004). “Critical infrastructure and key assets definition and identification." *Congressional Research Service - The Library of Congress*, Order Code RL32631.

Mottershead, J. E., and Friswell, M. I. (1993). “Model updating in structural dynamics: a survey.” *Journal of Sound and Vibration*, 167(2), 347–375.

Moyo, P., Brownjohn, J. M. W., Suresh, R., and Tjin, S. C. (2005). “Development of fiber Bragg grating sensors for monitoring civil infrastructure.” *Engineering Structures*, 27(12 SPEC. ISS.), 1828–1834.

Murayama, H., Kageyama, K., Uzawa, K., Ohara, K., and Igawa, H. (2012). “Strain monitoring of a single-lap joint with embedded fiber-optic distributed sensors.” *Structural Health Monitoring*, 11(3), 325–344.

National Transportation Safety Board [NTSB] (1989). *Aircraft Accident Report Aloha*

Airlines, flight 243, Boring 737-200, N73711, Near Maui, Hawaii, April 28, 1988.

National Transportation Safety Board [NTSB]. (2010). *Pacific gas and electric company natural gas transmission pipeline rupture and fire San Bruno, California September 9, 2010.* 1–15.

Nielsen, U. D. (2017). "A concise account of techniques available for shipboard sea state estimation." *Ocean Engineering,* 129, 352-362.

Nutter Jr., R. S., and Aldridge, M. D. (1988). "Status of mine monitoring and communications." *IEEE Transactions on Industry Applications*, 24(5), 820–826.

O'Connor, S. M., Lynch, J. P., and Gilbert, A. C. (2014). "Compressed sensing embedded in an operational wireless sensor network to achieve energy efficiency in long-term monitoring applications." *Smart Materials and Structures*, IOP Publishing, 23(8).

Okundi, E., Aylott, P. J., and Hassanein, A. M. (2003). "Structural health monitoring of underground railways." *SHMII-1, Structural Health Monitoring and Intelligent infrastructures*, 1039–1046.

ON Semiconductor [OS]. (2011). "Low noise dual/quad operational amplifiers." *Technical Datasheet,* Rev 9.

ON Semiconductor [OS]. (2013). "1.0 A output current , dual power operational amplifiers." *Technical Datasheet,* Rev 11.

Otter, D. ., Joy, R. ., Jones, M. ., and Maal, L. . (2012). "Need for bridge monitoring systems to counter railroad bridge service interruptions." *Transportation Research Record: Journal of the Transportation Research Board*, (2313), 134–143.

Ou, J. P., Li, H. W., Xiao, Y. Q., and Li, Q. S. (2005). "Health dynamic measurement of tall building using wireless sensor network." *Smart Structures and Materials 2005:*

Sensors and Smart Structures Technologies for Civil, Mechanical, and Aerospace, Pts 1 and 2, 5765(1–2), 205–216.

Park, H. S., Shin, Y., Choi, S. W., and Kim, Y. (2013). "An integrative structural health monitoring system for the local/global responses of a large-scale irregular building under construction." *Sensors*, 13(7), 9085–9103.

Pedley, M. (2013). "Tilt Sensing Using a Three-Axis Accelerometer." *Freescale semiconductor application notes*, 1–22.

Piro, D. J. (2013). "A Hydroelastic method for the analysis of global response due to slamming events." PhD Dissertation - University of Michigan, Ann Arbor, MI.

Power, D. J. (2008). "Understanding Data-Driven Decision Support Systems." *Information Systems Management*, 25(2), 149–154.

Pyo, S., Loh, K. J., Hou, T., Jarva, E., and Lynch, J. P. (2011). "A wireless impedance analyzer for automated tomographic mapping of a nanoengineered sensing skin." *Smart Structures and Systems*, 8(1), 139–155.

Union Pacific Railroad [UPR] (2013). *Bridge Assessment Inspection Reference Cards*.

Rainer, J. H., and Van Selst, A. (1976). "Dynamic properties of Lions' Gate suspension bridge." *ASCE/EMD Speciality Conference on Dynamic Response of Structures: Instrumentation, Testing Methods, System Identification*, Los Angeles, CA, 243–252.

Reid, R. L. (2010). "Damaged Eyebar Section Replaced On San Francisco--Oakland Bay Bridge." *Civil Engineering—ASCE*, 80(4).

Roemer, J., Pieczonka, L., Szwedo, M., Uhl, T., and Staszewski, W. J. (2013). "Thermography of metallic and composite structures-review of applications." *International Workshop on Smart Materials, Structures & SHM*.

Rose, J. L. (2004). *Ultrasonic waves in solid media*. Cambridge University Press.

Rytter, A. (1993). "Vibration based inspection of civil engineering structures." *Building Technology and Structural Engineering,* Aalborg University, Denmark.

Salinas. (2012). "Statement of Work - 45RBM Full Scale Load Measurement."

Schlichting, J., Ziegler, M., Maierhofer, C., and Kreutzbruck, M. (2012). "Flying laser spot thermography for the fast detection of surface breaking cracks." *18th World Conference on Nondestructive Testing*.

Schwab, K. (2013). *The Global Competitiveness Report*.

Seakeeping Committe (2007). *Final report and recommendations to the 25th ITTC*.

Shepard, D. M., and Curtis, J. M. (2010). "U.S. Coast Guard Response Boat – Medium (RB-M)." *The First Chesapeake Power Boat Symposium*, Annapolis, MD.

Ship Motion Associates [SMA]. (1999). *POWERSEA Planing Hull Simulator*. Portland, ME.

Silicon Design Inc. [SDI]. (2016). "Specialty Low Voltage +5V Models Accelerometer Modules." *Technical Datasheet.*

Sjödahl, P., Dahlin, T., Johansson, S., and Loke, M. H. (2008). "Resistivity monitoring for leakage and internal erosion detection at Holby embankment dam." *Journal of Applied Geophysics*, 65(3–4), 155–164.

Smothers, R. (1993). "Dozens are killed in wreck of train in Alabama bayou." *The New York Times,* A1.

Sohn, H., Farrar, C. R., Hemez, F. M., Shunk, D. D., Stinemates, D. W., Nadler, B. R., and Czarnecki, J. J. (2003). "A review of structural health monitoring literature 1996-2001." *Technical Report Annex to SAMCO Summer Acadamy*, Los Alamos National

Laboratory, Los Alamos, NM.

Spencer, B. F., Jo, H., Mechitov, K. A., Li, J., Sim, S. H., Kim, R. E., Cho, S., Linderman, L. E., Moinzadeh, P., Giles, R. K., and Agha, G. (2016). "Recent advances in wireless smart sensors for multi-scale monitoring and control of civil infrastructure." *Journal of Civil Structural Health Monitoring*, Springer Berlin Heidelberg, 6(1), 17–41.

Spidsoe, N., Berg, S., Hoen, C., and Beck, G. (1980). "Measured behaviour of platforms on the Norwegian Continental Shelf." *European Offshore Petroleum Conference*.

Staszewski, W. J., Boller, C., and Tomlinson, G. (2004). *Health Monitoring of Aerospace Structures: Smart Sensor Technologies and Signal Processing*. John Wiley & Sons Ltd., West Sussex, England.

Straser, E. G., and Kiremidjian, A. S. (1998). "A modular, wireless damage monitoring system for structures." John A. Blume Earthquake Engineering Center Stanford.

Sumitoro, S., Matsui, Y., Kono, M., Okamoto, T., and Fujii, K. (2001). "Long span bridge health monitoring system in Japan." *6th Annual International Symposium on NDE for Health Monitoring and Diagnostics*, 4337, 517–524.

Swartz, R. A., Jung, D., Lynch, J. P., Wang, Y., Shi, D., and Flynn, M. P. (2005). "Design of a wireless sensor for scalable distributed in-network computation in a structural health monitoring system." *5th International Workshop on Structural Health Monitoring*, Stanford, CA.

Swartz, R. A., Lynch, J. P., Zerbst, S., Sweetman, B., and Rolfes, R. (2010). "Structural monitoring of wind turbines using wireless sensor networks." *Smart Structures and Systems*, 6(3), 1–8.

Swartz, R. A., Zimmerman, A. T., Lynch, J. P., Rosario, J., Brady, T., Salvino, L., and

Law, K. H. (2012). “Hybrid wireless hull monitoring system for naval combat vessels.” *Structure and Infrastructure Engineering*, 8(7), 621–638.

Texas Instruments. [TI]. (2000). “LM35 Precision Centigrade Temperature Sensors.” *Technial Datasheet*, Dallas, TX.

Texas Instruments. (2007). *CC2520 Datasheet*, Dallas, TX.

Texas Instruments. (2008). *CC2591 Datasheet*, Dallas, TX.

Texas Instruments. (2011). *TMS320F2806x Datasheet*, Dallas, TX.

Texas Instruments [TI]. (2013). “2.4 GHz IEE 802.15.4/ZigBee-ready RF Transceiver.” *Technical Datasheet*, Dallas, TX.

Texas Instruments [TI]. (2014). “Code Composer Studio v5.” <http://processors.wiki.ti.com/index.php/Category:Code_Composer_Studio_v5> (Feb. 1, 2017).

The Mathworks Inc [TMI]. (2013). “MATLAB.” Natick, MA.

Thomas, G. A., Davis, M. R., Holloway, D. S., Watson, N. L., and Roberts, T. J. (2003). “Slamming response of a large high-speed wave-piercer catamaran.” *Marine Technology*, 40(2), 126–140.

Thomson, B. W. E. (1949). “Delay networks having maximally flat frequency characteristics.” *Proceedings of the IEE-Part III: Radio and Communication Engineering*, 487–490.

Thornhill, E. M., and Stredulinksky, D. C. (2010). “Real time local sea state measurements using wave radar and ship motions.” *SNAME Annual Meeting*, 118(M), 248–268.

United States Coast Guard [USCG]. (2016). “Acquisition Directorate.” <2146 Westwood Terrace, Grapevine, TX 76051> (Dec. 26, 2016).

Wang, Y., Lynch, J. P., and Law, K. H. (2007). “A wireless structural health monitoring system with multithreaded sensing devices: design and validation.” *Structure and Infrastructure Engineering*, 3(2), 103–120.

Warnsinck, W. H., and Denis, M. S. (1957). “Dutch destroyer trials.” *Proceedings of the Symposium on the Behavior of Ships in a Seaway*, 439–467.

Weng, J. H., Loh, C. H., Lynch, J. P., Lu, K. C., Lin, P. Y., and Wang, Y. (2008). “Output-only modal identification of a cable-stayed bridge using wireless monitoring systems.” *Engineering Structures*, 30(7), 1820–1830.

Whelan, M. J., Fuchs, M. P., Gangone, M. V., and Janoyan, K. D. (2007). “Development of a wireless bridge monitoring system for condition assessment using hybrid techniques.” *Proceedings of SPIE*, 6530, 65300H–65300H–12.

WinSystems. (2016). “PPM-C393-S.” *Technical Datasheet*

Wong, K.-Y. (2007). “Design of a structural health monitoring system for long-span bridges.” *Structure and Infrastructure Engineering*, 3(2), 169–185.

Worden, K., Farrar, C. R., Manson, G., and Park, G. (2007). “The fundamental axioms of structural health monitoring.” *Proceedings of the Royal Society A: Mathematical, Physical and Engineering Sciences*, 463(2082), 1639–1664.

Wu, Z., and Su, H. (2005). “Dam health diagnosis and evaluation.” *Smart Materials and Structures*, 14(3), S130–S136.

Xu, Z. (2013). “Medical imaging systems, course notes.” University of Michigan, Ann Arbor, MI.

Yao, Y., and Glisic, B. (2015). “Detection of steel fatigue cracks with strain sensing sheets based on large area electronics.” *Sensors*, 15(4), 8088–8108.

Young, I. R. (Ed.). (1999). “Wave theory.” *Wind Generated Ocean Waves*, Elsevier, 3–23.

Zhang, Y., Kurata, M., and Lynch, J. P. (2016). “Long-term modal analysis of wireless structural monitoring data from a suspension bridge under varying environmental and operational conditions : system design and automated modal analysis.” *Journal of Engineering Mechanics*.

Zhao, X., Qian, T., Mei, G., Kwan, C., Zane, R., Walsh, C., Paing, T., and Popovic, Z. (2007). “Active health monitoring of an aircraft wing with an embedded piezoelectric sensor/actuator network: II. Wireless approaches.” *Smart Materials and Structures*, 16(4), 1218–1225.

Zimmerman, A. T., Shiraishi, M., Swartz, R. A., and Lynch, J. P. (2008). “Automated modal parameter estimation by parallel processing within wireless monitoring systems.” *ASCE Journal of Infrastructure Systems*, 14(1), 102–113.

Zonta, D., Glisic, B., and Adriaenssens, S. (2014). “Value of information: impact of monitoring on decision-making.” *Structural Control and Health Monitoring*, 21(7), 1043–1056.